

Copyright
by
Yu-Hao Tsai
2017

**The Dissertation Committee for Yu-Hao Tsai Certifies that this is the approved
version of the following dissertation:**

**First Principle Study of Transition Metal Oxide (Catalytic) Electrodes
for Electrochemical Energy Technologies**

Committee:

Gyeong S. Hwang, Supervisor

Arumugam Manthiram

Guihua Yu

Paulo Ferreira

**First Principle Study of Transition Metal Oxide (Catalytic) Electrodes
for Electrochemical Energy Technologies**

by

Yu-Hao Tsai

Dissertation

Presented to the Faculty of the Graduate School of

The University of Texas at Austin

in Partial Fulfillment

of the Requirements

for the Degree of

Doctor of Philosophy

The University of Texas at Austin

August 2017

Dedication

To my parents, Lang-Fu Tsai and Yu-Chun Chang; brother, Yuhsin Tsai; fiancée, Ling-Hui Chen.

Acknowledgements

I firstly would like to thank my supervisor, Professor Gyeong S. Hwang, for his support and encouragement. His meticulous attitude toward research and energetic passion for science are inspiring and truly admirable. Warmly thanks to all my dissertation committee, Professor Arumugam Manthiram, Guihua Yu, and Paulo Ferreira, each of whom has set up a unique scholarly model and help me in various ways.

I would next like to thank all group members for marching with me and with whom I have shared all the memorable moments in the journey; Kyoung Eun Kweon, Eunsu Paek, John Adam Stephens, Yongjin Lee, Chia-Yun Chou, Alexander J. Pak, Dhivya Manogaran, Myungsuk Lee, Haley Maren Stowe, Gregory Hartmann, Mathew Boyer, Linas Vilciauskas, Oscar Nordness. I wish to especially thank Kyoung Eun Kweon and Chia-Yun Chou for being my valuable mentors, collaborators and close friends.

I would like to thank my parents, Lang-Fu Tsai and Yu-Chun Chang, for their longstanding support and precious guidance in all perspectives of both life and career. I would also like to thank my brother, Yuhsin Tsai, for always having faith in me. Finally and most importantly, I want to thank my fiancée, Ling-Hui Chen, for her love, accompany and selfless support.

First Principle Study of Transition Metal Oxide (Catalytic) Electrodes for Electrochemical Energy Technologies

Yu-Hao Tsai, Ph.D.

The University of Texas at Austin, 2017

Supervisor: Gyeong S. Hwang

To fulfill the needs for developing the alternative energy technologies, searching for the adequate electrode materials which catalyze the electrochemical reactions utilized in devices such as fuel cell, Li-ion batteries, and related applications such as hydrogen generation and storage, has been a longstanding challenge. Among various catalysts, transition metal oxides (TMO) draw great attentions due to their low-cost, high stability, and, most importantly, a great variety of structures and electrical properties. Nonetheless, studying electrochemical reactions catalyzed by TMO is a challenging task due to the possible multivalent systems, flexible coordinations of lattice atoms, adjustable surface structures and diverse surface species. In the past decades, many innovative approaches have been explored with encouraging results; however, the mechanisms of incorporating the bulk/surface TMO structures in various chemical reactions still remain unclear. In this dissertation, using quantum mechanical calculations, we attempt to improve the fundamental understandings of how structures and electronic properties of TMO materials facilitate the electrochemical reactions of interest.

To identify the possible causes for CuO and Cu structures having different selectivity in catalysis, in Chapter 3, we study the CO₂ reduction reaction (CO₂RR) catalyzed by CuO (111) surface structure, and compare the results with the more widely studied Cu (100) surface. The roles played by the electronic properties of two materials in their selectivity are elucidated. In Chapter 4 and 5, we study the oxygen evolution reaction (OER) for LiCoO₂ surface structure. The structures and stabilities of Li-, O-, and H-terminated surface are investigated comprehensively. Based on the results, the formation of H-terminated surface results from Li/H exchange at the solid/liquid interface is proposed (Chapter 4). Along with the findings, we explore the possible mechanisms for the OER for non-metal terminated LiCoO₂ surface (Chapter 5). In Chapter 6, we study the oxygen reduction reaction (ORR) for Co₃O₄ (111) H-terminated surface structure. The possible reaction steps for both four-electron and two-electron pathway are investigated. In Chapter 7, the PO₄-deficient LiFePO₄/FePO₄ structures are investigated to understand how the presence of polyanion defects in the matrices could potentially improve the performance of the materials as electrodes in Li-ion batteries.

Table of Contents

| | |
|---|------|
| List of Tables | xi |
| List of Figures | xiii |
| Chapter 1 : Introduction | 1 |
| Chapter 2 : Theoretical Background | 4 |
| 2.1 Schrödinger Equation for Many-Body System | 4 |
| 2.2 Hartree-Fock Theory | 5 |
| 2.3 Density Functional Theory | 7 |
| 2.4 Exchange-Correlation Function | 9 |
| 2.5 Pseudopotential | 10 |
| Chapter 3 : Reaction Mechanisms for the Electrochemical Reduction of CO ₂ on CuO (111) Surface | 13 |
| 3.1 Introduction | 13 |
| 3.2 Methodology | 15 |
| 3.3 Results and Discussion | 16 |
| 3.3.1 Bulk Properties of CuO Structure | 16 |
| 3.3.2 CuO (111) Surface Structure | 18 |
| 3.3.3 Adsorption of H ₂ O on CuO (111) Surface | 21 |
| 3.3.4 Adsorption of CO ₂ on CuO (111) Surface | 24 |
| 3.3.5 Selectivity Toward Formate Anion and CO Molecule | 29 |
| 3.3.6 Selectivity for CuO (111) and Cu (100) Surface | 31 |
| 3.4 Summary | 34 |
| Chapter 4 : Structure and Stability of LiCoO ₂ Surface | 36 |
| 4.1 Introduction | 36 |
| 4.2 Methodology | 38 |
| 4.3 Results and Discussion | 40 |
| 4.3.1 Bulk Properties of LiCoO ₂ | 40 |

| | |
|---|----|
| 4.3.2 Dependence of Surface Energy on Termination | 45 |
| 4.3.3 Li-terminated Surface Structure | 47 |
| 4.3.4 Surface Li-deficiency | 50 |
| 4.3.5 O-terminated Surface Structure | 52 |
| 4.3.6 H-terminated surface | 55 |
| 4.4 Summary | 58 |
| Chapter 5 : Reaction Mechanisms for the Oxygen Evolution Reaction on LiCoO_2 (001) Surface | |
| 5.1 Introduction | 62 |
| 5.2 Methodology | 63 |
| 5.3 Results and Discussion | 64 |
| 5.3.1 H-terminated Surface in Aqueous Solution | 64 |
| 5.3.2 Oxidized Surface Structure | 66 |
| 5.3.3 Reaction Pathway for OER | 68 |
| 5.3.4 Dependence of H and OH Binding Energy on H-removal Concentration | 69 |
| 5.3.5 Reaction Enthalpies | 75 |
| 5.4 Summary | 76 |
| Chapter 6 : Mechanisms for the Oxygen Reduction Reaction on Co_3O_4 (111) Surface | |
| 6.1 Introduction | 78 |
| 6.2 Methodology | 79 |
| 6.3 Results and Discussion | 81 |
| 6.3.1 Bulk Properties of Co_3O_4 structure | 81 |
| 6.3.2 Co_3O_4 (111) Surface Structure | 84 |
| 6.3.3 Reaction Pathway | 89 |
| 6.3.4 Mechanisms for ORR | 91 |
| 6.3.5 The Free Energy Diagram | 96 |
| 6.4 Summary | 99 |

| | |
|--|-----|
| Chapter 7 : Investigation of Metal-Oxide Cathode Materials for Lithium Ion Batteries: Phosphate Deficient LiFePO_4 and FePO_4 | 102 |
| 7.1 Introduction | 102 |
| 7.2 Methodology | 103 |
| 7.3 Results and Discussion | 104 |
| 7.3.1 Pristine Bulk Structure | 104 |
| 7.3.2 PO_4 -deficient FePO_4 Structure | 107 |
| 7.3.3 Relative Stability of Defected FePO_4 in Various Charged States | 110 |
| 7.3.4 PO_4 -deficient LiFePO_4 Structure | 111 |
| 7.3.5 Relative Stability of PO_4 -defected LiFePO_4 in Various Charged States | 114 |
| 7.3.6 Mechanical Properties | 118 |
| 7.4 Summary | 119 |
| References | 122 |

List of Tables

| | |
|--|----|
| Table 3.1 Adsorption energies of CO and HCO_2^- anions on CuO (111) and Cu (100) surface structure. Energies calculated using the hybrid functionals (HSE06) are in the square parenthesis. | 32 |
| Table 4.1 The bulk properties of layered LiCoO_2 (L-LCO) structure (lattice constants, bond distances, gap energies and total energy per formula unit) predicted using DFT+U and hybrid functionals, together with the experimental data (Exp.) for comparison. The portions of exact HF exchange potential are in parentheses. | 41 |
| Table 4.2 The bulk properties of spinel LiCoO_2 (S-LCO) structure (lattice constants, bond distances, gap energies, and total energy per formula unit) predicted using DFT+U and hybrid functionals, together with the experimental data (Exp.) for comparison. The portions of exact HF exchange potential are in parentheses. | 42 |
| Table 4.3 Bonding distances of atoms denoted in Fig. 4, 6 and 8 for Li-terminated, O-terminated and H-terminated surface structures, respectively. | 49 |
| Table 5.1 Predicted hydrogen binding and water dissociative adsorption energies on the H-terminated surface structure with various amounts of clustered H-removals. The energies for separated H-removal cases are in the square brackets. | 69 |
| Table 5.2 Predicted enthalpies of reactions for the proposed OER pathway. The calculations are based on the binding energy of $\ast\text{H}$ on surface with various amounts of clustered H-removals. | 75 |
| Table 6.1 Energy difference between a low- and high-spin Co^{3+} ion in Co_3O_4 bulk structure calculated using various U values. | 83 |
| Table 6.2 H-bonding energies on fully H-terminated surface structure; U(TET) and U(OCT) are U-values applied for the tetrahedral and octahedral Co atoms, respectively. The portion of Hartree-Fock exchange energy in HSE06 is marked in percentage. | 87 |
| Table 6.3 Removal and adsorption energies of $\ast\text{OH}$ and $\ast\text{O}_2$ on Co_3O_4 (111) H-terminated surface, respectively, and enthalpies of each reaction steps are calculated using various U values. | 90 |

Table 6.4 Difference of adsorption energies of partially ($\text{*O}_2^{\delta-}$) and fully (*O_2^-) charge transfer to the superoxyl anion on Co_3O_4 (111) H-terminated surface structure; the enthalpies of step 1 and 2 are calculated based on the fully charge transfer case. ... 93

Table 7.1 Valence states of the indicated Fe (left of slash) and distances (\AA) from the Fe to PO_4 vacancy center (right of slash) of in optimized structures of pristine and PO_4 -deficient FePO_4 under various charge states. 108

Table 7.2 Valence states of the indicated Fe (left of slash) and distances (\AA) from the Fe to PO_4 vacancy center (right of slash) of in optimized structures of pristine and PO_4 -deficient LiFePO_4 under various charge states. 112

List of Figures

| | |
|---|----|
| Figure 2.1 Self-consistent Kohn-Sham equation diagram. | 9 |
| Figure 2.2 Comparison between pseudo and all-electron wavefunctions and pseudo and all-electron potentials. | 11 |
| Figure 3.1 Atomic configuration of unit cell of CuO structure. Arrows denotes the spin alignments. | 17 |
| Figure 3.2 Electron density of states (DOS) projected onto Cu (blue) and O (red) atoms of CuO structure, predicted using: DFT+U (a) and HSE06 (b). The vertical line indicates the Fermi level position. | 18 |
| Figure 3.3 Structure of CuO (111) surface. Left: Side-view of the slab structure with denotations of 3-fold undercoordinated Cu (Cu_{3c}), 4-fold coordinated Cu (Cu_{4c}), 3-fold undercoordinated O (O_{3c}), and 4-fold coordinated O (O_{4c}) atoms. Right: Top-view of the surface. Distances (\AA) of Co – O and Co_{3c} – Co_{3c} are indicted. | 19 |
| Figure 3.4 Electron density of states (DOS) of CuO (111) surface structure, projected onto Cu_{3c} (grey), Cu_{4c} (blue), O_{3c} (red) and O_{4c} (green) atoms. The vertical line indicates the Fermi level position. | 20 |
| Figure 3.5 Structures of H_2O -adosorption on surfaces: 0.25 ML H_2O (a), 0.25 ML dissociative H_2O (b), and 0.5 ML non-dissociative/dissociative H_2O (c) adsorptions; insets are the 0.5 ML cases for related adsorptions. The O atoms of adsorbed H_2O and OH^- and the related adsorbent Cu^{2+} ions are denoted by $\text{O}_{\text{H}_2\text{O}}$, O_{OH} , $\text{Cu}_{\text{H}_2\text{O}^*}$, and Cu_{OH^*} , respectively. (d-f) are electron density of states (DOS) of (a-c), respectively, projected onto the denoted atoms; the upper/lower parts of (f) are DOS for different projected atoms, instead of spins. | 22 |
| Figure 3.6 Structures of CO_2 molecule at the solid/liquid interface of 0, 1 and 2 water molecules removed from the CuO surface. Explicit water molecules are illustrated using volume-filling clouds. | 25 |
| Figure 3.7 Structures of the singlet charged ($q = -1$) surface before (a) and after (b) CO_2 adsorption and doublet charged ($q = -2$) surface with CO_2 adsorption (c). (d-e) are electron density of states (DOS) projected onto denoted atoms of (a-c), respectively. The dotted vertical line indicates the Fermi level position of (d), while the solid vertical line indicates the Fermi level position of (e) and (f). | 26 |

| | |
|--|----|
| Figure 3.8 Schematics of the formate (HCO_2^-) formation on CuO surface structure through the proton transfer..... | 30 |
| Figure 3.9 Schematics of the carbon monoxide (CO) formation on CuO surface structure through the proton transfer..... | 30 |
| Figure 3.10 Adsorption configurations of polarized CO_2^{2-} , HCO_2^- , and CO molecule on CuO (111) (a-c, respectively) and Cu (100) (d-e, respectively) surface structures, together with the top-views as insets. | 32 |
| Figure 4.1 Atomic configuration for (a) Layered (L-LCO) and (b) Spinel (S-LCO) LiCoO_2 structures..... | 40 |
| Figure 4.2 Electron density of states (DOS) projected onto Li, Co and O atoms of the layered (upper) and spinel (lower) LiCoO_2 structures. The insets show the crystal orbital overlap population (COOP) analysis for each phase; the positive (negative) value indicates bonding (antibonding) characteristic of states at the related energies. The vertical lines indicate the Fermi level position. | 42 |
| Figure 4.3 Left: Atomic configuration of $\text{Li}_{0.98}\text{CoO}_2$ (1 Li vacancy illustrated as the black ball). Co in direct neighborhood to the vacancy (Co_{dir}), with linear connection to the vacancy via an O atom (Co_{lin}), far from the vacancy (Co_{far}), Co^{4+} ($4+$) and Co in direct neighborhood to Co^{4+} ($\text{Co}_{\text{dir}4+}$) are denoted, as been discussed by Laubach et al. Right: The electron density of states (DOS) projected onto the denoted Co atoms. | 44 |
| Figure 4.4 Atomic configuration of slab structures with related top-view of surfaces and surface energies shown in the middle; (a) Li-terminated L-LCO, (b) Co-terminated L-LCO, (c) Li-terminated S-LCO, (d) Co-terminated S-LCO, and (e) Li-terminated layered-spinel composite LiCoO_2 structure. | 46 |
| Figure 4.5 Left: The 1/2 ML Li-terminated layered LiCoO_2 (L-LCO) 2×2 slab structure consists of two equivalent Li atoms, connected with three O atoms, on each surface. Two types of O atoms and two types of Co atoms are in the second and third atomic layers, respectively: four-fold coordinated O (O_{4c}), five-fold coordinated O (O_{5c}); Co adjacent to two O_{4c} and one O_{5c} (Co_{445}), Co adjacent to two O_{5c} and one O_{4c} (Co_{554}). Right: The side view of the structure. | 48 |
| Figure 4.6 Electron density of states (DOS) projected onto surface Co and O, denoted in Fig 4, of the Li-terminated L-LCO (111) surface structure. The vertical line indicates the Fermi level position. | 49 |

Figure 4.7 Left: 1/2 ML O-terminated layered LiCoO_2 (L-LCO) 2×2 slab structure consisted of two Co^{3+} and Co^{4+} ions in the subsurface layer. The first and third atomic layers both contain two types of O ions, and two ions for each type: surface/subsurface O adjacent to two Co^{3+} and one Co^{4+} ($\text{O}_{3+}/\text{O}_{3+}$), surface/subsurface O adjacent to two Co^{4+} and one Co^{3+} ($\text{O}_{4+}/\text{O}_{4+}$). Right: The side view of (a) marked with the displacements (\AA) of atoms with respect to the Li-terminates surface structure. 53

Figure 4.8 Electron density of states (DOS) projected onto Co and O denoted in Fig 6(a) of (a) Li-deintercalated and (b) Li^+ -removed O-terminated LiCoO_2 surface structure,. The vertical line indicates the Fermi level position. 54

Figure 4.9 Left: 1/2 ML H-terminated 2×2 layered LiCoO_2 (L-LCO) slab structure consisted of two types of O ions on both first and third atomic layer; two types of Co ions on the second atomic layer in between: hydrogenated O (O_H), non-hydrogenated O (O_{3c}); Co adjacent to one O_H and two O_{3c} ($\text{Co}_{1\text{OH}}$), Co adjacent to two O_H and one O_{3c} ($\text{Co}_{2\text{OH}}$); subsurface O adjacent to two $\text{Co}_{1\text{OH}}$ and one $\text{Co}_{2\text{OH}}$ (O_{s1}), subsurface O adjacent to two $\text{Co}_{2\text{OH}}$ and one $\text{Co}_{1\text{OH}}$ (O_{s2}). Right: The side view of (a) marked with the displacements (\AA) of atoms with respect to the O-terminated surface structure. 56

Figure 4.10 Electron density of states (DOS) projected onto H, Co and O, denoted in Fig 8 (a), of H-terminated LiCoO_2 surface structure. The vertical line indicates the Fermi level position. 57

Figure 5.1 (a) Structure of the solid/liquid interface of H-terminated LiCoO_2 (111) surface structure in the explicit solvent model. (b)-(e) Electron density of states (DOS) projected onto the undercoordinated (O_{3c}) and hydrogenated ($\text{O}_{3c}(\text{H})$) O_{3c} atoms. The vertical line indicates the Fermi level position. 65

Figure 5.2 Structures of H-terminated surface connected to H-bond networks (4 water molecules) in the neutral (a,c) and positively charged (b,d) states. 67

Figure 5.3 Electron density of states (DOS) projected onto the 3-fold undercoordinated O atoms (yellow cross) on the surface structure of clustered 1H-removal (grey shaded), 2H-removal (blue), and 3H-removal (red) cases. The vertical line indicates the Fermi level position of the 1H-removal case. Insets are the zoom-in images indicated by white dotted line. 71

Figure 5.4 Structures of the adsorption configuration of $^*\text{OH}$ (a) and $^*\text{H}$ (b) on H-terminated surfaces. 73

- Figure 5.5** Electron density of states (DOS) projected onto Co and O atoms adjacent to the H-removal site on the surface structure before (a) and after (b) *OH adsorption on the 3-fold undercoordinated O (O_{3c}) atom. The vertical line indicates the Fermi level position of the 1H-removal case. 74
- Figure 6.1** Atomic configuration of spinel Co_3O_4 structure; Co and O atoms are illustrated by blue and red balls, respectively. 81
- Figure 6.2** Electron density of states (DOS) of Co_3O_4 bulk structure composed of high-spin (a) and low-spin (b) Co^{3+} ions, projected onto Co^{2+} (red), Co^{3+} (blue) ion and O (grey shaded). The vertical line indicates the Fermi level position (EF). 82
- Figure 6.3** (a) Stoichiometric polar (111) surface structure. (b) Nonstoichiometric nonpolar (111) O-terminated surface structure and the related top view (c). (d) Top view of 7/8 ML (d) H-terminated surface structure. (e) Top view of fully H-terminated surface structure. 85
- Figure 6.4** Electron density of states (DOS) of partially (a) and fully (b) H-terminated Co_3O_4 (111) surface structure. In (a), the DOS is projected onto Co^{3+} adjacent to $1O_{3c}/2HO_{2c}$ (green), $1HO_{3c}/2HO_{2c}$ (blue) and in the bulk (gray shade), and O_{3c} (red) atom. In (b), the blue denotes Co^{2+} ion adjacent to $1O_{3c}/2HO_{2c}$ 88
- Figure 6.5** *OH removal (0.13 ML) on Co_3O_4 (111) H-terminated surface structure 91
- Figure 6.6** Structures and electron density of states (DOS) of Co_3O_4 (111) H-terminated surface with adsorbate (a) $*O_2$ and (b) $*OOH$, projected onto Co^{3+} (blue), Co^{2+} (grey shaded) adjacent to the adsorbate, O of the adsorbate adjacent to the surface (red) and exposed to the solution (green). 92
- Figure 6.7** Illustration of in-plan H-bonding between HO_{2c} and OOH on Co_3O_4 (111) H-terminated surface structure. 96
- Figure 6.8** Free energy diagrams of the four-electron pathway for ORR on the Co_3O_4 (111) H-terminated surface structure. The red line represents the reaction at equilibrium (Φ_{eq}) potential corresponding to the zero electrode potential (0 V vs. RHE). The blue line represents the ORR potential (Φ_{ORR}) corresponding to the over potential (η) where all reaction steps along pathway are predicted downhill regarding to the free energies. The dashed line represents the theoretical open circuit potential. 98
- Figure 7.1** The atomic configuration of $LiFePO_4$ and $FePO_4$ with brown octahedra and pink tetrahedra represent FeO_6 and PO_4 units, respectively; Green and red balls represent Li and O atoms, respectively. 104

- Figure 7.2** The electron density of states (DOS) projected onto Li, Fe, P and O atoms in (a) LiFePO_4 and (b) FePO_4 with Fermi level indicated by dash line. 105
- Figure 7.3** (a) The DOS of PO_4 -deficient FePO_4 [note the intensity of O $2p$ state is rescaled by $1/3$]. (b) and (c) The band-decomposed charge densities corresponding to defect states I and II are plotted with an isosurface value of $0.005 \text{ electron/\AA}^3$. 107
- Figure 7.4** Variation in the relative formation energy of PO_4 -deficient FePO_4 in different charge states with respect to as a function of the Fermi level relative to the valence band maximum (E_v) for the computed FePO_4 bandgap around 1.75 eV 111
- Figure 7.5** The DOS of PO_4 -deficient LiFePO_4 in charge state (a) neutral, (b) $1+$, (c) $2+$ and (d) $3+$, respectively. The insets are enlarged DOS detail of localized states indicated by green arrow. The band-decomposed charge densities corresponding to those localized states are plotted with an isosurface value of $0.01 \text{ electron/\AA}^3$ 113
- Figure 7.6** Variation in the relative formation energy of PO_4 -deficient LiFePO_4 in different charge states with respect to as a function of the Fermi level relative to the valence band maximum (E_v) for the computed LiFePO_4 bandgap around 3.8 eV . 115
- Figure 7.7** The relative formation energy of PO_4 -deficient LiFePO_4 with $q = 0$ to $4+$ as a function of Li content (x) in the $\text{Li}_x\text{Fe}_N(\text{PO}_4)_{N-1}$ supercell ($N = 24$) with respect to the $x = N-3$ neutral case ($q = 0$). 116

Chapter 1 : Introduction

Since the mid-20th century, global warming has been observed to occur as a result of increasing CO₂ emissions. Climate change is expected to cause a series of problems such as sea level rise, food shortage and lack of clean water.¹ As continuous reliance on coal energy is expected, alternative technologies are needed to reduce CO₂ emissions from energy generation.^{2,3} In this regard, various electrochemical energy conversion/storage systems, such as fuel cells and Li-ion batteries, become crucial. In addition, other technologies supporting carbon-neutrality, such as CO₂ capture/conversion/storage, are also being pursued. While the metal-based materials have been successfully demonstrated as the catalysts for electrochemical systems, the widespread commercialization of their usages is still hindered by the high cost and insufficient lifetime. Among the alternative catalysts, transition metal oxides (TMO) is considered one of the most promising groups due to its low-cost, durability, and highly engineerable structures and electrical properties.

TMO have been intensely studied for a long period due to their fascinating properties, especially these last 20 years. TMO shows extraordinary diversity not only in scientific insights but also in the materialized and potential applications. In TMO, the natures of metal-oxygen bonds vary among nearly ionic, covalent and metallic.⁴ The varying properties of TMO materials significantly relates to the unique nature of outer *d*-electrons, which splits into different energy states when forming bonds with O 2*p* electrons in the matrices. Through manipulating the compositions or applying voltages to

the crystals, multivalent TMO systems can be created, which in turn offer greatly diverse electronic natures. In addition, the multi-component systems possess a wide variety of bulk/surface structures, which largely affect the electrochemical reactions performed in/on the matrices. In this dissertation, we use density functional theory (DFT) calculations to advance our understanding of how different metal oxide materials facilitate electrochemical reactions such as CO₂ reduction reaction (CO₂RR), oxygen evolution reaction (OER), oxygen reduction reaction (ORR), and lithiation process for Li-ion batteries. We hope these studies could be examples of how each of these systems demonstrates similar fundamental interactions generalizable to TMO. Prior to discussing these systems, theoretical background of DFT is introduced in Chapter 2.

In Chapter 3, the CO₂RR on CuO surface structure is investigated to understand the underlying mechanism behind the different selectivity between CuO and Cu surface. We first identified the solvated surface structure in the aqueous condition. Based on that, we studied the adsorption of polarized CO₂ on the neutral and negatively charged surfaces. Possible mechanisms for CO₂RR creating formate and CO are proposed. Finally, the comparison between CO₂RR catalyzed by CuO and Cu metal surface is discussed. Through this comparative study, we elucidate why CuO has higher selectivity toward formate than Cu while Cu metal has limited selectivity to formate.

In Chapter 4, the surface structures of LiCoO₂ in aqueous solution are studied thoroughly. We identified the most stable termination for LiCoO₂ (001) surface structure. Based on that, the phase transformation from spinel to layered phases near the surface driven by the Li/Co site exchange is proposed. The Li-, O-, and H-terminated surface

structures are investigated comprehensively. In addition, the hydrogenated surface structure formed through Li/H exchange at the solid/liquid interface is discussed. The findings provide a foundation to explore the possible mechanisms of the OER for non-metal terminated LiCoO_2 surface, as presented in Chapter 5. We found that the hole injection could induce deprotonation on the surface. Following that, the hydrogenation reaction of the surface may catalyze the OER.

In Chapter 6, we studied the ORR for Co_3O_4 structure. Based on the findings in Chapter 4, the H-terminated (111) surface structure was employed. The reaction steps of four-electron pathway are then investigated. In addition, the possible two-electron pathway is also proposed. Influences from the calculation methods are also discussed in the work. In Chapter 7, the properties of PO_4 -deficient $\text{LiFePO}_4/\text{FePO}_4$ structures are investigated. As the pristine $\text{LiFePO}_4/\text{FePO}_4$ crystals are used as the cathode materials in Li-ion batteries, we study the bulk, electronic and mechanical properties of their defected structures to understand how the presence of polyanion vacancies could potentially improve the performances. We assess the structure and binding nature of the defected matrices, together with the relative stabilities of the PO_4 -vacancies in various charged states. Thereafter, the bulk moduli of the structures are calculated to study the correlation between the presences of defects and flexibilities of the crystals.

Chapter 2 : Theoretical Background

2.1 SCHRÖDINGER EQUATION FOR MANY-BODY SYSTEM

In quantum mechanics, the probability of finding a particle in a finite space at time t is provided by Born's statistical interpretation:⁵

$$\int |\Psi(r,t)|^2 dr \quad (2.1.1)$$

where Ψ is the wavefunction of the particle and r is the coordination of the particle. The wavefunction is calculated by solving the Schrödinger equation:

$$i\hbar \frac{\partial \Psi}{\partial t} = -\frac{\hbar^2}{2m} \frac{\partial^2 \Psi}{\partial r^2} + V\Psi \quad (2.1.2)$$

where \hbar is the Planck's constant and V is the potential that the particle experiences.

For finding a stationary state of the particle, the equation is transformed to

$$E\Psi = -\frac{\hbar^2}{2m} \frac{\partial^2 \Psi}{\partial r^2} + V\Psi \quad (2.1.3)$$

And if we would like to find the wavefunctions for a many-body system, the equation is generalized in to

$$\hat{H}\Psi(R_1, R_2, \dots; r_1, r_2, \dots) = E\Psi(R_1, R_2, \dots; r_1, r_2, \dots) \quad (2.1.4)$$

where $\{R_i\}$ and $\{r_i\}$ correspond to the coordinates of nuclei and electrons, respectively, and the spins have been omitted for the simplicity. The Hamiltonian is composed of both the kinetic energy (\hat{T}) and potential (\hat{V}) operators:

$$\hat{H} = \hat{T} + \hat{V} \quad (2.1.5)$$

$$\hat{T} = \sum_I -\frac{\hbar^2}{2M_I} \nabla_I^2 + \sum_i -\frac{\hbar^2}{2m_i} \nabla_i^2 \quad (2.1.6)$$

$$\hat{V} = \frac{1}{2} \sum_{ij(i \neq j)} \frac{e^2}{|r_i - r_j|} - \sum_{Il} \frac{Z_l e^2}{|R_l - r_i|} + \frac{1}{2} \sum_{IJ(I \neq J)} \frac{Z_I Z_J e^2}{|R_I - R_J|} \quad (2.1.7)$$

where M (m) is the mass of nuclear (electron), e is the elementary charge and Z is the atomic number of the nuclear. According to the Born-Oppenheimer approximation,⁶ the first term of Eq. 2.1.6 can be ignored due to the relatively enormous mass of nuclei. In the description of quantum mechanics, physical observables are calculated to be the expectation value of related operators. For instance, the total energy is the expectation value of Hamiltonian regarding to the system of interest. Based on that, the ground state wavefunction can be determined by minimizing the total energy ($E = \langle \Psi | \hat{H} | \Psi \rangle$) respect to variables of $\Psi(\{r_i\})$.

2.2 HARTREE-FOCK THEORY

In the Hartree approximation,⁷ the electronic part of the many-body wavefunction is described by a single product of non-interacting single particle wavefunctions:

$$\Psi^H(r_1, r_2, \dots, r_N) = \varphi_1(r_1) \varphi_2(r_2) \cdots \varphi_N(r_N) \quad (2.2.1)$$

The total Hartree energy then becomes

$$E^H = \langle \Psi^H | \hat{H} | \Psi^H \rangle \quad (2.2.2)$$

$$= \sum_i \left\langle \varphi_i \left| -\frac{\hbar^2}{2m_e} \nabla_i^2 + V_{ion}(r) \right| \varphi_i \right\rangle + \frac{e^2}{2} \sum_{ij(i \neq j)} \left\langle \varphi_i \varphi_j \left| \frac{1}{|r-r'|} \right| \varphi_i \varphi_j \right\rangle \quad (2.2.3)$$

The first term of Eq. 2.2.3 contains the kinetic energy and the ion contribution to the potential (V_{ion}) while the second term contains the electron-electron interactions. In order to find ϕ_i , the variational principle is applied to Eq. 2.2.3, leading to the single particle Hartree equation:

$$\left[-\frac{\hbar^2}{2m_e} \nabla_i^2 + V_{ion}(r) + e^2 \sum_{j(i \neq j)} \left\langle \varphi_j \left| \frac{1}{|r-r'|} \right| \varphi_j \right\rangle \right] \varphi_i = \varepsilon_i \varphi_i(r) \quad (2.2.4)$$

Reflecting that solving ϕ_i required given ϕ_j , the Hartree equation needs to be solved by the variational principle and iterating method. To further consider the Pauli exclusive principle, the N-body wavefunction is written in a Slater determinant:⁸

$$\Psi^H = \begin{vmatrix} \varphi_1(r_1) & \varphi_1(r_2) & \cdots & \varphi_1(r_N) \\ \varphi_2(r_1) & \varphi_2(r_2) & \cdots & \varphi_2(r_N) \\ \vdots & \vdots & \ddots & \vdots \\ \varphi_N(r_1) & \varphi_N(r_2) & \cdots & \varphi_N(r_N) \end{vmatrix} \quad (2.2.5)$$

The wavefunction now fulfills the anti-symmetry with respect to an interchange of any position of two electrons. Given the single Slater determinant, the Hartree-Fock (HF) equation is written as:

$$\begin{aligned} & -\frac{\hbar^2}{2m_e} \nabla_i^2 \varphi_i(r) + V_{ion}(r) \varphi_i(r) + e^2 \left[\sum_{j(i \neq j)} \int \frac{|\varphi_j(r')|^2}{|r-r'|} dr' \right] \varphi_i(r) \\ & - \sum_{j(i \neq j)} \int \frac{dr'}{|r-r'|} \varphi_j^*(r') \varphi_i(r') \varphi_j(r) \varphi_i^*(r) = \varepsilon_i(r) \end{aligned} \quad (2.2.4)$$

In the electronic structure calculations, the predictions of the exchange and correlation energies are the most challenging part. The exchange energies are related to the anti-symmetry of electronic wavefunctions as expressed by the last term on the left hand side of Eq. 2.2.4. The correlation energies are related to the interaction between all electrons in the system. While the interaction between electron carrying parallel spins have been counted by the exchange energy term, the single Slater determinant is not sufficient to derive the complete correlation energies. Thus, the correlation energy is defined as the difference of true energy and energy calculated by using HF method.

2.3 DENSITY FUNCTIONAL THEORY

To solve for a better approximation of wavefunctions based on HF method, Density Functional Theory (DFT) was proposed in 1970s. The core foundation of DFT is Hohenberg-Kohn (HK) theorem,⁹ which states that: First, the expectation value of energy of a wavefunction is a unique functional of the electron density $\rho(r)$. Second, the lowest energy is only given by the functional when the $\rho(r)$ is the true ground state density. Accordingly, the electron energy functional is expressed as:

$$E[\rho] = T[\rho] + \int \hat{V}_{ext}(r)\rho(r)dr + V_{ee}[\rho] \quad (2.3.1)$$

where $T[\rho]$ is the kinetic energy of electrons, $\int \hat{V}_{ext}(r)\rho(r)dr$ is the electron-nucleus Coulomb potential energy, and $V_{ee}[\rho]$ is the Coulomb potential energy between electrons.¹⁰ The HK theorem reformulate the many-body problems based on the electron

density; yet, the analytic form of kinetic energy and electron-electron Coulomb potential energy are still unknown. In 1965, Kohn and Sham proposed to restate the intractable many-body problems to an equivalent set of non-interacting electrons under influence of effective potentials.¹¹ By introducing a fictitious system to describe N non-interacting electrons by single determinant, they rearranged the energy functional as

$$E[\rho(r)] = T_s[\rho] + V_{ext}[\rho] + V_H[\rho] + E_{xc}[\rho] \quad (2.3.2)$$

$$V_H[\rho] = \frac{1}{2} \int \frac{\rho(r_1)\rho(r_2)}{|r_1 - r_2|} dr_1 dr_2 \quad (2.3.3)$$

where T_s is the kinetic energy of non-interaction electrons and V_H is Hartree potential which includes a major portion of electron-electron Coulomb potential energy. Most importantly, the exchange-correlation functional, $E_{xc}[\rho]$, represents all the omissions of energy calculated based on the fictitious wavefunctions. With above, the Kohn-Sham equation is written as

$$\left[-\frac{\hbar^2}{2m_e} \nabla_i^2 + V_{ext}[\rho] + V_H[\rho] + E_{xc}[\rho] \right] \varphi_i(r) = \varepsilon_i \varphi_i(r) \quad (2.3.4)$$

which can be solved with a self-consistent scheme as briefly illustrated in Fig. 2.1.

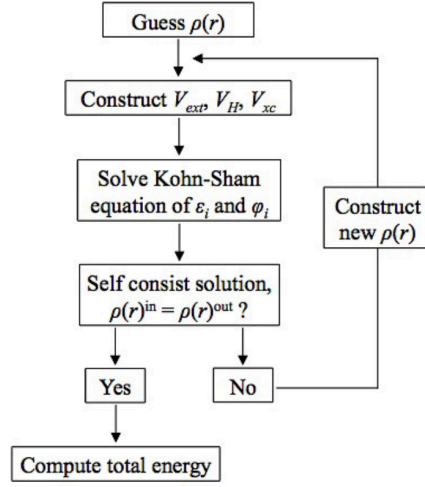


Figure 2.1 Self-consistent Kohn-Sham equation diagram.

2.4 EXCHANGE-CORRELATION FUNCTION

The competence of $E_{xc}[\rho]$ in closing the gap between true and calculated energies of the many-body system mostly determines the accuracy of DFT calculations. Two best known $E_{xc}[\rho]$ functionals were discussed briefly in this chapter: Local Density Approximation (LDA)¹² and Generalized Local Gradient Approximation (GGA)¹³. The basic concept of LDA is to treat electrons as a homogeneous electron gas.¹¹ That is, at each point in the system, the electron density of the rest of space is assumed to be the same at the very position. LDA works fine for the system with slow $\rho[r]$ change; however, for the system with steep $\rho[r]$ changes, the inadequate extrapolation of large $\rho[r]$ leads to the overestimation of binding energy. Inheriting the rational, GGA considers the gradient of the $\rho[r]$ in addition to the $\rho[r]$ itself. By including the gradient, GGA

improves the local limit of LAD; however, it is worth mentioning that the overcorrection leads to the well-known underestimation of binding energy. Widely used GGA functionals include the Perdew-Wang functional (PW91),¹⁴ Perdew-Burke-Ernzerhof (PBE)^{15,16} and others. While performing calculations, specifying the employed functionals is important as different functionals might provide results with discrepancies.

2.5 PSEUDOPOTENTIAL

In general, electrons of an ion can be decomposed into two parts: valence and core electrons. As illustrated in Fig 2.2, the wavefunctions of valence electron usually oscillate much less rapidly than the core counterpart, where r_c is the cut-off radius for core region. The differences are created by the change of electron-core binding strength spanning from the outer to inner shells. For the outer shells, valence electrons bound to the nuclear relatively loose. On the other hand, the core electrons bound strongly to the nuclear, leading to a stronger Coulomb interaction. The atomic-like nature of wavefunctions requires them to be orthogonal to core states. Thus, the wavefunctions rapidly oscillate. To describe these wavefunctions of all electrons (Ψ_{AE}) using plane-waves, a large basis set are needed, corresponding to numerous computational resources. To handle the issue, the general concept of pseudopotential is introduced.

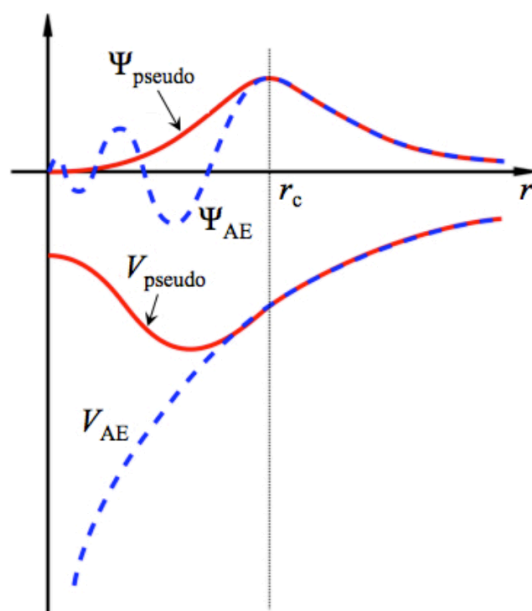


Figure 2.2 Comparison between pseudo and all-electron wavefunctions and pseudo and all-electron potentials.¹⁷

Considering that most of chemical reactions involve valence electrons much more strongly than core electrons, pseudopotential treats core electrons fixed as part of the nuclear, while the valence electrons are partially considered based on the essentiality of describing the electronic structures. As depicted in Fig 2.2, a pseudo-wavefunction, Ψ_{pseudo} (pseudopotential, V_{pseudo}) captures the same shape of Ψ_{AE} (all-electron potential, V_{AE}) outside the r_c , while reducing the nodes of Ψ_{AE} (V_{AE}) inside the r_c ; hence, reduces the computational cost. The pseudopotential built based on a larger r_c is considered softer, which is adopted for less expensive calculations along with the compromised accuracies.

The norm-conserving¹⁸ and ultra-soft¹⁹ are two common pseudopotentials. The former demands a reproduction of electron density beyond r_c while the latter loses that

criteria. Based on the concept of pseudopotential, the projected augmented method (PAW) was proposed to improve the computational efficiency by projecting the rapidly oscillating wavefunctions on to a smoother basis set.

Chapter 3 : Reaction Mechanisms for the Electrochemical Reduction of CO₂ on CuO (111) Surface

3.1 INTRODUCTION

The CO₂ reduction reaction (CO₂RR) is a crucial electrochemical conversion process in the carbon cycle. In CO₂RR, CO₂ molecules are transformed to various value-added carbon hydro compounds. The main problem hindering the application of the reaction is the high over-potential. In the past decades, several catalysts (eg. Cu, Fe, Ni, Ag, Pd) have been identified with different selectivity toward various products including CO, CH₄, C₂H₅OH and formate.^{20,21} Among these products, formate or formic acid (depending on pH values) is an attractive option for carbon-neutral applications. Formate salts are considered adequate chemical carriers in hydrogen storage and transportation.²² While transporting compressed hydrogen in gas or liquid phase is costly, using formate salts as chemical carriers provides a practical substitute to materialize the hydrogen economy. In the search for adequate catalysts, several recent studies have demonstrated the dependence of formate selectivity on the amount of surface oxides, as with the following examples. While *p*-block metals such as In, Sn, Hg and Pb are known for having formate as the main product of CO₂RR,^{23,24} removing the surface oxides from these structures has been shown to lower product yields.²⁵ Relatedly, increasing surface oxidation of electrodes such as tin and indium improves the yield.²⁶ As arguably the best-known metal catalyst, Cu metal has been shown to possess selectivity toward a large variety of products, including all aforementioned chemical compounds;²⁷ however, the

efficiencies for products other than the hydrocarbon compounds are relatively low.²⁸ In a previous work, Li et al. found that the copper electrodes synthesized with reduced Cu_2O films catalyze CO_2RR to form CO and formic acid with improved faradaic efficiencies compared to polycrystalline Cu metal.²⁹ In another recent experiment, Kang et al. found that CuO, CuFeO_2 and their composite materials photoelectrochemically reduce CO_2 to the formate anion at high selectivity.^{30,31} These works all suggest that the conversion of CO_2 to the formate anion is highly related to the presence of oxides on related host materials. In this Chapter, the CuO structure is investigated as a prototype system to better understand how incorporating O atoms into the structure could change the catalytic properties of Cu surfaces, which in turn facilitate the creation of formate. We first predicted the solvated CuO (111) surface structure in water solution to capture the adequate active surface for CO_2RR . Next, we studied the charged surface structures and related CO_2 adsorption configurations using both the implicit and explicit solvent models. Following that, different scenarios for proton interaction with polarized CO_2 to create formate or CO are proposed. The selectivity towards different products is then examined based on the differences in predicted enthalpies. Based on a similar reaction pathway, the selectivity of products for Cu (100) metal surface is also studied for comparison. Finally, the underlying mechanisms related to the different selectivity between CuO and Cu structures are discussed based on the nature of two materials.

3.2 METHODOLOGY

All atomic structures and energies reported herein were calculated using spin-polarized DFT within the generalized gradient approximation (GGA-PBE)^{15,16} as implemented in the Vienna Ab initio Simulation Package (VASP)^{32,33}. The projected augmented wave (PAW) method^{34,35} with a plane-wave basis set was employed to describe the interaction between ion core and valence electrons. To treat the strong on-site *3d* electron-electron interactions on Cu an additional Hubbard-U was added with an effective value of $U_{\text{eff}} = 7.14 \text{ eV}$ ³⁶. For the hybrid-DFT calculations, the HSE06 (Heyd-Scuseria-Ernzerhof)³⁷ exchange-correlation functional was employed with a short-range screening factor of 0.2 and the portion of exact HF exchange potential of 25%.

The pristine CuO structure was modeled using an 8-atom unit cell. An energy cutoff of 450 eV was applied for the plane-wave expansion of the electronic eigenfunctions. For geometry optimization and energy calculations, all atoms were fully relaxed using the conjugate gradient method until residual forces on constituent atoms became smaller than $1 \times 10^{-2} \text{ eV/\AA}$. For Brillouin zone sampling, (6×6×6) k-point mesh in the scheme of Monkhorst-Pack³⁸ was used for the structure. For the surface studies, the periodic (2×2) and (4×4) slabs with thickness of 5 and 3 Cu-layers are employed for different cases, respectively; slab structures are separated by a vacuum of 15 Å in the (111) direction. The Monkhorst-Pack type k-point sampling of (3×3×1) and (2×2×1) was used for (2×2) and (4×4) surface structures, respectively. To simulate the aqueous conditions, the implicit solvent model³⁹ was employed in all the surface calculations,

while explicit water molecules were also considered in some cases to study the influence on the charge transfer and stability of structures.

3.3 RESULTS AND DISCUSSION

3.3.1 Bulk Properties of CuO Structure

CuO exhibits a monoclinic structure with each Cu (O) atom connected to four O (Cu) atoms, as shown in Fig. 3.1. The crystal structure consists of CuO_4 square polyhedra formed by Cu^{2+} and O^{2-} ions. In experiments, the monoclinic CuO phase is reported to be antiferromagnetic. The spin ordering adopted in this work [Fig. 3.1] is selected among different magnetic arrangements to best predict the bulk properties such as the lattice constant and gap energy. The lattice constants are predicted to be $a= 4.619$, $b= 3.549$ and $c= 5.139 \text{ \AA}$ with $\gamma= 97.57^\circ$, in close agreement with experimental data ($a= 4.684$, $b= 3.423$ and $c= 5.129 \text{ \AA}$ with $\gamma= 99.54^\circ$).⁴⁰ Due to the variance of lattice parameters predicted by the earlier works^{41,42}, the experiential data of lattice constants is used in this work. Meanwhile, no significant difference of total energy and electronic structures are found between structures predicted using calculated and experimentally measured lattice constants.

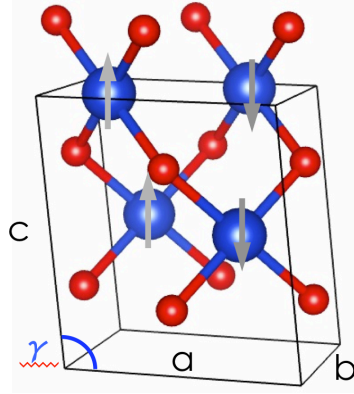


Figure 3.1 Atomic configuration of unit cell of CuO structure. Arrows denotes the spin alignments.

Figure 3.2 (a) shows the electron density of states (DOS) projected onto the Cu and O atoms of CuO structure predicted using the DFT+U method. The top of the valence band (VB) mainly consists of O 2*p* overlapped with minor Cu 3*d* states, while the bottom of the conduction band (CB) is the opposite case, with major Cu 3*d* and minor O 2*p* states, matching with the earlier theoretical studies.^{43,44} An energy gap of ~ 1.44 eV is predicted, recapturing experimental measurement (1.2–1.9 eV) well.^{45,46,47} In the valence band, nonbonding Cu 3*d* states are predicted in the energy range from -8 to -4 eV, while overlap of Cu 3*d* and O 2*p* states are predicted between -4 to -2 eV. The overlap is mostly attributed to the half-filled $d_{x^2-y^2}$ state of square planar Cu²⁺ ion as the electronic state being highly directional toward adjacent O 2*p* states. Relatedly, the hybridization of Cu 3*d* and O 2*p* electrons was also hinted at previous experimental work.⁴⁸ From -2 eV to Fermi level, the O 2*p* nonbonding states are mostly predicted along with minor overlap with Cu 3*d* states. Compared to DFT+U, the hybrid functional HSE06 predicts more

significant overlap of $3d$ and $2p$ states is predicted in the energy range from -4 eV to Fermi level, likely attribute to that the better localization of electrons reducing the antibonding interactions [Fig. 3.2 (b)].

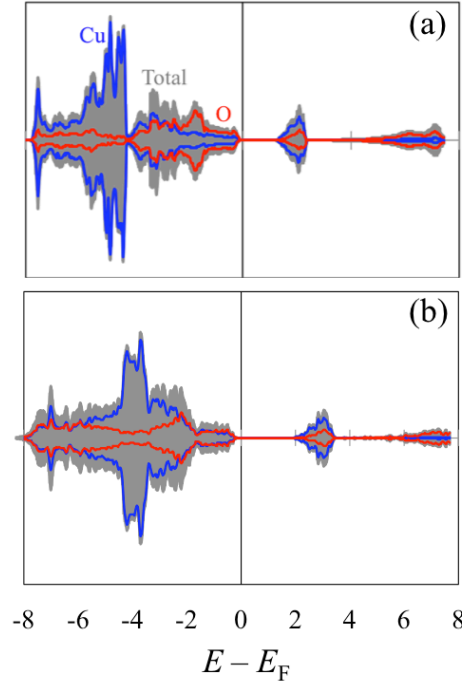


Figure 3.2 Electron density of states (DOS) projected onto Cu (blue) and O (red) atoms of CuO structure, predicted using: DFT+U (a) and HSE06 (b). The vertical line indicates the Fermi level position.

3.3.2 CuO (111) Surface Structure

The CuO (111) surface is reported to be one of the most stable facets in both experimental and theoretical studies.^{49,50,51} We predicted the surface energy to be 0.76

J/m^2 , a good match with pervious theoretical workss.^{52,53} Figure 3.3 shows the atomic configuration of the surface structure.

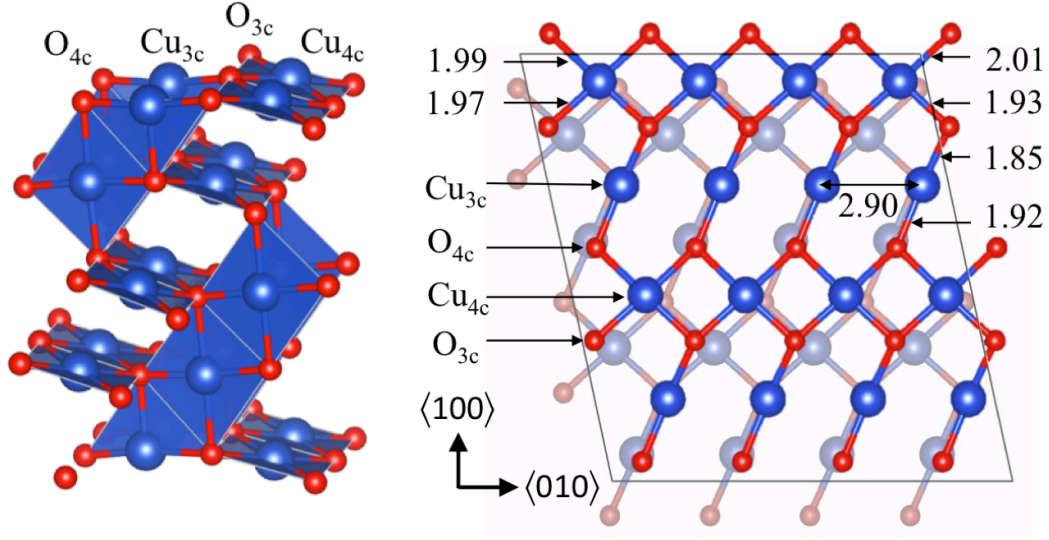


Figure 3.3 Structure of CuO (111) surface. Left: Side-view of the slab structure with denotations of 3-fold undercoordinated Cu (Cu_{3c}), 4-fold coordinated Cu (Cu_{4c}), 3-fold undercoordinated O (O_{3c}), and 4-fold coordinated O (O_{4c}) atoms. Right: Top-view of the surface. Distances (Å) of Co – O and Co_{3c} – Co_{3c} are indicted.

The surface is composed of the same amount of Cu and O atoms with two types of coordination for each element: undercoordinated 3-fold Cu (Cu_{3c})/ O (O_{3c}) or coordinated 4-fold Cu (Cu_{4c})/ O (O_{4c}). Cu and O are arranged in separated rows parallel to each other in the $\langle 010 \rangle$ direction. Each row consists of atoms with the same type of coordination. Alternating rows in an order of Cu_{3c} - O_{3c} - Cu_{4c} - O_{4c} span the surface. A Cu_{3c} atom is adjacent to an O_{3c} , O_{4c} and O atom in the subsurface layer, forming a defected (3-fold) square planar ($\angle \text{O}_{3c}$ - Cu_{3c} - $\text{O}_{4c} \approx 172^\circ$) perpendicular to the surface. Meanwhile, a Cu_{4c} atom is adjacent to two O_{3c} and O_{4c} atoms, remaining a square planar parallel to the

surface. An O_{3c} atom connected to a Cu_{3c} and two Cu_{4c} atoms is predicted to be the most exposed atom. While O_{4c} is also connected to a Cu_{3c} and two Cu_{4c} atoms, the O atom connects to a Cu atom in the subsurface layer, making O_{4c} the least exposed atom; O_{4c} is located more inward than O_{3c} by about 0.5 Å.

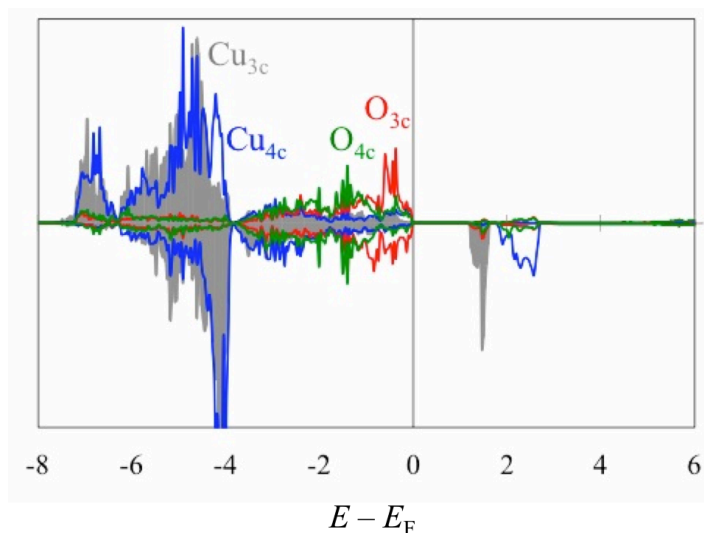


Figure 3.4 Electron density of states (DOS) of CuO (111) surface structure, projected onto Cu_{3c} (grey), Cu_{4c} (blue), O_{3c} (red) and O_{4c} (green) atoms. The vertical line indicates the Fermi level position.

Figure 3.4 shows the DOS projected onto surface Cu and O atoms. The VB and CB are consisted of mainly O_{3c} 2p and Cu_{3c} 3d states, respectively. The gap energy is predicted to be 1.1 eV (~ 0.3 eV narrower than the bulk structure), indicating the undercoordinated square planar Cu_{3c} has a relatively unstable unpaired electron. In addition, the smaller coordination number of Cu_{3c} than Cu_{4c} could also contribute to the lower CB, as the antibonding interaction related to the perspective excess electron is

reduced. On the other hand, the pronounced O_{3c} $2p$ states are predicted to be pronounced at the VB because of the weakened electron localization.

3.3.3 Adsorption of H_2O on CuO (111) Surface

Water solvated surface structures are comprehensively examined using implicit solvent model considering 1/4 and 1/2 ML water coverage. Between two types of coordinations of Cu^{2+} ions on the surface, we found that water molecules only adsorb on Cu_{3c}^{2+} ions. On the 1/4 ML water-solvated surface structure, the distance of H_2O and Cu_{3c} is predicted to be 2.08 Å. Meanwhile, H_2O forms a hydrogen bond with the nearest O_{3c} atom, as shown in Fig. 3.5 (a). The adsorption energy is calculated to be -0.42 eV (-0.62 eV in vacuum). The configuration is the same as predicted by Zhang et al.⁵⁴, while the adsorption energy is smaller by about 0.2 eV; the discrepancy could be due to the absence of Hubbard correction and different functional employed in the the earlier work. In the DOS analysis [Fig. 3.5 (d)], the solvated surface O_{3c} $2p$ states become less pronounced near VB, compared to the unsolvated surface structure, which can be attributed to the stabilization out of hydrogen bonding interaction. Meanwhile, a significant overlap of Cu_{3c} $3d$ states and O_{H_2O} $2p$ states are predicted between -6 and -2 eV, suggesting the electron sharing between two atoms; the result supports the chemisorption of water on CuO surface observed by Chen et al.⁵⁵

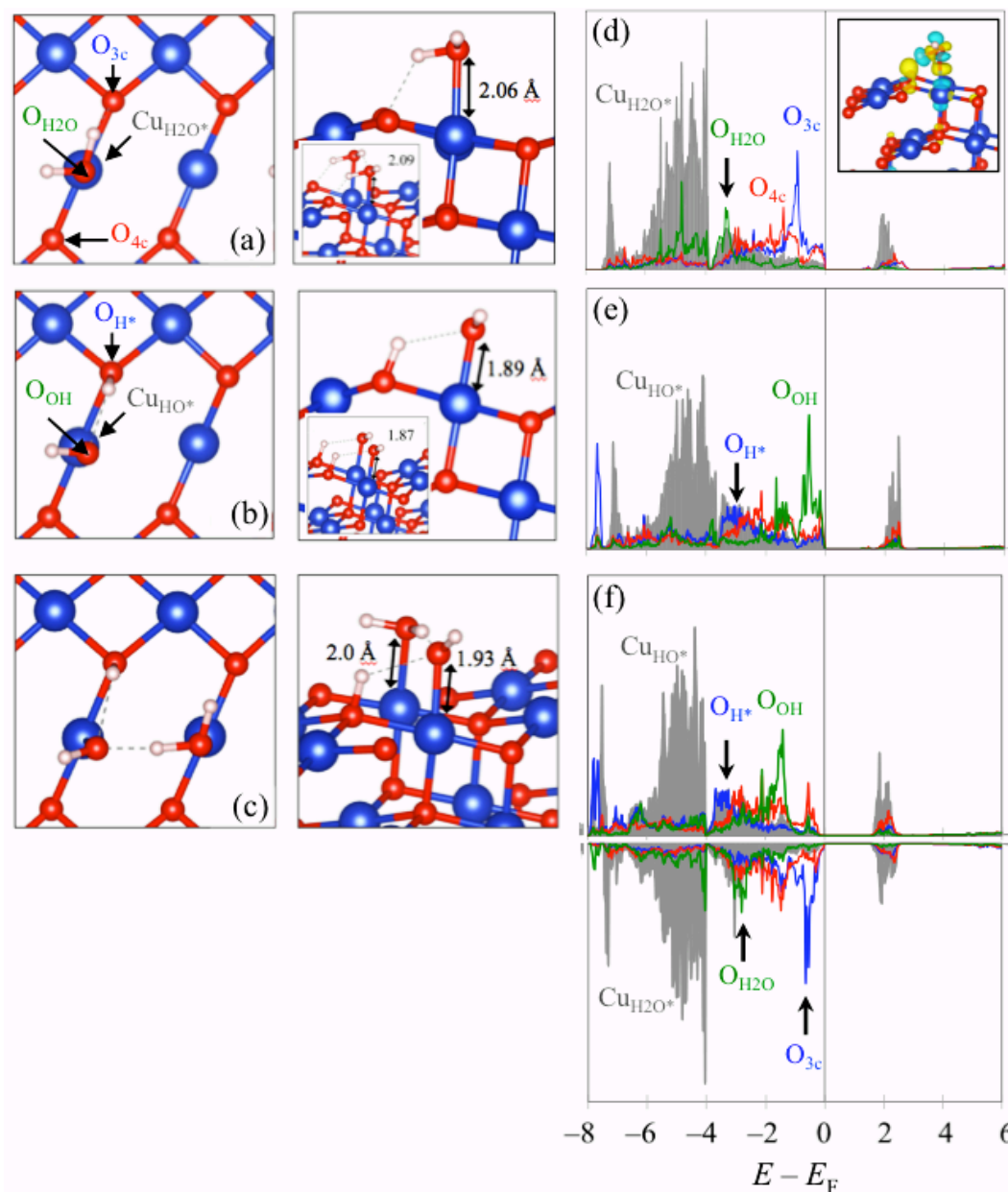


Figure 3.5 Structures of H₂O-adsorption on surfaces: 0.25 ML H₂O (a), 0.25 ML dissociative H₂O (b), and 0.5 ML non-dissociative/dissociative H₂O (c) adsorptions; insets are the 0.5 ML cases for related adsorptions. The O atoms of adsorbed H₂O and OH⁻ and the related adsorbent Cu²⁺ ions are denoted by O_{H2O}, O_{OH}, Cu_{H2O*}, and Cu_{OH*}, respectively. (d-f) are electron density of states (DOS) of (a-c), respectively, projected onto the denoted atoms; the upper/lower parts of (f) are DOS for different projected atoms, instead of spins.

The inset of Fig. 3.5 illustrates the charge difference created by water adsorption. The electron population is increased between H₂O and Cu_{3c}²⁺ ion, and also near the lattice O atoms adjacent to Cu_{3c}²⁺, while being decreased around Cu_{3c} ion. Considering that defected square planar Cu_{3c}²⁺ ion has an unpaired electron in $3d_{x^2-y^2}$ states pointing to the solution, the redistribution of electron could be attributed to the recovery of coordination due to water adsorption. In fact, the same rational also explains why water molecules do not adsorb on Cu_{4c}²⁺ ion as the $3d_z^2$ states pointing to the solution are filled and stable.

For 1/2 ML H₂O solvated surface structure, water molecules form hydrogen bonds with neighboring water molecules, as shown by the inset of the Fig. 3.5 (a). The adsorption energy per water molecule is calculated to be ~ -0.4 eV, implying the adsorption energy is concentration independent. Figure 3.5 (b) shows the configuration of 1/4 ML dissociative water solvated surface. The dissociation energy of water molecule is calculated to be 0.03 eV with OH⁻ and H⁺ ions being adsorbed on Cu_{3c}²⁺ and O_{3c}, respectively; the distance of OH⁻ and Cu_{3c} is predicted to be 1.89 Å. The dissociation energies are predicted to be the same for 1/2 ML case [inset of Fig. 3.5 (b)], being independent of the concentration. Figure 3.5 (e) shows the DOS of the dissociative adsorption case. The protonation reaction on O_{3c} atom largely stabilizes the Cu_{3c}²⁺-O_{3c} antibonding interaction, resulting in a major downshift of the 2*p* states. Meanwhile, unpaired O_{OH} and O_{4c} 2*p* states are predicted to be pronounced right below Fermi level, suggesting that the slight distribution of *OH 2*p* electrons toward Cu_{3c}²⁺ ion could partly compromise the overall stability of configuration. On top of that, we found the dissociation energy is highly related to the hydrogen bonding networks connected to the

created OH^- anions. Namely, surrounding water molecules could facilitate the water dissociation reaction. For the case of two water molecules paired via hydrogen bond on the surface [Fig. 3.5 (c)], the dissociation energy of a H_2O molecule is predicted to be -0.43 eV, much smaller than the 0.25 ML case. As shown in Fig. 3.5 (f), with assistance from neighboring water molecule via hydrogen bonding interaction, the overlap of O_{OH} , O_{4c} $2p$ and Cu_{3c}^{2+} $3d$ states are predicted to shift downward, implying the enhancement of localization of OH^- $2p$ electrons. The localization is assisted by the $\text{OH}_2\text{-OH}$ hydrogen bonding interactions, which in turn weaken the antibonding interaction of O_{4c} and Cu_{3c}^{2+} ions. Accordingly, the surface terminated with 0.25 ML H_2O mixed with 0.25 ML OH/H could be the most stable structure in aqueous condition.

3.3.4 Adsorption of CO_2 on CuO (111) Surface

The adsorptions of polarized CO_2 molecule on the metal atoms of catalytic surfaces is widely considered crucial steps in the CO_2 reduction reaction (CO_2RR) pathway. The configuration provides a relatively low energy for transfer of charge to CO_2 , which in turn facilitate the interaction with the protons in the environment.^{56,57,58,59} Here we investigated the interaction between CO_2 molecule and Cu atoms at the solid/liquid interface while considering surface structure at various charge states.

In the neutral state ($q = 0$), we find CO_2 molecule does not adsorb on the surface structure with either end- or side-on configuration. Therefore, the replacement energy of CO_2 and an adsorbed water molecule is basically similar to the water adsorption energy,

about 0.8 eV for a fully solvated surface as discussed in the Section 3.3.2. The energetically unfavorable event implies the importance of water desorption reaction for CO_2 to approach the surface.

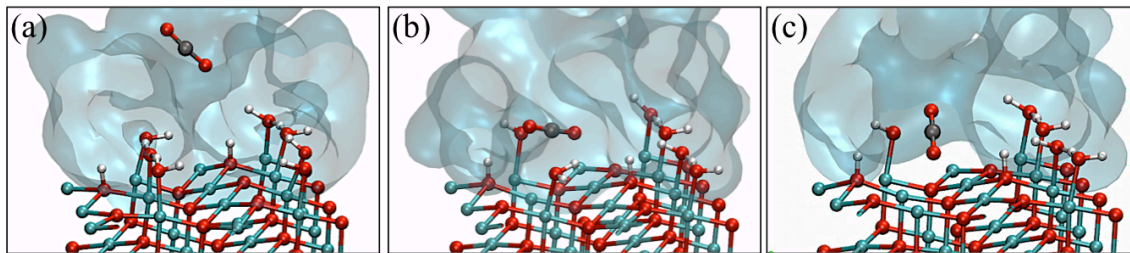


Figure 3.6 Structures of CO_2 molecule at the solid/liquid interface of 0, 1 and 2 water molecules removed from the CuO surface. Explicit water molecules are illustrated using volume-filling clouds.

In the slab structure with an additional electron ($q = -1$), the Fermi level is predicted to shift up by ~ 0.7 eV, similar to the overpotential for CO_2RR to create CO and formate on Cu metals.⁶⁰ The excess charge is predicted to localize on a 3-fold coordinated Cu^{2+} ion on the extreme surface, reducing the Cu_{3c}^{2+} ion to Cu_{3c}^{+} . The energy difference between electron localized in bulk and on the surface structure is predicted to be ~ 0.7 eV. Following that, a H_2O molecule is predicted to desorb from the Cu_{3c}^{+} ion, creating an open-site on the solvated surface structure. Using explicit solvent model, CO_2 molecule staying near surface via the open-site is calculated to be energetically more favorable than in bulk solution by about 0.5 eV [Fig. 3.6 (a)], attributed to the presence of vacuum space on top of the open-site [Fig. 3.6 (b)]. We further found that the H_2O molecule sitting next to the open-site slightly shifts away (outward) from adsorbent Cu^{2+} ion by

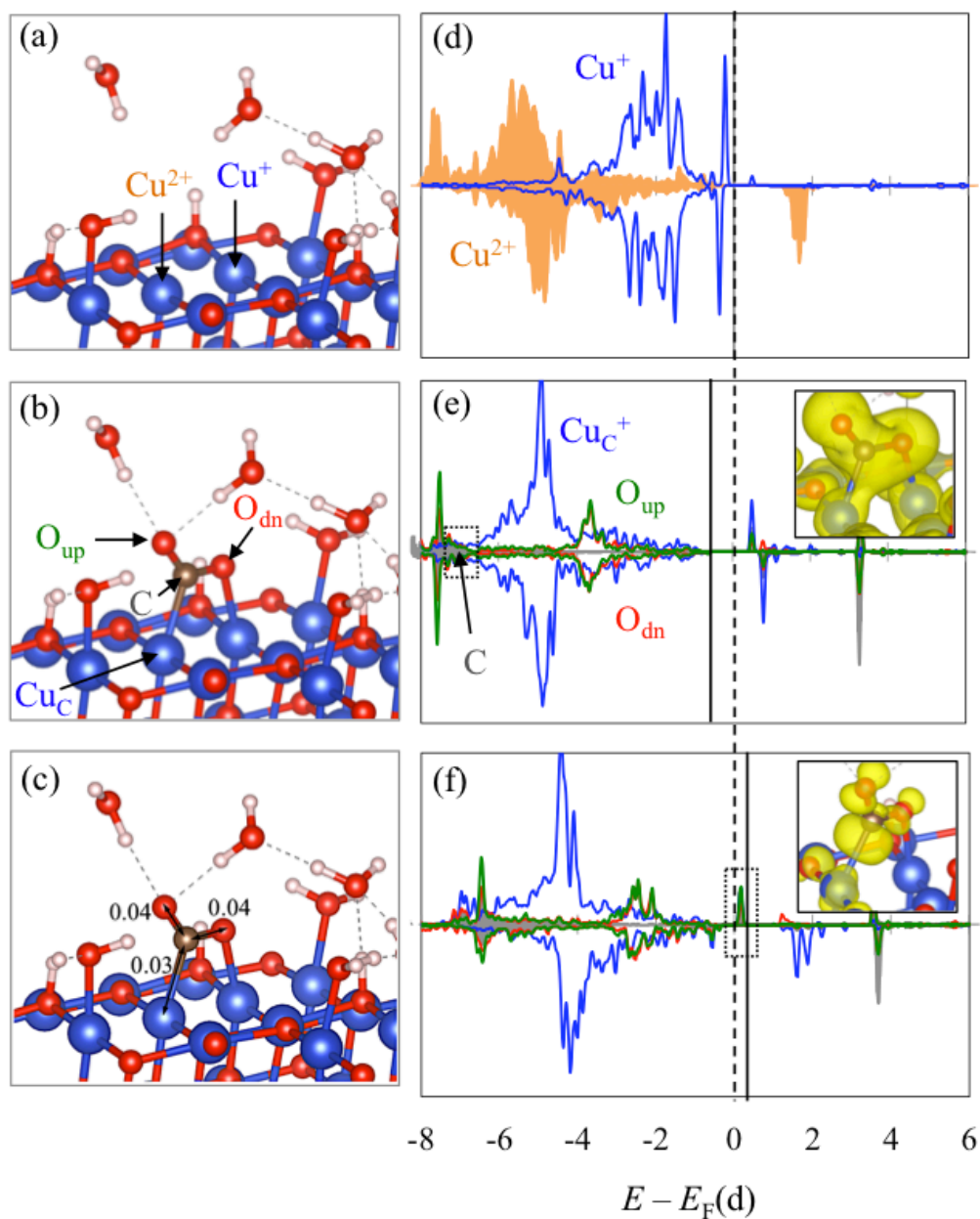


Figure 3.7 Structures of the singlet charged ($q = -1$) surface before (a) and after (b) CO₂ adsorption and doublet charged ($q = -2$) surface with CO₂ adsorption (c). (d-e) are electron density of states (DOS) projected onto denoted atoms of (a-c), respectively. The dotted vertical line indicates the Fermi level position of (d), while the solid vertical line indicates the Fermi level position of (e) and (f).

about 0.1 Å, indicating the $\text{H}_2\text{O}\cdots\text{Cu}^{2+}$ bond is weakened due to the decreasing of support from neighboring H_2O molecule. We predicted the desorption of H_2O molecule to be energetically favorable (~ -0.3 eV). As shown in Fig. 3.6 (c), the extra space created by the second water removal better accommodates the CO_2 molecule, which has limited solubility in the water solution.

We then looked into the electronic structure of the reduced surface. Figure 3.7 (a) shows the surface structure with two H_2O molecules removed from Cu^+ and Cu^{2+} ions. An excess electron is localized on the Cu^+ ion adjacent to a H-terminated O_{3c} ; the proton stabilizes the related $\text{Co}^+ - \text{O}$ bond. Figure 3.7 (d) shows the DOS projected onto the Co^+ and Co^{2+} ions. The VB and CB consist of filled Cu^+ and half-filled $\text{Cu}^{2+} 3d x^2-y^2$ states, respectively. The significant upshift of Cu^+ $3d$ bands implies that the reduction reaction reduces the local stability of the surface structure. With the two open-sites of Cu^+ and Cu^{2+} ions on the surface, the bidentate $\text{CO}_2^{\delta-}$ chemisorption is predicted with the C and an O atom (O_{dn}) bonding to $\text{Cu}_C^{(1+\delta)-}$ and Cu_{3c}^{2+} ions, respectively [Fig. 3.7 (b)]. The $\text{C} - \text{O}_{dn}$ bond is parallel to the surface while $\text{C} - \text{O}_{up}$ bond tilts toward the solution, spanning an angle of $\sim 45^\circ$ with the surface. The bond length of $\text{C} - \text{Cu}_C$, $\text{C} - \text{O}_{dn}$ and $\text{C} - \text{O}_{up}$ are predicted to be 1.94, 1.26 and 1.24 Å, respectively. In the related DOS [Fig. 3.7 (e)], the Fermi level is predicted to shift down by ~ 0.5 eV with respect to the case before the adsorption. Both VB and CB are constituted of mainly $\text{Cu}_C 3d$ states hybridized with C and O $2p$ states, indicating the electron transfer from Cu_C to the CO_2 molecule. The notably stabilized $\text{Cu}_C 3d$ states suggest that the charge transfer weakens the $\text{Cu}_{3c}^+ - \text{O}$ antibonding interaction. Meanwhile, the hybridization of C $2p$ states and $\text{Cu}_C 3d$ states is

predicted to span an energy range of $-10 \sim -8$ eV below Fermi level. The decomposed electron density distribution, as shown in the inset of Fig. 3.7 (e), demonstrates an electron sharing between C and Cu_C ions, implying the bonding-state nature of this hybridization. The predicted decreasing (increasing) of antibonding- (bonding-) state interactions facilitate the polarization of CO_2^δ . It is worth mentioning that the hydrogen-bonding network effectively stabilizes the adsorption configuration. Compared with solely implicit solvent calculation, the adsorption configuration predicted using explicit water molecules is energetically more favorable by ~ 0.3 eV. Using ab-initio molecular dynamics (AIMD), the configuration is predicted to remain at 300K for longer than 9 ps.

For the injection of a second electron for the surface structure with bidentate CO_2 adsorption, the Fermi level shifts up for about 0.7 eV, similar to the first electron injection. Besides the Cu_C^+ ion, no additional Cu^+ ion is predicted in this doublet charged slab structure ($q = -2$), suggesting that the excess electron does not localize on another Cu^{2+} ion. At the meantime, the adsorption configuration remains similar on the structure. In the DOS of $q = -2$ case [Fig. 3.7 (f)], the VB is predicted as localized states consisted of C $2p$ and Cu $3d$ electrons, indicating that the excess electron is localized between Cu_C and C atoms. Meanwhile, the bond distances of C – O_up , C – O_dn and C – Cu_C increase by 0.04, 0.04 and 0.06 Å, respectively [Fig. 3.7 (c)], implying the antibonding nature of the localized states. Furthermore, the decomposed electron density distribution of VB also demonstrates a limited electron sharing between C and Cu ions [inset of Fig. 3.7 (f)]. The antibonding interaction weakens the $\text{Cu}_\text{C} - \text{C}$ bond, which could in turn facilitate the

interactions between the adsorbed CO_2 and surrounding protons. Additionally, the configuration is tested by AIMD to remain stable at 300K for longer than 6 ps.

3.3.5 Selectivity Toward Formate Anion and CO Molecule

Figure 3.8 and 3.9 illustrate the possible proton transfer reactions near surface to polarized CO_2^{2-} , transforming the CO_2^{2-} to formate anion (HCO_2^-) and CO molecule, respectively. As discussed in Section 3.3.4, the adsorption structures of CO_2 molecule are stabilized through H-bonding interaction with surrounding H_2O molecules. As illustrated in Fig. 3.8 (a), the adsorbed H_2O molecule on the Cu^{2+} site (next to the Cu_C site) could interact with the O_up atom of CO_2 as a H-bond donor. With an assist of the H-bonding interaction on stabilization, a proton could be transferred to $\text{CO}_2^{(1+\delta)-}$, reacting with the carbon atom; a HCO_2^- anion is then created as the already weakened $\text{C}-\text{Cu}_\text{C}$ bond being broken [Fig. 3.8 (b)]. The reaction is predicted to be exothermic for about -0.2 eV. This mechanisms are similar to the CO2RR for Ru-dihydride species discussed by Kovacs et al.⁶¹ During the reaction, the adsorption of a bridge OH^- anion on two Cu^{2+} ions is predicted to stabilize the newly opened Cu^{2+} site. The total energy drops by another ~ 0.3 eV after another water molecule from solution is adsorbed on the Cu^{2+} site, as shown in Fig. 3.8 (c).

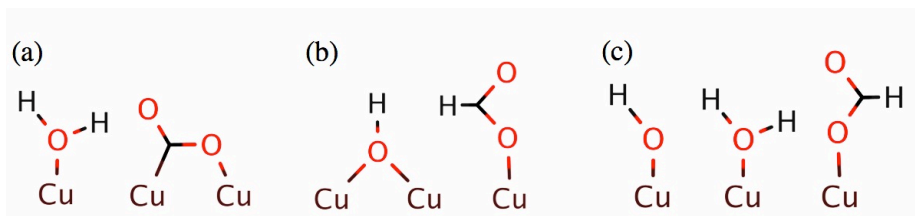


Figure 3.8 Schematics of the formate (HCO_2^-) formation on CuO surface structure through the proton transfer.

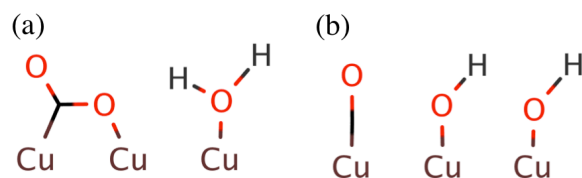


Figure 3.9 Schematics of the carbon monoxide (CO) formation on CuO surface structure through the proton transfer.

On the other hand, the adsorbed H_2O molecule next to the Cu_{Odn} site could interact with the O_{dn} atom of CO_2^{2-} [Fig. 3.9 (a)]. Through the proton transfer reaction, the $\text{C} - \text{O}_{\text{dn}}$ bond breaks, resulting in the creation of an end-on adsorbed CO molecule and OH^- anion on the surface [Fig. 3.9 (b)]. The structure of each adsorption configuration is illustrated in Fig 3.10 (a-c). Using the implicit solvent model, the enthalpy (ΔH) of forming HCO_2^- in CO2RR ($^*\text{CO}_2^{2-} + \text{H}_2\text{O} \rightarrow ^*\text{HCO}_2^- + ^*\text{OH}^-$) for the CuO (111) surface structure is predicted to be more favorable than CO molecule ($^*\text{CO}_2^{2-} + \text{H}_2\text{O} \rightarrow \text{CO} + 2\text{OH}^-$) by 1.09 eV, corresponding to the experimental results that the CuO structure has a higher selectivity toward HCO_2^- anion.⁶² A similar result of 1.15 eV is predicted using HSE06

functional. (For the consistency of surface structures and adequate comparisons with Cu metal, the unsolvated surface structures in the implicit solvent model are considered.) Finally, the end-on adsorption energy of HCO_2^- anions and CO molecule is predicted to be about -0.7 eV and -0.4 eV, respectively. More importantly, when an electron is injected to the slab, the adsorbent Cu^{2+} ion is reduced Cu^+ , notably weakening the bonds of HCO_2^- anion or CO molecule to the surface. Therefore, the nature of localization of excess charges at adsorbent Cu^{2+} ions could prevent the possible surface positioning from related products during the CO2RR.

3.3.6 Selectivity for CuO (111) and Cu (100) Surface

Based on the reaction mechanisms, we predicted the reaction enthalpy for CO2RR on the Cu (100) metal surface. The structure of each adsorption configuration is illustrated in Fig. 3.10 (d-f). The adsorptions on bridging sites are considered as the same configuration for CO_2 adsorption on Cu metal was also predicted by Cheng et al.⁵⁹ The ΔH of forming HCO_2^- anion is calculated to be more favorable than CO molecule by 0.27 eV. This predicted exothermic reaction corresponds to the fact that Cu metal has small selectivity for formate. Meanwhile, the much smaller magnitude than the CuO case (by 0.82 eV) suggests to the experimental observation that CuO structure has relatively high selectivity toward HCO_2^- anion than Cu metal.^{29,63,64}

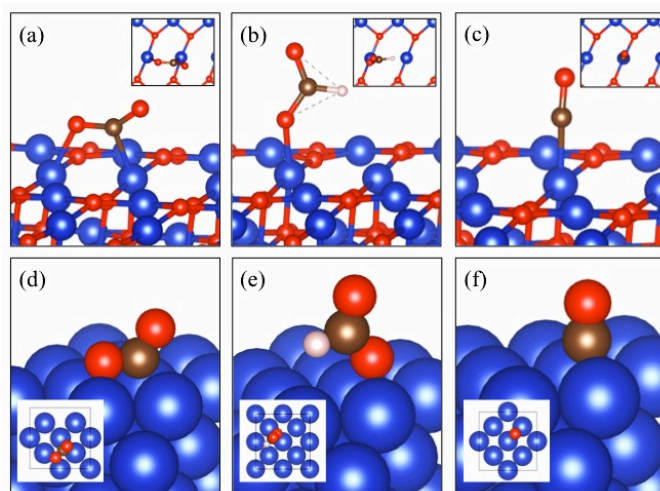


Figure 3.10 Adsorption configurations of polarized CO_2^{2-} , HCO_2^- , and CO molecule on CuO (111) (a-c, respectively) and Cu (100) (d-e, respectively) surface structures, together with the top-views as insets.

| Adsorbate | CuO (111) | Cu (001) |
|--------------------------------|--------------------------------|-------------------|
| CO | $-0.36 [-0.31]_{\text{HSE06}}$ | -0.85 |
| HCO_2^- (monodentate) | $-0.74 [-0.72]_{\text{HSE06}}$ | -0.73 |
| HCO_2^- (bidentate) | -1.29 | -0.90 |

Table 3.1 Adsorption energies of CO and HCO_2^- anions on CuO (111) and Cu (100) surface structure. Energies calculated using the hybrid functionals (HSE06) are in the square parenthesis.

Table 3.1 summarizes the adsorption energy of HCO_2^- anion and CO molecule on CuO and Cu metal surfaces. First of all, the limited differences between the energies predicted using DFT+U and HSE06 suggest that the charge distributions at the cleaved surface are described well with Hubbard correction method. Next, we noticed that the aforementioned differences of enthalpies for forming HCO_2^- and CO are mostly

attributed to the discrepancy in CO adsorption energies as the adsorption energies of HCO_2^- anions are similar in both materials. The more exothermic CO adsorption reaction on Cu metal than CuO (by -0.49 eV) supports the CO2RR to be more selective toward CO. On the other hand, the weaker binding strength of C – Cu could results in the formation of HCO_2^- anions. At this point, on top of these findings, three facts contributing to the higher selectivity of CO2RR toward HCO_2^- anion for CuO than Cu metal are summarized: First of all, in spite of the adsorptions of polarized CO_2^{2-} molecules are predicted on both materials, injecting additional electrons to weaken the related C – Cu bond is found difficult for Cu surface. As matter of fact, excess electrons are delocalized in Cu metal. Without the bond weakening process, the stable Cu – C bond could lead to the formation CO molecule, as shown in Fig 3.9. In a previous study, Peterson and Nørskov have pointed that adequate binding strengths of CO on the surfaces are essential for catalysts to create methane.⁶⁵ Thus, the relatively high adsorption energy of CO could also be related to why Cu metal is able to catalyze the CO2RR to create derivative hydrocarbon compounds (eg. methanol and ethanol).^{58,59,66} Second, once HCO_2^- anions are created on the surface, the desorption of HCO_2^- anion from CuO surface could be faster than Cu metal, considering that the electron localization facilitates the desorption reactions. On the other hand, the excess electrons might tend to further catalyze the adsorbates on Cu surface. And finally, considering that C atom of the bidentate adsorbed CO_2^{2-} is bounded with Cu_C , O_up and O_dn atoms, for protons to interact with C, the assists from surrounding H_2O molecules on the proton transfer could be crucial. Based on that, the water network on the hydrophilic CuO (111) surface structure

[Section 3.3.3] would facilitate the formation of HCO_2^- reaction. On the contrary, Cu (100) surface has much weaker interaction with water molecules. Without the help from the adequate water network, as a result, protons have relatively high probability to interact with O_{dn} , leading to the creation of CO molecules and related hydrocarbon compounds on Cu metal.

3.4 SUMMARY

Based on DFT-GGA calculations, the CO_2 reduction reaction (CO2RR) for CuO (111) surface structure is investigated. Starting with the surface structure, we identified the solvation configuration of CuO (111) surface. In the water solution, H_2O molecules are predicted to only adsorb on the 3-fold undercoordinated Cu^{2+} ions, which represent half of the Cu^{2+} ions on the surface. Using implicit solvent model, H_2O molecules are predicted to dissociate into protons (adsorbed on surface 3-fold O_{3c} atoms) and $^*\text{OH}^-$ (adsorbed on the 3-fold Cu^{2+} ions). We noted that the dissociation is greatly facilitated by other adsorbed H_2O molecules, which form H-bonds with the $^*\text{OH}^-$ anions. Based on that, the surface structure is predicted to be solvated with 50% of both OH^- anion and H_2O molecules adsorbed on the 3-fold Cu^{2+} ions. As CO_2 molecule barely interacts with the Cu^{2+} ions on the neutral surface, the removal of H_2O is crucial for CO2RR to happen. By injecting an electron to the slab structure, a H_2O molecule is predicted to desorb from the surface as the adsorbent Cu^{2+} ion being oxidized to Cu^+ . Following that, the system becomes energetically more favorable when the CO_2 molecule stays near the open site

(Cu^+), compared to being in the bulk solution. The water removal destabilizes the binding strength of neighboring adsorbed H_2O molecule to the surface Cu^{2+} ; the desorption of the H_2O molecule is then predicted as the extra space near surface better accommodate the CO_2 molecule spanning two open site (Cu^+ and Cu^{2+}). Afterward, the bidentate adsorption configuration of CO_2 is predicted with the C and an O atom bonded to the Cu^+ and Cu^{2+} , respectively. The DOS analysis illustrates the C $2p$ and Cu $3d$ binding states, implying the polarization of CO_2 through the charge sharing. Relatedly, the antibonding interaction of the original $\text{Cu}^+ - \text{O}$ bond in the lattice is largely reduced. By injecting another electron to the surface structure, the C $2p$ and Cu $3d$ antibonding states are predicted at VB, indicating the weakening of the C – Cu bond. The reactions of the polarized CO_2 transforming to HCO_2^- and CO are proposed via proton interacting with C and O of CO_2 , respectively. Based on the difference of enthalpies for both reactions, forming HCO_2^- on the surface is predicted to be more favorable than CO by 1.09 eV. We then calculated the difference of enthalpies for Cu (100) surface based on the same measures. Compared to CuO (111) surface, the tendency for Cu metal to create HCO_2^- during CO₂RR is less favorable by ~0.8 eV, implying a higher selectivity toward HCO_2^- for CuO than Cu metal. Finally, our calculations show that products of CO₂RR manage to desorb from CuO surface when additional electrons are injected to the structures, due to the reduction of adsorbent Cu^{2+} to Cu^+ which weakens the bonding strength of products. Contrarily, the desorption of the same products from metal surfaces might be difficult, considering their natures of having itinerant charges.

Chapter 4 : Structure and Stability of LiCoO₂ Surface

4.1 INTRODUCTION

Improving the efficiency of catalytic oxygen evolution/reduction reaction (OER/ORR) relies on the development of electrocatalyst with high turnover rates at low overpotentials. Metal-based electrocatalysts such as Pt, RuO₂ and IrO₂ are known for their high performances,^{67,68,69,70} whereas the rareness of these precious metals keeps the catalysts of this kind from being economically attractive.⁷¹ Additionally, the formation of insulating Pt oxides and poorly performing high-valent RuO₂ derivatives also hinder the implementation of these materials as catalysts.⁷⁰

In the search for promising low-cost substitutions, Co-based compounds have been studied extensively and proven competitive with precious-metals and their oxides for both OER and ORR catalysis.^{72,73,74,75} As one of the most widely studied Co-based metal oxides, LiCoO₂ receives great attention regarding its engineerable electronic structure based on the tunable lithium content of the matrix and the synthesis flexibility through doping with a variety of transition metals. By electrochemically extracting Li atoms from the matrix, Lu et al. reported an improvement on the catalyzing performance of partially delithiated LiCoO₂ structures,⁷⁶ which were also reported to be able to work as OER/ORR bifunctional catalysts by Maiyalagan et al. in a different work.⁷⁴ In another study of delithiated LiCoO₂ structure, Augustyn et al. pointed out that the morphology and electronic structures of Ni- and Fe-doped matrices change with different doping levels, further implying the rich variability of the properties of doped LiCoO₂.⁷²

While extensive studies have shed light on the potential of LiCoO_2 being a promising OER/ORR catalyst, the structure and composition of the active surface and the catalyzing mechanism still remain unclear. Some previous studies suggested that the active surface contains Co ions as the active sites, however it could be disputed considering undercoordinated metal atoms are reported to induce high surface energies in metal oxides.⁷⁷ In a previous work, the phase transformation of LiCoO_2 to Co_3O_4 surface structure was observed after the catalyzing reaction,⁷⁸ suggesting the environmental dependence on surface structure of the metal oxides. Meanwhile, as the incorporation of protons into partially delithiated metal oxides in the aqueous conditions has been studied in experiments,⁷⁹ possible hydrogenated surface structures of metal oxides are also within the scope of this work. In a study of synthesizing monolayered cobalt oxides, Kim et al. successfully exfoliated the protonated partially delithiated layered LiCoO_2 to form a thin layer of cobalt oxide, suggesting that the protonation reaction could stabilize the cobalt oxide thin film due to proton stability on the related surface.⁸⁰ In a theoretical study, Benedic et al. predicted the reaction free energy for the H^+/Li^+ ion exchange of LiCoO_2 to be lower than other selected metal oxides such as the layered Li_2MnO_3 and olivine LiFePO_4 ,⁸¹ implying possible correlation of the protonation reaction and the host metal ion type.

In this chapter, we studied the properties of the LiCoO_2 surface structure with various terminations. LiCoO_2 has two well known phases: Layered (L-LCO) and spinel-like (S-LCO) LiCoO_2 structures, which are synthesized at about 900 °C and 400 °C, respectively.⁸² To predict the most stable surface structure of LiCoO_2 in aqueous

condition, we first studied the bonding nature of the bulk structure for both phases of the crystal. Following that, we calculated the surface energy for various terminations, influencing the phase transformation of the surface structure. We then looked into the properties of delithiated and hydrogenated surface structures. This particularly highlights the stabilization due to the hydrogenation reaction of O-terminated.

4.2 METHODOLOGY

All atomic structures and energies reported herein were calculated using spin-polarized DFT within the generalized gradient approximation (GGA-PBE)^{15,16} as implemented in the Vienna Ab-initio Simulation Package (VASP).^{32,33} The projected augmented wave (PAW) method^{34,35} with a plane-wave basis set was employed to describe the interaction between ion core and valence electrons. To treat the strong on-site $3d$ electron-electron interactions on Co an additional Hubbard-U was added (with an effective value of $U_{\text{eff}} = 4.91$ and 5.62 eV for layered and spinel-like structures, respectively).⁸³ The HSE (Heyd-Scuseria-Ernzerhof)⁸⁴ exchange-correlation functional with a short-range screening factor of 0.2 was employed for the hybrid-DFT calculations. The portion of exact HF exchange potential of 15 and 25% are considered. Considering the undetermined electrical properties of cleaved surface structure, the electron density of states (DOS) of surface structures are calculated using HSE hybrid-functional with 15% exact HF exchange potential to better predict the atomic orbitals. Valence configurations employed are as follows: $1s^2 2s^1$ for Li, $3d^7 4s^2$ for Co, and $2s^2 2p^4$ for O. An energy cutoff

of 450 eV was applied for the plane-wave expansion of the electronic eigenfunctions. For geometry optimization and energy calculations, all atoms were fully relaxed using the conjugate gradient method until residual forces on constituent atoms became smaller than 1×10^{-2} eV/Å. The pristine LiCoO₂ was modeled using a 48-atom (2×2×1) supercell while the Li-deficient structures were created by removing a Li atom from expanded (3×3×1) and (4×4×1) supercells. For Brillouin zone sampling, (3×3×1) k-point mesh in the scheme of Monkhorst-Pack³⁸ was used.

The surface structure was modeled using a periodic (2×2) slab with a thickness of 10 oxygen-layers and a vacuum of 10 Å in (001) and (111) directions for layered (L-LCO) and spinel (S-LCO) LiCoO₂ structures, respectively. Surface relaxations are predicted in the region from the top to the forth oxygen-layer and become negligible beyond the depth, where the matrices start to exhibit the corresponding bulk-like structure. The terminating atoms, either Li or Co, are evenly distributed on the two surfaces to cancel the polar electrostatic field, which often leads to electron redistribution and results in high surface energies.^{85,86,87} While non-polar L-LCO slab structures remain stoichiometric, non-polar spinel S-LCO slab structures are built non-stoichiometrically by replacing a Co (three Li) with three Li (a Co) atoms for Li- (Co-) rich surface. Non-polar S-LCO surface structures terminated by either Li or Co atoms are modeled while the valence state of all Co³⁺ ions are maintained.

The formation energies of Li₂O- (O-) vacancy on the surface structure are calculated with the formula: $E_f(V_{Li_2O/O}) = 1/2 [E_{slab}(V_{Li_2O/O}) + 2E(Li_2O/O) - E_{slab}(Li-/O-termination)]$, where $E_{slab}(V)$ is the total energy of the slab structure with a Li₂O (O)

vacancy on each side of the $1/2$ ML Li- (1ML O-) terminated surface, E_{slab} is the total energy of the regarding termination and E is the total energy of Li_2O ($1/2 \text{ O}_2$) molecule.

4.3 RESULTS AND DISCUSSION

4.3.1 Bulk Properties of LiCoO_2

As illustrated in Fig. 1, LiCoO_2 exhibits the rock salt crystal structure, in which O anions form a distorted close-packed array and Li^+ and Co^{3+} cations are located in the octahedral sites.

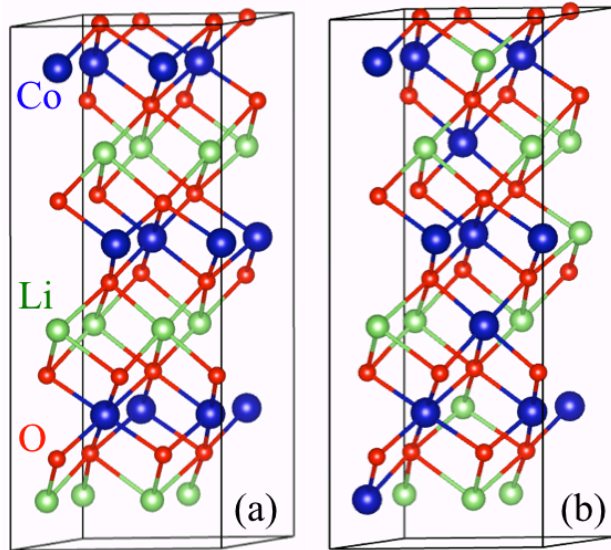


Figure 4.1 Atomic configuration for (a) Layered (L-LCO) and (b) Spinel (S-LCO) LiCoO_2 structures.

This structure has alternating planes of oxygen and metal ions. In layered LiCoO_2 (L-LCO) [Fig. 4.1 (a)], each metal layer consists of either Li^+ or Co^{3+} ions. In spinel

LiCoO₂ (S-LCO) [Fig. 4.1 (b)], mixed Li₃Co and LiCo₃ layers alternate; note that the spinel structure differs from the layered structure in that a quarter of the metal ions are swapped between the different metal layers. The predicted volumes of L-LCO and S-LCO are 32.97 and 32.89 Å³ per formula unit (f.u.), respectively, in good agreement with the experimental values of 32.28 and 32.23 Å³/f.u.⁸⁸; the small discrepancy in calculated and experimental results is due to the well-known underestimation of binding strength in the GGA calculation. The lattice constants and bond lengths calculated by DFT, DFT+U and hybrid-DFT methods are summarized in Table 4.1 and Table 4.2.

| | Exp. | DFT+U (U= 4.91) | Hybrid DFT (15%) | Hybrid DFT (25%) |
|---|-------------|--------------------|---------------------|---------------------|
| a, c (Å) | 5.64, 14.06 | 5.67, 14.21 | 5.64, 14.06 | 5.61, 14.04 |
| Co—O (Å) | | 1.94 | 1.92 | 1.91 |
| Li—O (Å) | | 2.12 | 2.10 | 2.09 |
| Gap (eV) | 2.7 | 2.70 | 2.37 | 3.77 |
| Total energy per formula unit (eV) | | 21.869 | 30.996 | 35.350 |

Table 4.1 The bulk properties of layered LiCoO₂ (L-LCO) structure (lattice constants, bond distances, gap energies and total energy per formula unit) predicted using DFT+U and hybrid functionals, together with the experimental data (Exp.) for comparison. The portions of exact HF exchange potential are in parentheses.

| | Exp. | DFT+U (U= 4.91) | Hybrid DFT (15%) | Hybrid DFT (25%) |
|---------------------------------------|-------------|--------------------|---------------------|---------------------|
| a, c (Å) | 5.64, 13.89 | 5.71, 13.98 | 5.66, 13.87 | 5.64, 13.80 |
| Co—O (Å) | | 1.94 | 1.92 | 1.91 |
| Li—O (Å) | | 2.10 | 2.09 | 2.08 |
| Gap (eV) | | 2.97 | 2.40 | 3.80 |
| Total energy per formula unit (eV) | | 21.859 (U=4.91) | 30.989 | 35.338 |

Table 4.2 The bulk properties of spinel LiCoO₂ (S-LCO) structure (lattice constants, bond distances, gap energies, and total energy per formula unit) predicted using DFT+U and hybrid functionals, together with the experimental data (Exp.) for comparison. The portions of exact HF exchange potential are in parentheses.

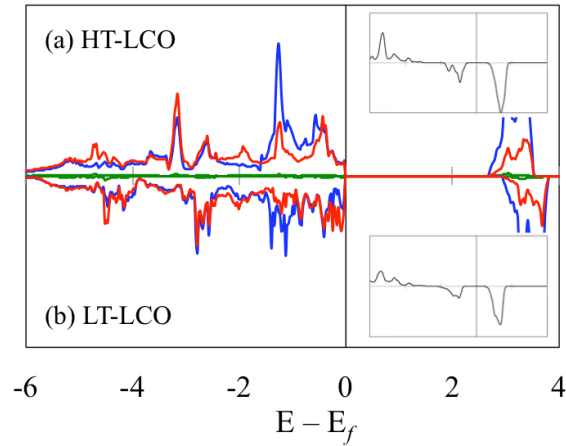


Figure 4.2 Electron density of states (DOS) projected onto Li, Co and O atoms of the layered (upper) and spinel (lower) LiCoO₂ structures. The insets show the crystal orbital overlap population (COOP) analysis for each phase; the positive (negative) value indicates bonding (antibonding) characteristic of states at the related energies. The vertical lines indicate the Fermi level position.

Figure 4.2 shows the electron density of states (DOS) projected onto the atomic orbitals of L-LCO [(a)] and S-LCO [(b)]. In LiCoO₂, the t_{2g} and e_g states of Co³⁺ are

completely filled and empty, respectively. The predicted gap of 2.37 and 2.40 eV for the L-LCO and S-LCO phases, respectively, shows good agreement with the experimentally measured value of 2.4~2.7 eV.^{89,90} The gaps predicted for L- and S-LCO by hybrid-DFT method are 2.70 and 2.97 eV, respectively. The upper valence band ($-2 \sim 0$ eV) is mainly composed of Co $3d$ nonbonding states with slight $3d-2p$ antibonding characteristics, while the lower valence band ($-6 \sim -2$ eV) is of $3d-2p$ bonding states, as demonstrated by crystal orbital overlap population (COOP) analysis (see insets of Fig. 4.2). The S-LCO structure has marginally broadened Co $3d$ and O $2p$ states near the Fermi level compared to the L-LCO structure. The slightly increased antibonding characteristics in the S-LCO structure could be related to the presence of cubane-like Co_4O_4 units, which have a more compact atomic arrangement compared to LiCo_3O_4 in L-LCO. Our calculation predicts the S-LCO phase to be 0.01 eV/f.u. less favorable than the L-LCO using both DFT+U and hybrid-DFT methods (see Table 1 and 2), implying that the S-LCO is less stable than L-LCO but to a small degree.

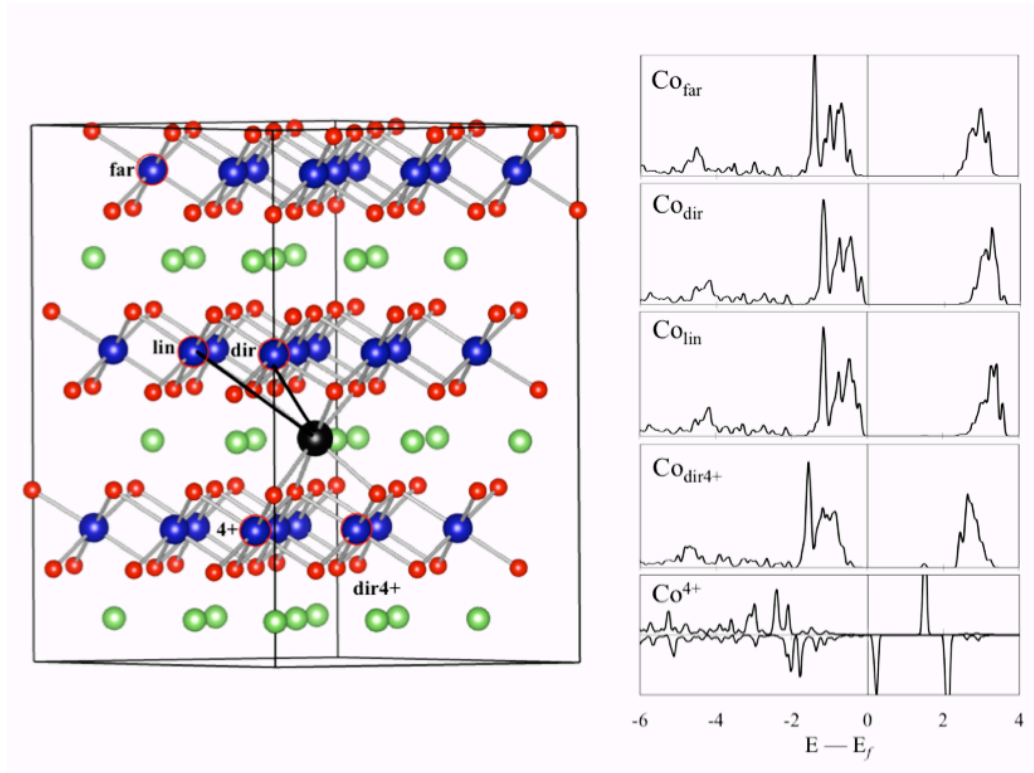


Figure 4.3 Left: Atomic configuration of $\text{Li}_{0.98}\text{CoO}_2$ (1 Li vacancy illustrated as the black ball). Co in direct neighborhood to the vacancy (Co_{dir}), with linear connection to the vacancy via an O atom (Co_{lin}), far from the vacancy (Co_{far}), Co^{4+} (4+) and Co in direct neighborhood to Co^{4+} ($\text{Co}_{\text{dir}4+}$) are denoted, as been discussed by Laubach et al⁹¹. Right: The electron density of states (DOS) projected onto the denoted Co atoms.

To understand the influence of Li removal on the LiCoO_2 surface structures, we first investigate the Li-deficient bulk structure. The Li-deficient system is constructed by removing a Li atom from the supercell containing 48 Li atoms (2.1% Li-deficiency) [Fig. 4.3]. Due to the loss of electrostatic attraction from the Li^+ ion, six undercoordinated O ions adjacent to the vacant octahedral site displace outward from the vacancy center by $\sim 0.04 \text{ \AA}$. Figure 4.3 shows the DOS of Li-deficient L-LCO as projected onto the atomic orbital of Co at various positions relative to the vacancy and Co^{4+} ion. In the DOS, an

empty state splitting from $\text{Co}^{4+} 3d\text{-}t_{2g}$ bands is predicted at the bottom of conduction band (CB). Due to the decreased amount of valence electrons, $\text{Co}^{4+} 3d$ states are in the energy range from -6 to -2 eV lower than $\text{Co}^{3+} 3d$ states from -2 to 0 eV and the $\text{Co}^{4+} - \text{O}$ bond lengths are shortened by averagely 0.04 \AA on average. Both Co_{dir} and Co_{lin} $3d$ states shift to higher level with respect to the bulk-like Co^{3+} ion. It is worth noting that $\text{Co}_{\text{adj}4+}$ $3d$ states are slightly stabilized because of the shortened $\text{Co}^{4+} - \text{O}$ bonds ease of the decreasing of $\text{Co}_{\text{adj}4+} - \text{O}$ bond length, thus reducing the antibonding interaction. Meanwhile, the Co_{dir} $3d$ states are predicted at slightly higher energy than Co_{lin} due to the shorter $\text{Co} - \text{O}$ bond lengths. Similar binding natures are also predicted in the S-LCO electronic structure. The delithiation voltage of the L-LCO structure is predicted to be 3.98 V , slightly lower than S-LCO (4.06 V), in agreement with the result reported by Van der Ven et al.⁹² The higher voltage could be attributed to the more symmetric structure of S-LCO which allows less relaxations in the Li-deficient matrix.

4.3.2 Dependence of Surface Energy on Termination

To search for the most stable $[111]$ LiCoO_2 surface structure, we calculated the surface energy for different terminations and phases comprehensively. Figure 4.4 illustrates the atomic configuration of four types of non-polar slab structures: (a) stoichiometric $1/2$ ML Li-terminated L-LCO structure (Li-L), (b) stoichiometric $1/2$ ML Co-terminated L-LCO structure (Co-L), (c) non-stoichiometric $3/4$ ML Li-terminated S-LCO structure (Li-S) and (d) non-stoichiometric $1/4$ ML Co-terminated S-LCO structure

(Co-S). The surface energy (γ) is calculated by the formula: $\gamma = (E_s - nE_b)/2A$, where E_s is the total energy of the slab structure containing n LiCoO_2 units, E_b is the total energy per formula unit and A is the area of each surface of the slab structure. Our calculation predicts $\gamma(\text{Li-L})$ and $\gamma(\text{Co-L})$ to be 1.12 and 2.40 J/m^2 , respectively, indicating that the Li-terminated surface is more stable than the Co-terminated surface. The results match the known fact that the coordination loss of transition metal on surface often causes a high surface energy for the related compound.

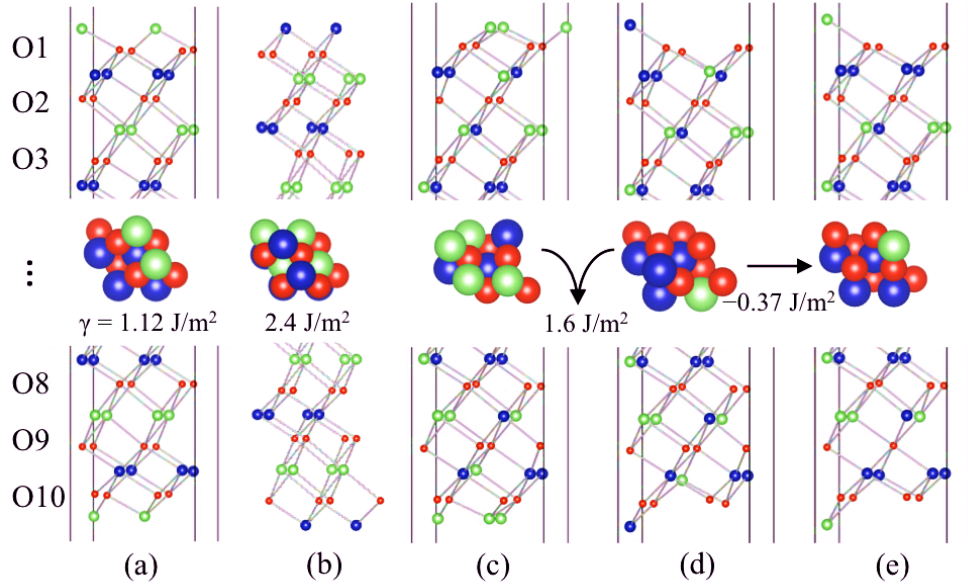


Figure 4.4 Atomic configuration of slab structures with related top-view of surfaces and surface energies shown in the middle; (a) Li-terminated L-LCO, (b) Co-terminated L-LCO, (c) Li-terminated S-LCO, (d) Co-terminated S-LCO, and (e) Li-terminated layered-spinel composite LiCoO_2 structure.

To calculate the surface energy of stoichiometric S-LCO structure (Li/Co-S), we took the average of E_s (Li-S) and E_s (Co-S) as the average stoichiometry is the same as

in pristine S-LCO; $\gamma(\text{Li/Co-S})$ is calculated to be 1.60 J/m^2 . The energy difference of 0.48 J/m^2 between $\gamma(\text{Li-L})$ and $\gamma(\text{Li/Co-S})$ would indicate the Li-terminated L-LCO slab is the more stable surface, rather than S-LCO. We note that the S-LCO slab structure has the subsurface metal layer composed of one (1) Li and three (3) Co atoms. In light of the tendency of undercoordinated Co ions tend to destabilize the surface, we investigated the possible surface reconstruction of switching a Co atom on the surface and a Li atom in the subsurface layer. The site switching results in the three atomic layers of the L-LCO structure on top of the S-LCO bulk structure, i.e. a layered-spinel composite structure. The calculation predicts that the formation of the composite structure decreases the surface energy by 0.37 eV compared to the Co-terminated spinel structure, corresponding to the occurrence of phase transformation near surface as reported in the earlier experiment.⁷⁴ Therefore, being the most representative surface structure of LiCoO_2 , the properties of the Li-terminated L-LCO surface structure are thoroughly studied in this work.

4.3.3 Li-terminated Surface Structure

Figure 4.5 shows the atomic configuration of the $1/2 \text{ ML}$ Li-terminated L-LCO surface structure. Li ions on the surface displace toward the slab structure almost perpendicularly by $\sim 0.36 \text{ \AA}$; three Li-O bonds are shortened by similar amount of $0.25 - 0.26 \text{ \AA}$ with respect to bulk structure (2.12 \AA). A small inward displacement of the second atomic layer (O-layer) by $\sim 0.01 \text{ \AA}$, coupled with the recapture of bulk structure

beyond the third layer, implies a minor adjustment of the Li-terminated surface structure. The distances of selected Co – O bonds are summarized in Table 4.3. In the subsurface layer, compared to Co – O bonds in bulk structure (1.94 Å), Co₄₄₅ – and Co₅₅₄ – O_{4c} are decreased by 0.02 – 0.03 Å, while Co₄₄₅ – and Co₅₅₄ – O_{5c} distances are predicted to be slightly increased by 0.01 – 0.02 Å. The slight shrinkages of Co – O_{4c} bond are attributed to the smaller coordination number of O atoms. Meanwhile, the elongation of Co – O_{5c} bonds could be a secondary effect of the shortened Co – O_{4c} bonds.

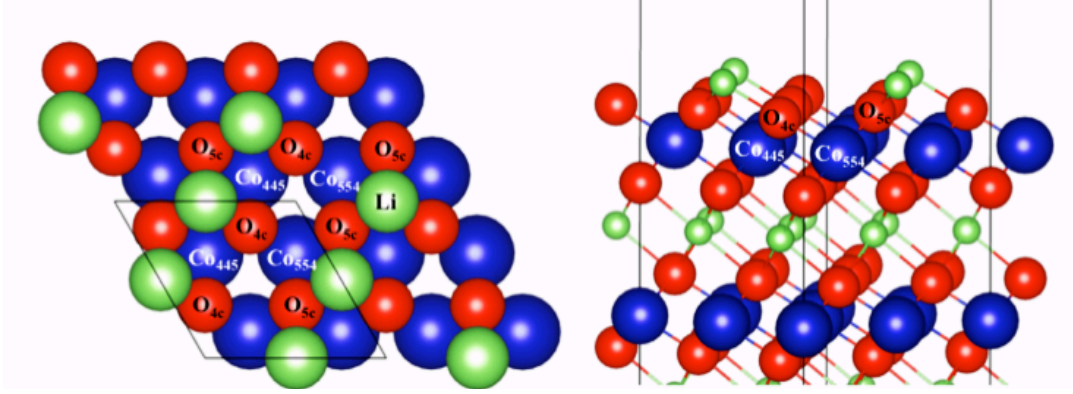


Figure 4.5 Left: The 1/2 ML Li-terminated layered LiCoO₂ (L-LCO) 2×2 slab structure consists of two equivalent Li atoms, connected with three O atoms, on each surface. Two types of O atoms and two types of Co atoms are in the second and third atomic layers, respectively: four-fold coordinated O (O_{4c}), five-fold coordinated O (O_{5c}); Co adjacent to two O_{4c} and one O_{5c} (Co₄₄₅), Co adjacent to two O_{5c} and one O_{4c} (Co₅₅₄). Right: The side view of the structure.

| Li-termination | Bond length (Å) | O-termination | Bond length (Å) | H-termination | Bond length (Å) |
|-------------------------------------|-----------------|-------------------------------------|-----------------|---------------------------------------|-----------------|
| Li – O _{4c} | 1.86 (1.86) | Co ³⁺ – O ₃₊ | 1.87 | H – O _H | 0.97 |
| Li – O _{5c} | 1.87 (1.86) | Co ³⁺ – O ₄₊ | 1.89 | Co _{1OH} – O _H | 1.95 |
| Co ₄₄₅ – O _{4c} | 1.92 (1.91) | Co ⁴⁺ – O ₃₊ | 1.81 | Co _{1OH} – O _{3c} | 1.89 |
| Co ₄₄₅ – O _{5c} | 1.95 (1.94) | Co ⁴⁺ – O ₄₊ | 1.86 | Co _{2OH} – O _H | 1.92 |
| Co ₅₅₄ – O _{4c} | 1.91 (1.90) | Co ³⁺ – O _{s3+} | 1.95 | Co _{2OH} – O _{3c} | 1.86 |
| Co ₅₅₄ – O _{5c} | 1.95 (1.94) | Co ³⁺ – O _{s4+} | 1.95 | Co _{1OH} – O _{s1OH} | 1.95 |
| | | Co ⁴⁺ – O _{s3+} | 1.94 | Co _{1OH} – O _{s2OH} | 1.91 |
| | | Co ⁴⁺ – O _{s4+} | 1.95 | Co _{2OH} – O _{s1OH} | 1.95 |
| | | | | Co _{2OH} – O _{s2OH} | 1.91 |

Table 4.3 Bonding distances of atoms denoted in Fig. 4, 6 and 8 for Li-terminated, O-terminated and H-terminated surface structures, respectively.

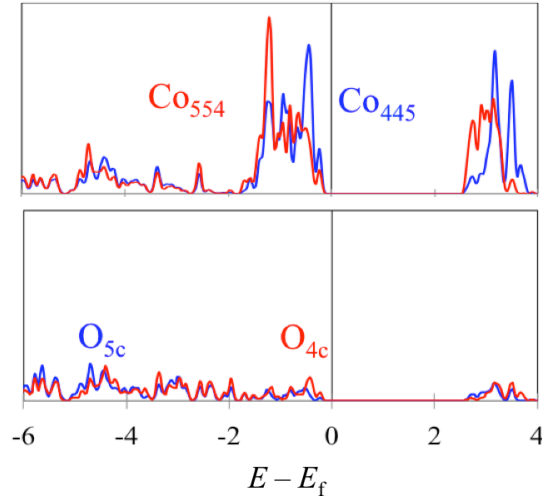


Figure 4.6 Electron density of states (DOS) projected onto surface Co and O, denoted in Fig 4, of the Li-terminated L-LCO (111) surface structure. The vertical line indicates the Fermi level position.

Figure 4.6 shows the DOS projected onto the aforementioned Co and O atoms of the L-LCO surface structure. Compared to the bulk structure, the upper valence band remains

mostly Co^{3+} $3d$ nonbonding states, indicating that the Li^+ ions on the surface sufficiently stabilize the undercoordinated O $2p$ electrons, leading to the predicted minor surface adjustment. Meanwhile, we note that Co_{445} (Co_{554}) $3d$ states are more pronounced at VB (CB) than Co_{554} (Co_{445}) $3d$ states, attributed to the relatively short Co – O_{4c} bond distances. This prediction demonstrates the positive correlation between the stability of subsurface Co – O bonds and the coordination number of surface O atoms.

4.3.4 Surface Li-deficiency

In a previous experimental study, the delithiation reaction near surface was observed during the oxygen evolution reaction (OER) resulting in the phase transformation of LiCoO_2 to the Co_3O_4 structure.⁷⁸ The event relates the instability of Li atoms near surface area to oxidizing environments, while also relating the sensitivity of surface structure to electrochemical operation. To better determine the active surface structure in catalytic OER, we examined the delithiated surface and possible stabilization reaction under aqueous conditions. We first calculated the removal energy of a Li atom on the surface. The averaged value is predicted to be about 1 eV lower than the bulk structure, indicating that the decreasing of coordination number compromises the stability of Li atoms. The result is in agreement with the occurrence of the delithiation reaction on surface structure under oxidizing environment or at high temperatures.⁹³

In addition to the redox deintercalation reaction, the Li^+/H^+ ion exchange on surface is also reported in recent experiments.^{94,95} In the experiment, a notable amount of OH groups is measured on the LiCoO_2 (001) surface under a high water exposure. Along

with a negatively charged water-solid interface being measured, a reaction involving the swapping of Li^+ ions on surface and protons of H_2O molecules was suggested. Differing from the removal of a Li atom, the Li^+/H^+ exchange reaction involves a minor reducing of the coordination number of O ions while maintaining the oxidation state of stable Co^{3+} . Coupled with the high solubility of Li^+ ions in water,⁹⁶ the corresponding H-terminated surface could form with no external bias required. We calculated the energy difference of replacing a Li ion on the surface with a proton from a water molecule by the equation of $\Delta E = [E_{\text{slab}}(\text{H-termi}) - E_{\text{slab}}(\text{Li-termi})] + [E(\text{LiOH}) - E(\text{H}_2\text{O})]$. The ΔE is predicted to be 1.7 and -0.3 eV in the vacuum and aqueous condition, respectively, implying that the switching reaction could be spontaneous in an aqueous solution or humid conditions. Atomic configurations and electronic structures of both O- and H-terminated surfaces were investigated. It is worth mentioning that the formation energy of a Li_2O (V_{Li2O}) vacancy on the Li-terminated surface and an O (V_{O}) vacancy on the O-terminated slab structures are also calculated as Co^{3+} ions undergo no redox reaction in the related defected structures. The $E_f(V_{\text{Li2O}})$ and $E_f(V_{\text{O}})$ were calculated to be 7.5 and 2.5 eV, respectively. The large $E_f(V_{\text{Li2O}})$ is qualitatively coherent with the the earlier experimental result showing that an extremely high temperature of around 1000 °C is required to induce the Li_2O depletion in LiCoO_2 structure.⁹⁷ That is, the direct Li_2O removal is unlikely to exist under ambient condition. On the other hand, the $E_f(V_{\text{O}})$ of the O-terminated surface is smaller than the rutile TiO_2 (110) surface (~ 3.7 eV) predicted in earlier theoretical works.^{98,99} Considering that oxygen defective TiO_2 surfaces have been widely observed in reducing environments,^{100,101} the relatively small $E_f(V_{\text{O}})$ implies

that the Vo could form on the O-terminated LiCoO₂ surface. The result is consistent with the previous experimental finding that partially delithiated Li_xCoO₂ matrices liberate O₂ molecules in high temperature environments.^{93,102,103} It is worth noting that the O-vacancy in metal oxides could be remedied by the dissociative water adsorption occurred at the interface, leading to the formation of H-termination.¹⁰⁴

4.3.5 O-terminated Surface Structure

We first study the redox Li-deintercalated surface structure [Fig. 4.7]. The selected bond lengths are summarized in Table 3. By removing two Li atoms from each surface, four Co³⁺ ions (two on each side) in the subsurface layer are oxidized to Co⁴⁺. In comparison to the Li-terminated case, the surface layer (O-layer) shifts inward by 0.04 Å in average, while the second atomic layer (Co-layer) shifts outward by 0.06 Å. The decreasing of the distance between the two layers is attributed to the absence of the attractive (repulsive) interaction of the Li⁺ cations and the O²⁻ anions (Co^{3+/4+} cations). Co³⁺ – O₃₊/O₄₊ are shortened by 0.03 – 0.05 Å with respect to the Li-terminated surface, as bond lengths being depend on the oxidation states of ions, Co⁴⁺ – O₃₊/O₄₊ bonds are further decreased by ~ 0.03 Å on average, as shown in Fig 6(b). On the third atomic layer (subsurface O-layer), O_{s3+} and O_{s4+} displace toward the forth atomic layer (subsurface Li-layer) with Co – O_{s3+}/O_{s4+} elongated by 0.02 Å and Li-O_{s3+}/O_{s4+} shortened by 0.01 – 0.03 Å, reflecting that the adjustment of O-terminated surface structure is slightly deeper into the bulk than the Li-terminated slab.

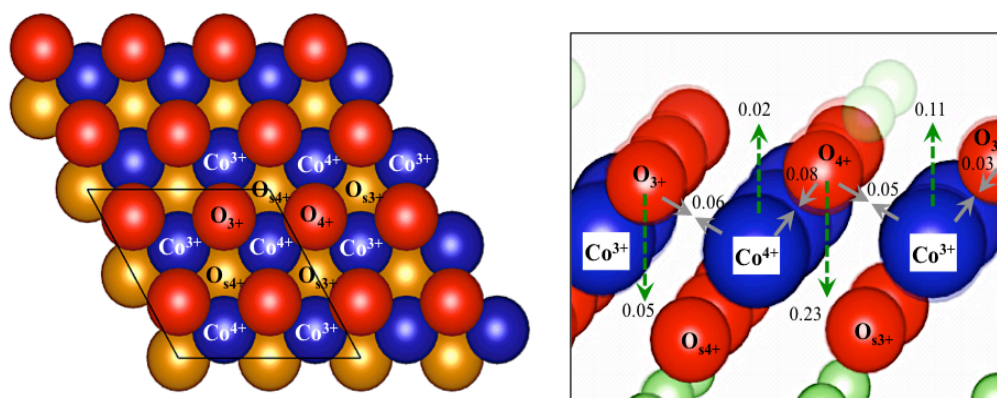


Figure 4.7 Left: 1/2 ML O-terminated layered LiCoO₂ (L-LCO) 2x2 slab structure consisted of two Co³⁺ and Co⁴⁺ ions in the subsurface layer. The first and third atomic layers both contain two types of O ions, and two ions for each type: surface/subsurface O adjacent to two Co³⁺ and one Co⁴⁺ (O₃₊/ O_{s3+}), surface/subsurface O adjacent to two Co⁴⁺ and one Co³⁺ (O₄₊/ O_{s4+}). Right: The side view of (a) marked with the displacements (Å) of atoms with respect to the Li-terminates surface structure.

Next, the Li^+ ion removed surface structure is simulated by adding four electrons to the aforementioned O-terminated slab structure; all Co^{4+} ions are reduced to Co^{3+} . The distance of $\text{Co}^{3+} - \text{O}$ bonds between the surface and subsurface layers are predicted to be 1.89 Å while between the subsurface and third atomic layers are 1.97 Å. Relative to the $\text{Co}^{4+} - \text{O}$ bonds in the Li-deintercalated case, $\text{Co}^{3+} - \text{O}$ bonds are elongated by about 0.03 Å in average, indicating the bonding strengths are weakened.

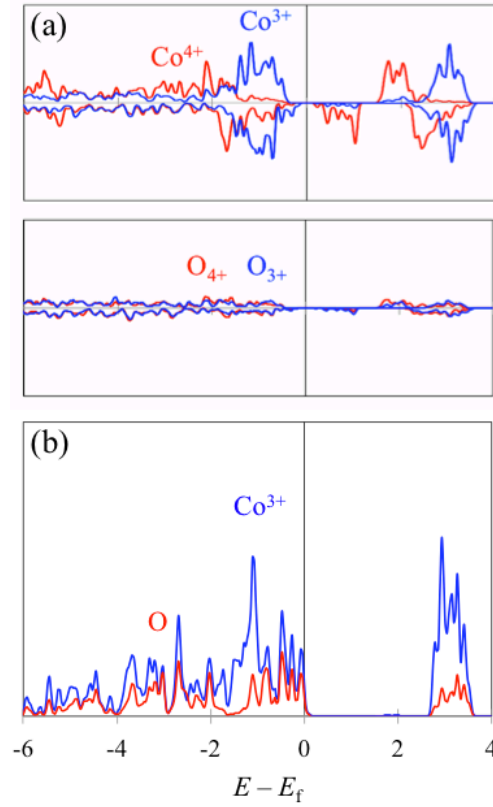


Figure 4.8 Electron density of states (DOS) projected onto Co and O denoted in Fig 6(a) of (a) Li-deintercalated and (b) Li^+ -removed O-terminated LiCoO_2 surface structure,. The vertical line indicates the Fermi level position.

Figure 4.8 (a) shows the DOS projected onto surface Co^{3+} , Co^{4+} ions and O atoms of the Li-deintercalated O-terminated surface structure. The VB and CB consist of Co^{3+} and Co^{4+} 3d states, respectively, as with the Li-deficient bulk structure. A small gap of ~ 0.3 eV is rendered, suggesting a reducible nature of Co^{4+} ions exist on the surface. A non-bonding feature of Co^{3+} 3d states is predicted right below Fermi level ($-0.5 \sim 0$ eV), indicating an enhancement of the antibonding interaction of the shortened $\text{Co}^{3+} - \text{O}_{3+}/\text{O}_{4+}$

bonds. Meanwhile, Co^{4+} $3d$ states are predicted at energy levels about 1 eV lower than Co^{3+} , due to the decreasing in total valence electron. The similar shape of O_{3+} and O_{4+} $2p$ states indicates the balance between the stronger ($\text{Co}^{3+} - \text{O}_{3+}/\text{O}_{4+}$) and weaker ($\text{Co}^{4+} - \text{O}_{3+}/\text{O}_{4+}$) antibonding states, which could be facilitated by the presence of Co^{4+} ions. In the Li^+ -removed case, the overlap of pronounced $3d$ and $2p$ states is predicted at VB [Fig. 4.8 (b)], suggesting the elongated Co – O bonds length result from the enhanced antibonding interaction. Compared to the Li-terminated case [Fig. 4.6], the pronounced O $2p$ states clearly demonstrate the reduced stability of the surface structure due to Li^+ ion removal.

4.3.6 H-terminated surface

On the H-terminated surface, H atoms attach to the O_{3c} atoms. Depending on the concentration of H atoms, the reduction of Co^{4+} to Co^{3+} and Co^{3+} to Co^{2+} occur in the subsurface layer via electron transfer from H atoms. The binding energy of H – O bonds on the 1/4, 1/2, 3/4 and 1 ML H-terminated surface are calculated to be -2.0 , -1.4 , -0.4 and -0.1 eV, respectively, with the to H_2 molecule as a reference. The relatively large energy drop between 1/2 and 3/4 ML cases suggests that the 1/2 ML H-terminated surface is more likely to be observed in ambient conditions. Nonetheless, a possible low-spin to high-spin transition of Co^{2+} ion is predicted in the 3/4 and 1 ML cases. Using DFT+U method, the high-spin configuration is predicted to be energetically more favorable than the low-spin configuration by ~ 0.7 eV. The same trend is predicted using hybrid functional calculation with a smaller energy difference of ~ 0.45 eV. This result

could be indirectly supported by the experimental observation of high-spin Co^{2+} ions in the spinel CoFe_2O_4 .¹⁰⁵ Adopting the energetically favorable spin state (high spin), the H – O binding energy of the third and forth H atoms become -1.1 and -0.8 eV, respectively, suggesting a hydrogenated surface structure contains possibly higher H-content. In this work, we are focused on the $1/2$ ML H-terminated surface with full Co^{3+} ions at the subsurface layer.

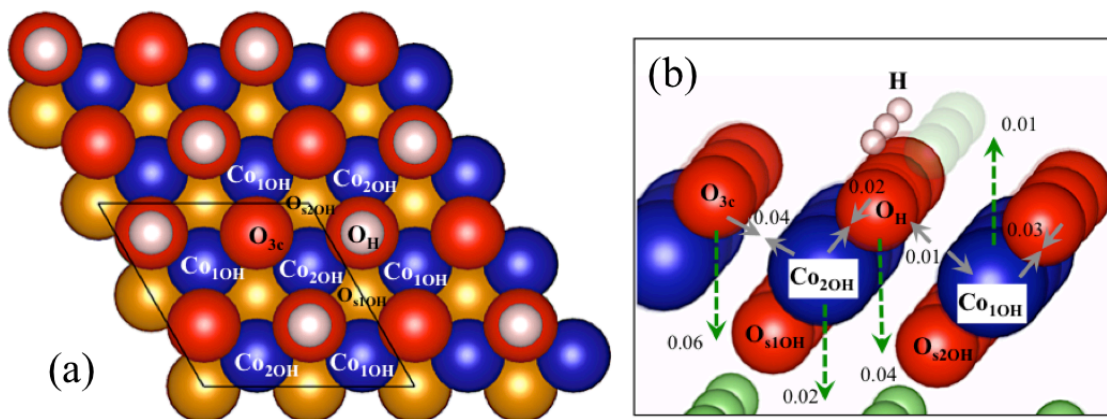


Figure 4.9 Left: 1/2 ML H-terminated 2x2 layered LiCoO₂ (L-LCO) slab structure consisted of two types of O ions on both first and third atomic layer; two types of Co ions on the second atomic layer in between: hydrogenated O (O_H), non-hydrogenated O (O_{3c}); Co adjacent to one O_H and two O_{3c} (Co_{10H}), Co adjacent to two O_H and one O_{3c} (Co_{20H}); subsurface O adjacent to two Co_{10H} and one Co_{20H} (O_{s1}), subsurface O adjacent to two Co_{20H} and one Co_{10H} (O_{s2}). Right: The side view of (a) marked with the displacements (Å) of atoms with respect to the O-terminated surface structure.

Figure 4.9 illustrates the atomic configuration of 1/2 ML H-terminated surface structure. The selected bond lengths are summarized in Table 3. The H – O bond distances are calculated to be 0.97 Å, as with alkali hydroxides reported in previous

experimental work.¹⁰⁶ The $\text{Co}_{1\text{OH}/2\text{OH}} - \text{O}_\text{H}$ distances are calculated to be almost the same as the bulk while being 0.06 Å longer than $\text{Co}_{1\text{OH}/2\text{OH}} - \text{O}_{3\text{c}}$, implying that the inward displacements of the undercoordinated O are restored by the hydrogenation reaction. Additionally, the distance of the Co and O_s layer is calculated to be similar to the bulk structure, supporting the restoration of structural stability. It is worth mentioning that the distance of $\text{Co}_{1\text{OH}}$ – and $\text{Co}_{2\text{OH}} - \text{O}_{\text{s}2}$ are predicted to be shorter than $\text{Co} - \text{O}_{\text{s}1}$ bonds by 0.04 Å, likely due to the linear connection of $\text{O}_\text{H} - \text{Co} - \text{O}_{\text{s}2}$ which helps lower the $\text{Co} - \text{O}_{\text{s}2}$ antibonding interaction.

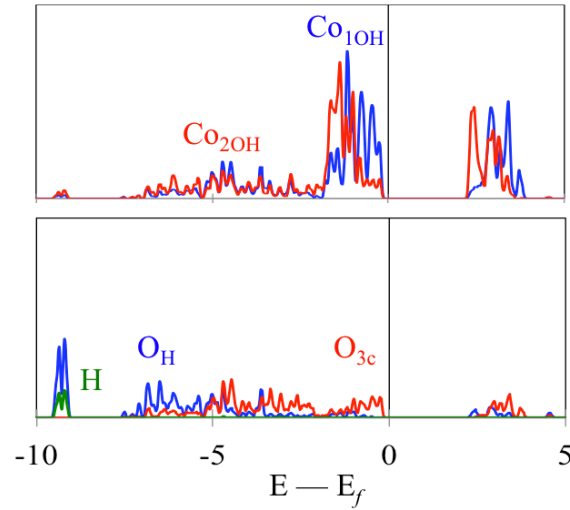


Figure 4.10 Electron density of states (DOS) projected onto H, Co and O, denoted in Fig 8 (a), of H-terminated LiCoO_2 surface structure. The vertical line indicates the Fermi level position.

Figure 4.10 shows the DOS of the H-terminated surface structure. The electronic structure is predicted to be similar to the Li-terminated surface structure composed of full

Co³⁺ ions coupled with the O 2*p* states which are stabilized via cations (H – O bonds); the hybridization of O_H 2*p* and H 1*s* states at around -9 eV implies the formation of an H – O bond. The Co_{2OH} 3*d* states are predicted to be mostly nonbonding states in the energy range from -2 to -1 eV, suggesting that the formation of the H – O bond lowers the Co – O_H antibonding interaction as the bond distance approaches that of the bulk. Meanwhile, Co_{1OH} 3*d* states are at a higher energy level than Co_{2OH} due to the connection with more undercoordinated O_{3c} ions. In comparison to the Li⁺-removed case, the significant downshift of O 2*p* states supports that the O-terminated surface could be stabilized through protonation reaction. Compared to the Li-intercalated case, the absence of the non-bonding feature of Co³⁺ 3*d* states at VB implies that the restoration of crystal structure Co³⁺ – O ions. It is worth noting that the reduction reaction of Co⁴⁺ ions to Co³⁺ is expected to enhance the related antibonding interaction; however, judging by the DOS analysis, the Co³⁺ – O bonds are stabilized by the adjacent protons well. The calculation illustrates that the hydrogenation reaction could effectively stabilize the delithiated surface.

4.4 SUMMARY

Using DFT-GGA calculations, we first examined the energetics, structures, and electric properties of both the layered (L-LCO) and spinel (S-LCO) LiCoO₂ structures. Based on the DOS analysis, the S-LCO structure is predicted to have stronger antibonding interactions of Co – O bonds than L-LCO, likely attributed to the more

compact Co_4O_4 cubane-like units. Relatedly, the L-LCO structure is thermodynamically more stable than S-LCO. Meanwhile, a small energy difference (0.01 eV/f.u.) is predicted for two phases, corresponding to the experimental observation that higher temperatures are needed for enhancing the kinetics of ion migration to synthesize the L-LCO structure. Next, the Li-deficient structure was modeled to investigate the influence of the presence of Li-vacancies on the LiCoO_2 structures. By creating a Li vacancy in the matrix, our calculations show that undercoordinated O atoms adjacent to the vacancy displace outward, shortening the $\text{Co}^{3+} - \text{O}$ bond distances and weakening the bond strengths. Meanwhile, a Co^{3+} ion is oxidized to Co^{4+} , mitigating the enhanced antibonding interactions of $\text{Co}^{4+} - \text{O}$ due to the Li removal.

According to the predicted surface energies of L- and S-LCO surface with different terminations, we found that the Li-terminated surface structure is more stable than the Co-terminated case for both phases. For the stoichiometric S-LCO (111) surface structure having 1/4 ML Co^{3+} ions on the surface, we predicted that the site switching of surface Co^{3+} and subsurface Li^+ ions lowers the surface energy by -0.37 J/m^2 . The stabilization suggests that the site switching could be an influential initiator for the spinel-layered phase transformation during the annealing process observed in previous experiments. Considering that, the Li-terminated L-LCO (111) structure is employed for more comprehensive surface studies. Excepting the decreasing of Li – O bond by about 0.25 Å, only minor structural adjustments are predicted for the Li-terminated surface structure, implying that surface Li^+ ions stabilize the underneath Co – O bonds effectively. On the other hand, as there are both 4- and 5-fold O atoms in the subsurface

layer, the DOS analysis illustrates that Co^{3+} $3d$ states are predicted to be more pronounced for the Co^{3+} adjacent to more 4-fold O atoms, indicating a negative correlation between surface stability and the coordination loss of O atoms.

Following that, two types of O-terminated surface structure created by removing 1) Li atoms (50% of Co^{3+} ions reduced to Co^{4+} in the subsurface layer) and 2) Li^+ ions (all Co^{3+} ions remained) are studied. For the Li-removal case, the subsurface $\text{Co}^{3+} - \text{O}$ bonds are shortened by $0.03 - 0.05 \text{ \AA}$ compared to the Li-terminated surface. Meanwhile, $\text{Co}^{4+} - \text{O}$ bond lengths are shorter than $\text{Co}^{3+} - \text{O}$ by another 0.03 \AA ; the above trends are similar to the Li-deficient bulk structure. On top of that, the DOS analysis illustrates a similar energy density distribution of O $2p$ states from O adjacent to different number of Co^{3+} and Co^{4+} ions, suggesting a balance between antibonding interactions of $\text{Co}^{3+} - \text{O}$ and $\text{Co}^{4+} - \text{O}$ bonds on the surface. For the Li^+ -removal case, $\text{Co}^{3+} - \text{O}$ bond distances are predicted to be similar to the Li-removal case. Relatedly, the DOS analysis also illustrates significant overlap of $3d$ and $2p$ states at the VB. As the subsurface layer contains more Co^{3+} ions, the stability of the surface structure is further compromised.

On the H-terminated surface structure, protons bond with the 3-fold coordinated O atoms. According to our calculations, the $\text{Co}^{3+} - \text{O}$ bond lengths in the subsurface layer are predicted to be similar to the Li-terminated case, implying the protons function effectively to stabilize the Co – O bonds. Compared to the Li-removal case, the DOS analysis illustrates that the total Co^{3+} $3d$ states become more pronounced as Co^{4+} ions are reduced to Co^{3+} . At the same time, the original Co^{3+} $3d$ states are stabilized as the adjacent O $2p$ states are stabilized through forming bonds with protons. Compared to the

Li⁺-removal case, the aforementioned stabilization of Co³⁺ 3*d* states are even more significant than the Li-removal case when coupled with O 2*p* states.

Last but not the least, the formation energy of 1/4 ML O-deficiency on O-terminated and Li₂O-deficiency on Li-terminated surface structures were calculated to be about 2.5 and 7.5 eV, respectively, suggesting that the O-deficient surface structure could be formed in a reducing environment, while the Li₂O-deficient case might be difficult. Nonetheless, the O-deficiency could be eliminated through water adsorption reaction in solution, leading to the formation of an H-terminated surface.

These fundamental findings add to the understanding of the properties of surface structure of LiCoO₂, especially in aqueous conditions. While various terminations are investigated, the importance of cations (Li⁺ and H⁺) on the surface with regards to the stability of surface structure is particularly demonstrated. On top of that, the formation of H-terminated surface structures in aqueous solution through either Li-deintercalation/hydrogenation or Li⁺/H⁺ ion exchange reactions are discussed. Following that, our studies of oxygen evolution reaction (OER) facilitated by the hydrogenation reaction are introduced in Chapter 5.

Chapter 5 : Reaction Mechanisms for the Oxygen Evolution Reaction on LiCoO₂ (001) Surface

5.1 INTRODUCTION

The oxygen evolution reaction (OER) is an important electrochemical energy technology for photoelectrochemical water splitting and Li-air batteries. Precious metal-based electrocatalysts such as Pt, RuO₂ and IrO₂ are considered typical electrode materials due to their high performances;^{107,108,109,110} however, the commercialization has long been hindered by the scarcity of raw materials. To search for substitutes, metal-oxides are studied intensively due to their low-cost and high stability. More importantly, the diverse valence states of metal cations in the matrices could facilitate charge transfer conducted in the catalytic reaction.¹¹¹ Among various metal-oxides, LiCoO₂ receives special attention regarding to that its tunable Li-content which observed to benefit the catalytic performance.⁷⁶ In addition, LiCoO₂ performance as an OER/ORR bifunctional catalyst after surface structure transformation is reported in earlier experiment work.⁷⁴ To further improve the performance of materials, a comprehensive understanding reaction mechanisms is necessary. On various metal and oxides surface structures, the OER is widely described by the well known four-electron pathway along with the water adsorption reaction on metal ions;^{112,113,114} nonetheless, the discussions about non-metal terminated surface structure are limited. As the OER for Co-based hydroxides has been reported in some recent studies, the existence of non-metal catalytic surface could also be suggested.^{115,116} In this chapter, we attempt to propose the possible mechanisms of the

catalytic OER for surfaces absent of metal elements. The H-terminated LiCoO_2 (001) surface structure, as discussed in Chapter 4, is employed for the investigation. (The atomic configurations of Li-, O-, and H-terminated surface structures are introduced in detail in Chapter 4) Therefore, the active surface structure is composed of only protons and O atoms. Starting with the oxidation-induced deprotonation reaction on surface, we investigated the catalyzing reactions driven by the subsurface $\text{Co}^{3+/4+}$ redox reaction combined with the re-protonation reaction. Without being limited to the LiCoO_2 structure, we hope this work could provide new perspective towards explaining the OER on metal oxides in general.

5.2 METHODOLOGY

All atomic structures and energies reported herein were calculated using spin-polarized DFT within the generalized gradient approximation (GGA-PBE)^{15,16} as implemented in the Vienna Ab initio Simulation Package (VASP)^{32,33}. The projected augmented wave (PAW) method^{34,35} with a plane-wave basis set was employed to describe the interaction between ion core and valence electrons. To treat the strong on-site $3d$ electron-electron interactions on Co an additional Hubbard-U was added (with an effective value of $U_{\text{eff}} = 4.91$ eV for Co atoms in the structure).⁸³ Valence configurations employed are as follows: $1s^2 2s^1$ for Li, $3d^7 4s^2$ for Co, and $2s^2 2p^4$ for O. An energy cutoff of 450 eV was applied for the plane-wave expansion of the electronic eigenfunctions. For geometry optimization and energy calculations, all atoms were fully relaxed using the

conjugate gradient method until residual forces on constituent atoms became smaller than 1×10^{-2} eV/Å. The surface structure was modeled using a periodic (4×4) slab with a thickness of 4 oxygen-layers and a vacuum of 15 Å in the (111) direction. For Brillouin zone sampling, (3×3×1) k-point mesh in the scheme of Monkhorst-Pack³⁸ was used for the slab structures. The H-bond network on the solid/liquid interface was modeled using the ab-initio molecular dynamics simulation (AIMD). A total of 1.93 nm of liquid water was included, enough to approximate the ambient density of liquid water at the point furthest from the two surfaces. The implicit solvent model¹¹⁷ was employed for the prediction of binding energies of intermediate products on the surface structure. A smaller (2×2) surface structure connected to a four-water H-binding network was used to model the oxidation-induced deprotonation reaction.

5.3 RESULTS AND DISCUSSION

5.3.1 H-terminated Surface in Aqueous Solution

We employed the H-terminated surface structure to study the oxygen evolution reaction (OER) structure for the layered LiCoO₂ (001) surface. Considering the experiments are practiced in aqueous conditions, we first simulated the interaction of water and the surface structure at the solid/liquid interface. The ab-initio molecular dynamics simulation (AIMD) predicts constant rearrangements of hydrogen atoms on the surface through water network at 300 K, suggesting that the stability of surface structures are similar among various H-coverage configurations in the water solution. As shown in

Fig. 5.1 (a), at the interface, H_2O molecules behave as either H-bond donors ($\text{HO} - \text{H} \cdots \text{O}_{3c}$) or acceptors ($\text{H}_2\text{O} \cdots \text{H} - \text{O}_{3c}$) by forming H-bond with the either 3-fold undercoordinated O atoms (O_{3c}) or protons, respectively. The averaged H-bond distances between water and surface O_{3c} atoms are predicted to be about 1.5 Å, slightly shorter than the average distance of intermolecular hydrogen bonds by 0.2 Å. At the same time, H atoms on the surface are slightly pulled away by the water molecules by about 0.05 Å compared to the case in vacuum.

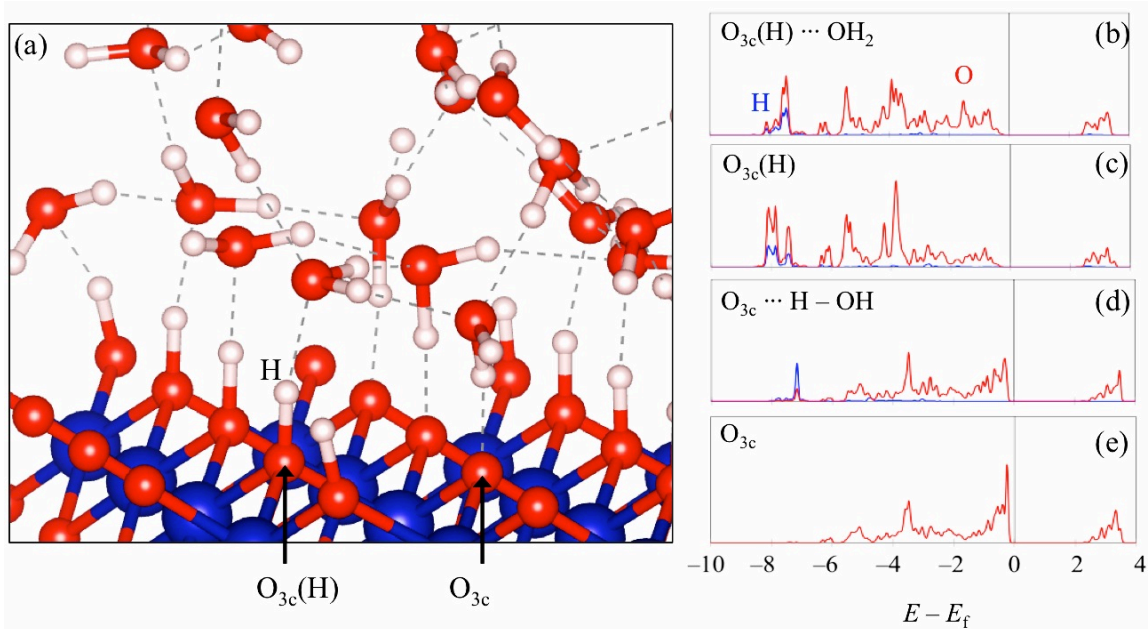


Figure 5.1 (a) Structure of the solid/liquid interface of H-terminated LiCoO_2 (111) surface structure in the explicit solvent model. (b)-(e) Electron density of states (DOS) projected onto the undercoordinated (O_{3c}) and hydrogenated ($\text{O}_{3c}(\text{H})$) O_{3c} atoms. The vertical line indicates the Fermi level position.

Figure 5.1 (b) – (e) show the electron density of states (DOS) projected onto H and O atoms on the H-terminated surface structure in the water solution. First, we

compared the surface H – O_{3c} bond with the H interacting [Fig. 5.1 (b)] and not interacting [Fig. 5.31 (c)] with the H₂O molecule from the solution. Clearly, when H interacts with a water molecule, both the H 1s and O 2p states shift upward in terms of energy, suggesting the stability of a slightly elongated H – O bond is reduced. On the other hand, the DOS illustrates that the non-hydrogenated O_{3c} 2p states shift downward while interacting with a water molecule [Fig. 5.1 (d) and (e)], implying the H-bond interaction stabilizes the O_{3c}. It is worth mentioning that a small overlap of O_{3c} 2p and H 1s states (of donors) suggests marginal atomic orbital interactions between the lattice oxygen atom and water molecule [Fig. 5.1 (d)]. These findings indicate that water molecules could stabilize the O_{3c} atoms as H-donors along with assisting proton rearrangement on the surface. The resulting high mobility of proton could accelerate the proton coupled electron transfer (PCET)¹¹⁸, which in turn facilitates the catalytic reactions at the solid-liquid interface.

5.3.2 Oxidized Surface Structure

To investigate the OER for the LiCoO₂ structure, the effect of hole injection on the H-terminated slab structures was studied. As illustrated in Fig. 5.2, we used four water molecules to simulate the local water networks on the 1/2 and 1/4 ML H-terminated 2×2 slab structures. The intermolecular hydrogen bonds between four water molecules range from 1.60 to 1.84 Å, sufficiently capturing a water network. In the neutral state, a proton on the 1/2 ML H-terminated surface forms a hydrogen bond with

an oxygen ion of a water molecule at the interface; the $\text{HOH}\cdots\text{O}_{3c}$ distance is predicted to be 1.81 Å [Fig. 5.2 (a)]. After removing an electron from the slab structure, a proton is predicted to detach from an O atom and move to the water network [Fig. 5.2 (b)]; a hydronium ion (H_3O^+) with H – O bond lengths of 1.01, 1.03 and 1.12 Å is formed in the water solution.

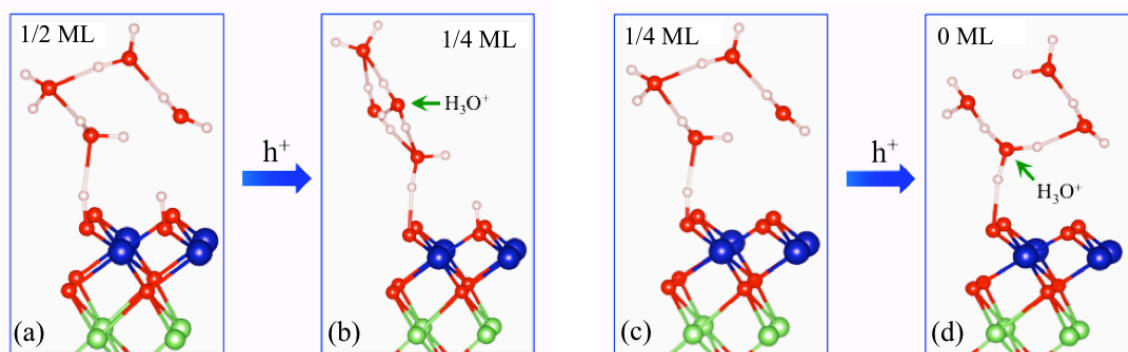


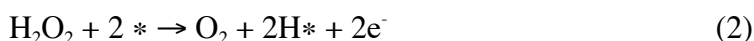
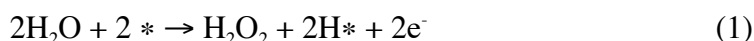
Figure 5.2 Structures of H-terminated surface connected to H-bond networks (4 water molecules) in the neutral (a,c) and positively charged (b,d) states.

At the meantime, a Co^{3+} ion adjacent to the newly formed O_{3c} atom is oxidized to Co^{4+} as the Co – O bond distance is reduced by about 0.03 – 0.04 Å. Compared to the case with protons fixed on the surface, the creation of an H_3O^+ ion lowers the total energy by 1.22 eV, indicating the deprotonation reaction is spontaneous in the positively charged system. The same deprotonation reaction is also predicted on the positively charged 1/4 ML H-terminated surface [Fig. 5.2 (c) and (d)], implying the independence of the reaction on the proton concentration. At this point, our calculations have revealed the possibility of creating H-removals and corresponding O_{3c} sites on the H-terminated surface structure. In

Chapter 4, we have discussed the stabilization of O-terminated LiCoO₂ surface structure achieved by the hydrogenation reaction in water solutions. Accordingly, the potential mechanisms of OER driven by the hydrogenation reaction of the surface structure are investigated.

5.3.3 Reaction Pathway for OER

The four-electron pathway of the OER catalyzed by LiCoO₂ (111) H-terminated surface is proposed as follow:



, where * denotes a surface O_{3c} site created by removing H atoms and X* indicates an adsorbed X species.

In this scheme, each reaction step happens along with two proton/electron transfers from solution to O_{3c}/Co atoms on the surface/subsurface layer. That is, the recovery of valence state of Co^{3+/4+} (4+ → 3+) ions and the stabilization of adjacent Co³⁺ – O bonds are proposed to be the main driving forces of the mechanisms. In step 1, a hydrogen atom from water interacts with an O_{3c} atom (HOH...O_{3c}), resulting in the creation of hydroxyl radical (OH). The OH could first adsorb on another O_{3c} atom (water dissociative adsorption), and then react with another H₂O molecule, or directly react with another H₂O molecule to form a H₂O₂ molecule (as another H atom bounds to the surface

O_{3c}). In a previous experimental study, the observation of H₂O₂ molecules as intermediate products in the OER (four-electron pathway) has also been reported for the oxyhydroxide iron electrode by Lyons et al.¹¹⁹ In step 2, H₂O₂ is oxidized to O₂, as both H atoms transfer to the surface O_{3c} atoms. Relatedly, in a recent experiment, Takashima et al. reported the oxidation reaction of H₂O₂ to O₂ through a chemisorption reaction at the solid/liquid interface of metal oxides.¹²⁰

5.3.4 Dependence of H and OH Binding Energy on H-removal Concentration

Known to be the major indicator of reaction activities, the predicted hydrogen binding energies on H-terminated surface structures with various concentrations and distributions of H-removals are summarized in Table 5.1 (with respect to half of an H₂ molecule). For the purpose of clarity, the removal energy is defined as the negative value of the corresponding binding energy from hereafter.

| | 1H-removal | 2H-removal | 3H-removal | 4H-removal |
|--|------------|---------------------------------|------------|------------|
| $E_b(\text{H})$ with respect to H ₂ | -1.43 | -1.65 [-1.47] _{sep} | -2.08 | -2.11 |
| Dissociative adsorption of H ₂ O | 3.03 | 0.45 [0.96] _{sep} | -0.22 | -0.38 |

Table 5.1 Predicted hydrogen binding and water dissociative adsorption energies on the H-terminated surface structure with various amounts of clustered H-removals. The energies for separated H-removal cases are in the square brackets.

Starting with the 0.5 ML H-terminated surface structure, the removal energy of the first H atom is predicted to be 1.43 eV, which is similar to removing another (second) H atom when two H-removals are separated from one another. The similarity suggests the creation of an H-removal does not have a long-range effect on the structure. In addition, the removal energies could remain alike as the H-coverage rate remains higher than 0.25 ML (corresponding to 50% H removed). On the other hand, for the clustered H-removal case, the energy of removing the second H atom is predicted to be 1.65 eV, higher than the separated case by 0.18 eV. To explain what causes the difference, we need to look into the stability of Co^{3+} ions in the subsurface layer. During the dehydrogenation reaction, after O_{3c} is created, two types of Co^{3+} ion are created in the subsurface layer: (1) $\text{Co}_{\text{OH}}^{3+}$ ion adjacent to two O_{3c} and an O_{H} atom and (2) $\text{Co}_{\text{O}_{3c}}^{3+}$ ion adjacent to three O_{3c} atoms on the surface. The removal energy is highly dependent on the type of Co^{3+} ions adjacent to the resulting O_{3c} atom. For the first H-removal, O_{3c} atom is adjacent to two $\text{Co}_{\text{OH}}^{3+}$ and a Co^{4+} ion. As $\text{Co}_{\text{OH}}^{3+}$ is more stable than $\text{Co}_{\text{O}_{3c}}^{3+}$, the removal energy is the lowest. For the separated 2H-removal case, the types of adjacent Co^{3+} ions of both O_{3c} atoms are the same. Thus, the removal energies are similar to each other. On the other hand, in the clustered 2H-removal case, the created O_{3c} atom is adjacent to $\text{Co}_{\text{OH}}^{3+}$, $\text{Co}_{\text{O}_{3c}}^{3+}$ and Co^{4+} ions; the presence of $\text{Co}_{\text{O}_{3c}}^{3+}$ results in the higher removal energy. Following the same rational, for the third H-removal, the created O_{3c} atom is adjacent to two $\text{Co}_{\text{OH}}^{3+}$ and a Co^{4+} ion, resulting in the highest H removal energy (2.08 eV). The removal energies of the forth H atom is predicted to be 2.11 eV, almost the same as the third H removal, due

to the process also creating another $\text{Co}_{\text{O}_{3\text{c}}}^{3+}$. Based on that, for the clustered case with three H-removals and beyond, the removal energies could be similar.

Figure 5.3 shows the DOS projected onto $\text{O}_{3\text{c}}$ atom of the surface containing H-removals. Depending on the amount of H-removals, the $2p$ states of $\text{O}_{3\text{c}}$ adjacent to (1) two $\text{Co}_{\text{OH}}^{3+}$ and a Co^{4+} ion, (2) $\text{Co}_{\text{OH}}^{3+}$, $\text{Co}_{\text{O}_{3\text{c}}}^{3+}$ and Co^{4+} ion, and (3) two $\text{Co}_{\text{OH}}^{3+}$ and a Co^{4+} ion are illustrated. A continuous upshift of positions of the VB corresponds to the positive correlation between the H-removal energy and the dehydrogenation level.

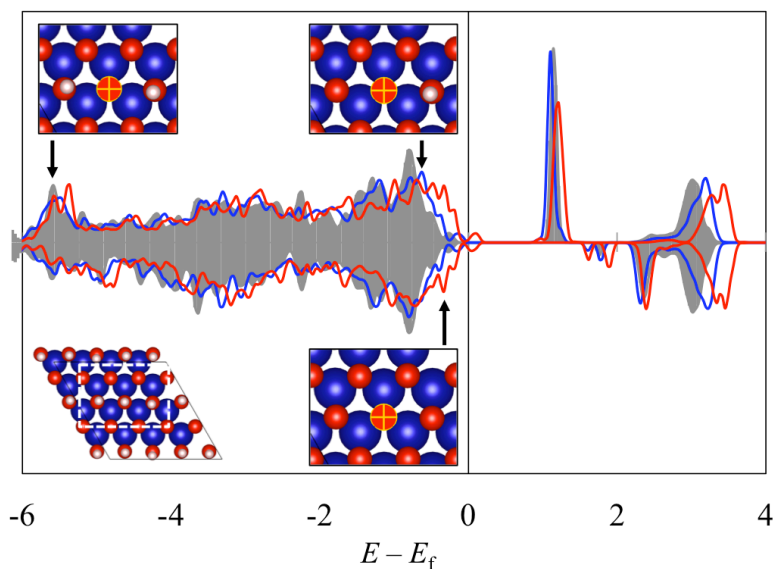


Figure 5.3 Electron density of states (DOS) projected onto the 3-fold undercoordinated O atoms (yellow cross) on the surface structure of clustered 1H-removal (grey shaded), 2H-removal (blue), and 3H-removal (red) cases. The vertical line indicates the Fermi level position of the 1H-removal case. Insets are the zoom-in images indicated by white dotted line.

According to our calculations, for a proton to transfer from an H₂O molecule to O_{3c} on the surface, an electron is required to transfer to a Co⁴⁺ ion in the subsurface layer at the same time. That is also the concept of PECT. As the H-terminated surface structure has no metal cation exposed to the solution, H₂O molecules mostly interact with the surface structure via H-bonds at the solid/liquid interface. In pervious studies, charge transfer through H-bond has been reported in organometallic complexes;^{121,122} though, with small magnitudes. On top of that, in another study about the charge redistribution of the water dimer, Bartha et al. pointed out that the valence electrons of an H-bond donor shift in the opposite direction of the H-bond acceptor.¹²³ This tendency of charge distribution could lower the probability of the PCET via H-bond directly. Nevertheless, while the charge transfer via H-bond is jeopardized, the increase of electron density near the O side of water may enhance the interaction between the H – O bond of water and the O_{3c}, i.e. [H₂O...O_{3c}], leading to the dissociative water adsorption with a related proton and OH⁻ adsorbed on separated O_{3c} atoms. In fact, in a previous study Grimaud et al. also reported the OER involves the adsorption of OH⁻ ions onto lattice O atoms of the Co-based perovskite oxides.¹²⁴

Table 5.1 also summarizes the dissociative water adsorption energy based on the related H⁺ and OH⁻ ions being adsorbed on the O_{3c} atoms. The energies are predicted to be 3.03, 0.45, -0.22 eV, and -0.38 eV based on the O_{3c} created for 1, 2, 3, and 4 clustered H-removal cases, respectively. The continuously decreasing energy indicates the stronger tendency for water dissociation on the surface. Considering the larger increments of the H₂O dissociation energy compared to the H-removal energy for each additional H-

removal, the adsorption energy of OH^- anion is predicted to increase along the way. As shown in Fig. 5.4 (a), the $\text{HO} - \text{O}_{3c}$ bond distance is predicted to be 1.46 Å, implying the peroxy nature of the $\text{O} - \text{O}$ bond. The lengths of three $\text{Co} - \text{O}$ bonds adjacent to the $\text{O} - \text{OH}$ are predicted to be 1.92, 1.92, and 1.94 Å, similar to the H-terminated case (1.92, 1.92, 1.94 Å) [Fig. 5.5 (b)], indicating that the OH stabilizes the $\text{Co} - \text{O}$ bonds as protons do. Figure 5.5 shows the DOS projected onto the Co and O atoms adjacent to the removal site of the clustered 3H-removal surface before (a) and after (b) the OH adsorption. In Fig. 5.5 (a), the top of the valence band (VB) and bottom of the conduction band (CB) consist of Co^{3+} and Co^{4+} 3d states, respectively.

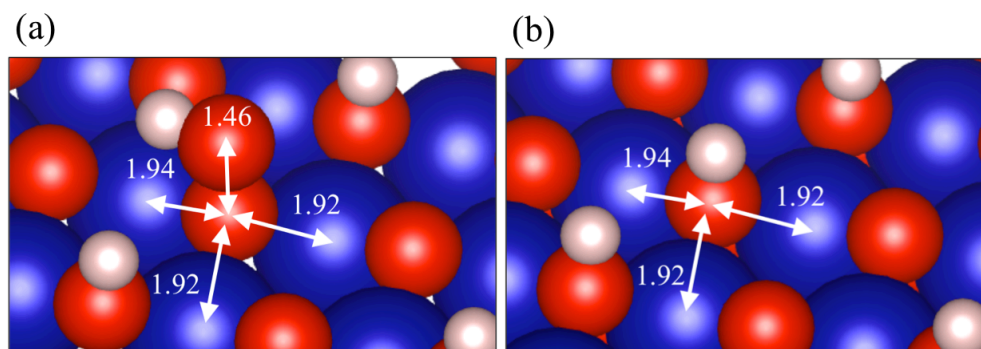


Figure 5.4 Structures of the adsorption configuration of *OH (a) and *H (b) on H-terminated surfaces.

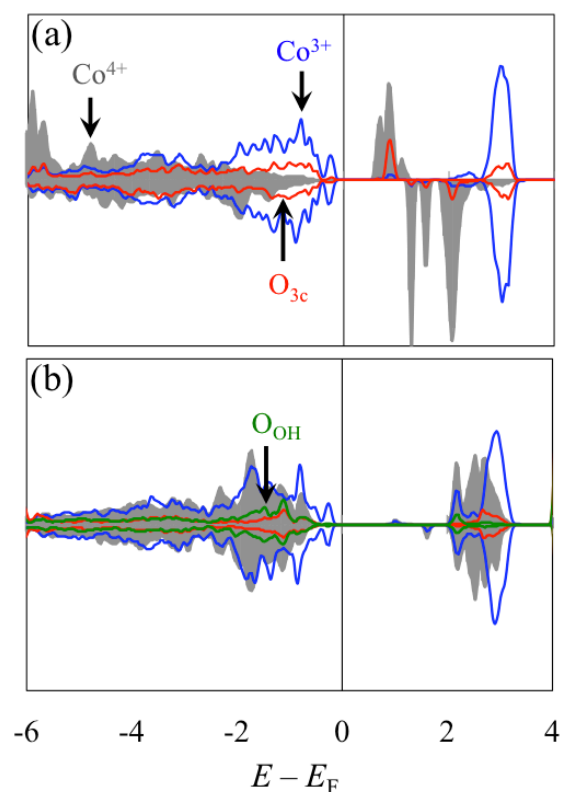


Figure 5.5 Electron density of states (DOS) projected onto Co and O atoms adjacent to the H-removal site on the surface structure before (a) and after (b) $^*\text{OH}$ adsorption on the 3-fold undercoordinated O (O_{3c}) atom. The vertical line indicates the Fermi level position of the 1H-removal case.

The pronounced nonbonding Co^{3+} $3d$ states below the Fermi level are attributed to the strong antibonding interaction with the adjacent O_{3c} $2p$ states, as with the aforementioned $\text{Co}_{\text{O}_{3c}}^{3+} - \text{O}_{3c}$ bond. In Fig. 5.5 (b), with OH adsorbed on the O_{3c} site, the VB is predicted to be Co^{3+} $3d$ states, implying the reduction reaction of Co^{4+} to Co^{3+} ions. Relatedly, the downshift of O_{3c} $2p$ states corresponds to the p -electron redistribution which result from

the peroxy nature of the O – OH bond. Following that, the stabilization of Co³⁺ 3d states at the upper valence band is also predicted.

| H-terminated LiCoO ₂ | 1 H-removal | 2 H-removal | 3 H-removal |
|---|-------------|-------------|-------------|
| $2 \text{H}_2\text{O} + 2 * \rightarrow \text{H}_2\text{O}_2 + 2 \text{H}^* + 2 \text{e}^-$ | 1.08 | 0.48 | -0.38 |
| $\text{H}_2\text{O}_2 + 2 * \rightarrow \text{O}_2 + 2 \text{H}^* + 2 \text{e}^-$ | -0.77 | -1.37 | -2.23 |

Table 5.2 Predicted enthalpies of reactions for the proposed OER pathway. The calculations are based on the binding energy of *H on surface with various amounts of clustered H-removals.

5.3.5 Reaction Enthalpies

Table 5.2 summarizes enthalpies of reaction for OER on the H-terminated LiCoO₂ (111) surface structure with various amounts of H-removals (*). Each enthalpy is calculated by considering an *H to be adsorbed on the specified type of H-removal defined in the Section 5.3.4. For step 1 ($2\text{H}_2\text{O} + 2 * \rightarrow \text{H}_2\text{O}_2 + 2\text{H}^* + 2\text{e}^-$), the enthalpies are predicted to be 1.08, 0.48, and -0.38 eV for the clustered 1H-, 2H-, and 3H-removal cases, respectively. As the binding energy of *H atoms increases (in the negative direction) along with the creation of H-removal, the reaction becomes more favorable. The reaction is predicted to be exothermic for the 3H-removal case, implying two O_{3c} sites both adjacent to two CoO_{3c}³⁺ ions are needed to trigger the oxidation reaction. As shown in Table 5.1, forming the coupled 3H-removal is predicted to be energetically less favorable than the separated case by 0.65 eV using implicit solvent model; however, as

discussed in Section 5.3.1, the rearrangement of *H on the surface in the water solution is predicted using AIMD under ambient conditions. Therefore, the clustered 2H- or 3H-removals are still expected on the oxidized surface structure, especially in the presence of high H-removal contents. For step 2 ($\text{H}_2\text{O}_2 + 2 * \rightarrow \text{O}_2 + 2\text{H}^* + 2\text{e}^-$), the enthalpies are predicted to be -0.77 , -1.37 , and -2.23 eV for the clustered 1H-, 2H-, and 3H-removal cases, respectively, implying that H_2O_2 could be oxidized to O_2 by the surface with even low concentrations of H-removal. Based on that, step 1 is suggested to be the rate-limiting step for the OER. Overall, the smallest enthalpy (in absolute value) for the full reaction of catalytic OER ($2 \text{H}_2\text{O} + 4* \rightarrow \text{O}_2 + 4 \text{H}^* + 4 \text{e}^-$) on H-terminated LiCoO_2 surface is predicted to be -1.15 eV.

5.4 SUMMARY

Using DFT-GGA calculations, we introduced a four-electron pathway for OER catalyzed by the H-terminated LiCoO_2 (001) surface structure. First of all, our calculations predict that protons detach from the surface structure into the solution when the subsurface Co^{3+} ions are oxidized to Co^{4+} ions. That is, injecting holes to the slab structure leads to the creation of additional 3-fold undercoordinated O atom (O_{3c}) on the surface. Next, a two-step reaction pathway driven by the hydrogenation of the surface is proposed. In the first step, H_2O molecules undergo the dissociative water adsorptions onto surface O_{3c} atoms. The related *OH then further interacts with another H_2O molecule to form an H_2O_2 molecule. To predict the reaction enthalpies, the binding

energy of H atoms and the dissociative adsorption energy of H_2O molecules are calculated for the surfaces with various amounts of H-removals. Accordingly, the dissociative adsorption is predicted when there are two sets of clustered 3H-removals on the surface. On top of that, the reaction of H_2O transforming to H_2O_2 (as H atoms are transfers to the surface) is predicted to be exothermic in the presence of the same type of H-removals. In step 2, the exothermic reaction of H_2O_2 being oxidized to O_2 by the surface containing a low concentration of H-removal is predicted, indicating that the H_2O_2 could be a strong reducing agent on the oxidized H-terminated surface. On top of that, the formation of H_2O_2 is suggested to be the rate-limiting step of this proposed pathway.

Chapter 6 : Mechanisms for the Oxygen Reduction Reaction on Co_3O_4 (111) Surface

6.1 INTRODUCTION

The oxygen reduction reaction (ORR) is a crucial electrochemical process in fuel cells. Its efficiency and reaction pathway have been widely studied; they are reported to be highly dependent on the electrode materials. Precious-metal electrodes (PMD) (eg. Pt, Ir and Ru) are the best catalyst known so far;^{125,126,127} however, the application of PMD is hindered by their high-cost and limited stability. Among the non-precious-metal-based catalysts, Co_3O_4 structures are reported to be one of the most promising materials for ORR.^{75,128} The performance of Co_3O_4 is found to be highly dependent on the incorporated system. While the pristine Co_3O_4 structure is reported to catalyze the ORR through the two-electron pathway, the presence of a carbon-based support was found to change the related reaction pathway to the more active four-electron pathway.¹²⁹ On top of that, carbon-supported Co_3O_4 structure could also perform as OER/ORR bifunctional catalysts. In addition to carbon, transition metal dopants such as Mn and Cu are also reported to improve the catalytic performances.^{130,131,132} To fully understand how carbon-based structure and dopants facilitate the electrochemical ORR, it is necessary to identify the active sites and their possible mechanisms for the catalytic reaction. Nonetheless, the determination of active sites for ORR on the carbon-supported Co_3O_4 structure has been a longstanding question still under debate. In earlier experimental works, Xu et al. reported that the ORR catalytic activity is sensitive to the content of exposed Co^{3+} ions on the

surface,¹³³ while Xiao et al. described the Co^{2+} ions as the active sites for ORR.¹³⁴ In a recent experimental work, Liu et al. suggested the N-doped carbon nano-web in the composite structure should be the primary catalyst for ORR to take four-electron pathway.

In this chapter, we first looked into the properties of bulk structure to understand the nature of Co – O bonds in the matrix. In doing so, we noticed the predicted electronic structures are sensitive to the U-value employed in the DFT calculation; the dependence of spin states of Co^{3+} on U-values is thus examined. For the surface study an O-terminated surface structure is assumed considering the high surface energy caused by the presence of undercoordinated metal atoms on surface. In addition, based on the discussion of hydrogenated LiCoO_2 surface structure in Chapter 4, the hydrogenated Co_3O_4 surface structure is also employed. The reaction steps of the four-electron pathway for ORR on the (111) surface structure composed of H and O atoms are investigated. Lastly, the possible two-electron pathway is also discussed.

6.2 METHODOLOGY

All atomic structures and energies reported herein were calculated using spin-polarized DFT within the generalized gradient approximation (GGA-PBE)^{15,16} as implemented in the Vienna Ab initio Simulation Package (VASP)^{32,33}. The projected augmented wave (PAW) method^{34,35} with a plane-wave basis set was employed to describe the interaction between ion core and valence electrons. To treat the strong on-

site 3d electron-electron interactions on Co an additional Hubbard-U was added with an effective value of $U_{\text{eff}} = 4.4$ and 6.7 eV for the tetrahedral and octahedral Co atoms in bulk structures, respectively¹³⁵. For the hybrid-DFT calculations, the HSE (Heyd-Scuseria-Ernzerhof)¹³⁶ exchange-correlation functional with a short-range screening factor of 0.2 was employed. The portion of exact HF exchange potential of 15 and 25% are considered. An energy cutoff of 450 eV was applied for the plane-wave expansion of the electronic eigenfunctions. For geometry optimization and energy calculations, all atoms were fully relaxed using the conjugate gradient method until residual forces on constituent atoms became smaller than 1×10^{-2} eV/Å. The pristine Co₃O₄ was modeled using a 56-atom unit. For Brillouin zone sampling, (3×3×3) k-point mesh in the scheme of Monkhorst-Pack³⁸ was used for the structure.

The surface structure was modeled using a periodic (2×1) and (2×2) slabs with a thickness of 5 and 3 Co-layers, respectively, and a vacuum of 15 Å in the (111) direction. The Monkhorst-Pack type k-point sampling of (3×6×1) and (3×3×1) was used for (2×1) and (2×2) surface structures, respectively. Considering the undetermined electrical properties of cleaved surface structure, $U = 5.9$ eV, corresponding to the weighted average of U values for Co²⁺ and Co³⁺ ions, was used in the surface studies, as in the earlier theoretical study.¹³⁵ To simulate aqueous conditions, the implicit solvent model¹³⁷ was employed in the surface calculation, while explicit water molecules were also considered in certain cases to study the influence on the charge transfer.

6.3 RESULTS AND DISCUSSION

6.3.1 Bulk Properties of Co_3O_4 structure

Co_3O_4 exhibits a spinel structure with Co^{2+} and Co^{3+} ions on tetrahedral and octahedral sites, respectively [Fig. 6.1]. The lattice constants are predicted to be $a = b = c = 8.17 \text{ \AA}$, in close agreement with the experimental data ($a = b = c = 8.084 \text{ \AA}$).¹³⁸ The tetrahedral Co^{2+} and octahedral Co^{3+} ions are known to have high- ($3d^6: (e_g)^4(t_{2g})^6$) and low-spin ($3d^6: (t_{2g})^6$) configurations, respectively.¹³⁹

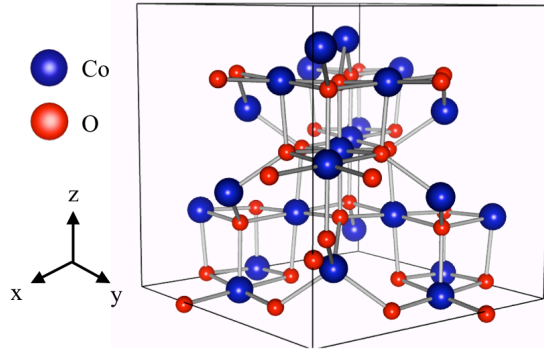


Figure 6.1 Atomic configuration of spinel Co_3O_4 structure; Co and O atoms are illustrated by blue and red balls, respectively.

Figure 6.2 (a) shows the electron density of states (DOS) projected onto Co^{2+} , Co^{3+} and O atoms of the bulk structure. The top of valence band (VB) mainly consists of Co^{2+} $3d$ minority-spin e_g states mixed with small amounts of Co^{3+} $3d$ - t_{2g} and O $2p$ states, while the bottom of conduction (CB) band consists of the hybridization of major Co^{3+} e_g and minor Co^{2+} t_{2g} states. The bands are separated by an energy gap of 2.0 eV in

agreement with the experimental data (ranged from 1.5 ~ 2.2 eV^{140,141,142}). In the valence band, the filled Co^{3+} t_{2g} states are predicted over an energy range from -5 ~ -1 eV overlapping with the Co^{2+} majority-spin t_{2g} states from -4 ~ -2 eV; here an intersection suggests interaction between the related states.

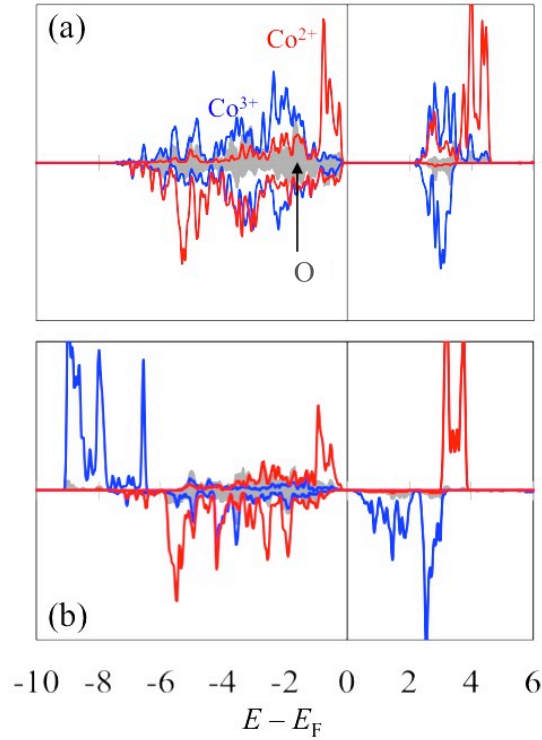


Figure 6.2 Electron density of states (DOS) of Co_3O_4 bulk structure composed of high-spin (a) and low-spin (b) Co^{3+} ions, projected onto Co^{2+} (red), Co^{3+} (blue) ion and O (grey shaded). The vertical line indicates the Fermi level position (E_F).

Based on our further investigations of the electronic structures, the predicted spin configuration for the Co^{3+} ion is actually dependent on the U values used in the

calculations. Using the same U values (4.4/6.7 eV for $\text{Co}^{2+}/\text{Co}^{3+}$), we predicted the high-spin Co^{3+} ($t_{2g}^4 e_g^2$) to be more favorable than the low-spin state (t_{2g}^6) by ~ 0.4 eV per ion. From there, we summarized the energy differences between high- and low-spin configurations calculated using various U values in Table 6.1. The high-spin configurations are successfully predicted when the U value for Co^{3+} ions is smaller than 4.5 eV. Here, the inadequate prediction of the correct spin configuration could be attributed to the overestimation of electron localization in Co^{3+} $3d$ states, which is explained shortly. Figure 6.2 (b) shows the DOS of matrix for the high-spin Co^{3+} ion. Compared to the low-spin case, Co^{3+} $3d$ states are predicted to shift downward; the energy gap is narrowed to about 0.5 eV. The majority-spin Co^{3+} $3d$ states are predicted below Co^{2+} $3d$ states, implying the absence of the aforementioned interaction with Co^{2+} $3d$ t_{2g} states.

| | | <u>Co³⁺</u> | | | | |
|------------------|------|------------------------|-------|------|------|------|
| U | | 3.50 | 4.50 | 5.50 | 5.90 | 6.70 |
| Co ²⁺ | 2.50 | −0.22 | 0.04 | 0.33 | 0.45 | 0.70 |
| | 3.50 | −0.31 | −0.12 | 0.17 | 0.29 | 0.54 |
| | 4.40 | −0.33 | −0.12 | 0.12 | 0.20 | 0.40 |
| | 5.90 | −0.35 | −0.13 | 0.10 | 0.19 | 0.38 |

Table 6.1 Energy difference between a low- and high-spin Co^{3+} ion in Co_3O_4 bulk structure calculated using various U values.

According to the molecular orbital theory, the half filled e_g states of high-spin Co in the octahedral site have strong antibonding interactions with surrounding O 2p states.

Therefore, the scenario implies that U values larger than 4.5 eV might overestimate the localization of d -electrons, leading to erroneously stable half-filled e_g states. Thus, the energetic penalty for switching from low- to high-spin to avoid the aforementioned interaction with Co^{2+} $3d$ states is underestimated. In fact, in a previous study of Co_3O_4 electronic structures, Qiao et al. also points out concern over the possibility of overestimating the U values of Co ions in the Co_3O_4 structure.¹⁴³ Since applying $U = 4.4/6.7$ eV for $\text{Co}^{2+}/\text{Co}^{3+}$ ions still well captures properties of the Co_3O_4 structure composed of low-spin Co^{3+} ions, the set of U values are used in this work. Meanwhile, for the comprehensiveness of this study, results calculated using different U values are also reported.

6.3.2 Co_3O_4 (111) Surface Structure

As it is reported to have the lowest surface energy and highest catalytic activity for the oxygen reduction reaction (ORR), Co_3O_4 (111) surface is employed in this study.¹³⁴ The slab structure with (111) surface is composed of alternating planes of oxygen and metal ions. Each metal layer consists of either three CoO_6 octahedra (Oct) or a CoO_6 octahedron and two CoO_4 tetrahedra (Oct/Tet); the Oct and Oct/Tet layers stack alternately, as shown in Fig. 6.3 (a). The stoichiometric slab structure $([\text{Co}_{\text{tet}}^{2+}]_{\text{m}}[\text{Co}_{\text{oct}}^{3+}]_{2\text{m}}\text{O}_{4\text{m}})$ is naturally polarized due to different terminations of the two opposite surfaces: Co-termination and O-termination [Fig 6.3 (a)].

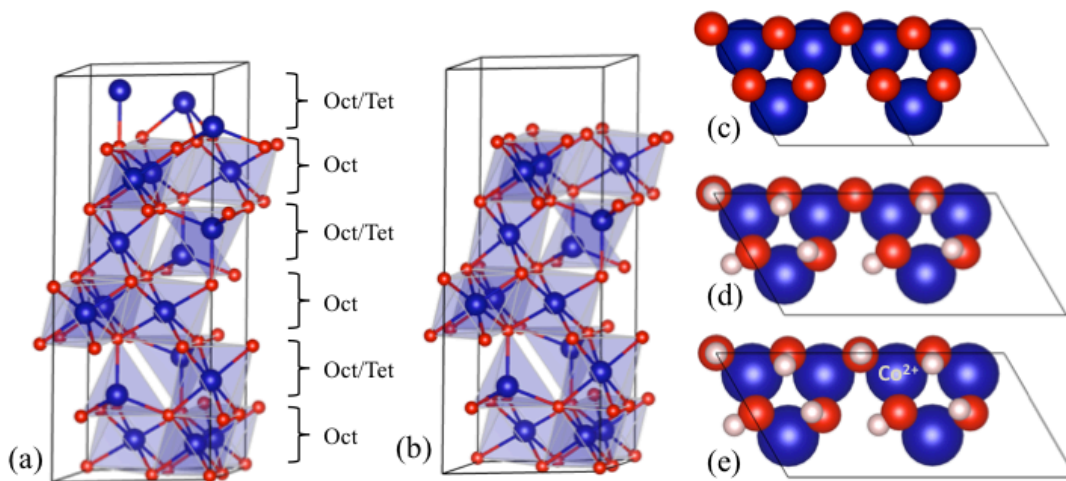


Figure 6.3 (a) Stoichiometric polar (111) surface structure. (b) Nonstoichiometric nonpolar (111) O-terminated surface structure and the related top view (c). (d) Top view of 7/8 ML (d) H-terminated surface structure. (e) Top view of fully H-terminated surface structure.

Both terminations have been reported in earlier experiments.^{144,145} Reflecting the reported tendency of undercoordinated metal atoms on the surface to have high surface energies,⁷⁷ the O-termination is chosen over Co-termination. To build a non-polar slab structure, two Co^{2+} and a Co^{3+} ion are removed from one side of the surface [Fig. 6.3 (b)]. Meanwhile, 7 Co^{3+} ions are oxidized to Co^{4+} to balance the charge ($[[\text{Co}_{\text{tet}}^{2+}]_{m-2}[\text{Co}_{\text{oct}}^{3+}]_{2m-1}\text{O}_{4m}]^{7+}$). In order to ensure the absence of polarity, a $2\times 1\times 1$ supercell is employed in this work to create an equal charge distribution on both surfaces; the subsurface layer on each side of the surface contains 7 Co^{4+} ions. Considering that the ORR of interest is operated in aqueous conditions, the H-terminated surface structure is utilized. The O-terminated

surface on top of the reducible Co^{4+} ions may be stabilized by the hydrogenation reaction as discussed in Chapter 4.

Before the hydrogenation reaction, the O-terminated $2 \times 1 \times 1$ surface structure has six 2-fold (O_{2c}) and two 3-fold (O_{3c}) undercoordinated O atoms on extreme surface layer, as shown in Fig 6.3 (c). Six octahedral Co atoms reside in the subsurface layer, each of them adjacent to two O_{2c} and an O_{3c} atom. On the H-terminated surface structure, all 8 O atoms on each surface are hydrogenated, excepting an O_{3c} atom [Fig 6.3 (d)]. While all 7 Co^{4+} ions on each subsurface layer are reduced to Co^{3+} ($\text{H}_7[\text{Co}_{\text{tet}}^{2+}]_m[\text{Co}_{\text{oct}}^{3+}]_{2m-1}\text{O}_{4m}$). The average H-binding energy is predicted to be -2.0 eV per H atom, with respect to half of an H_2 molecule; the magnitude is similar to the LiCoO_2 (111) H-terminated surface (~ -1.8 eV) studied in Chapter 4. Next, for the fully hydrogenated surface structure, the aforementioned O_{3c} atom is also hydrogenated. Following that, an octahedral Co^{3+} ion is predicted to be reduced to Co^{2+} in the subsurface layer ($\text{H}_8[\text{Co}_{\text{tet}}^{2+}]_m[\text{Co}_{\text{oct}}^{3+}]_{2m-2}[\text{Co}_{\text{oct}}^{2+}]\text{O}_{4m}$), as shown in Fig 6.3 (e). The length of the resulting $\text{Co}^{2+} - \text{O}$ bonds increase by 0.13 \AA with respect to $\text{Co}^{3+} - \text{O}$. The hydrogenation energy is calculated to be -1.71 eV. This magnitude is comparable with the aforementioned average H-binding energy, suggesting that the presence of fully hydrogenated surface structure is practical in experiments.

| | Method | Hydrogenation Energy |
|------------------------|---------|----------------------|
| DFT+U U(TET)/U(OCT) | 5.9/5.9 | – 1.71 |
| | 4.4/6.7 | – 2.01 |
| | 4.4/5.5 | – 1.57 |
| | 4.4/3.5 | – 0.86 |
| Hybrid DFT | 15 % | – 0.51 |
| | 25 % | – 1.05 |

Table 6.2 H-bonding energies on fully H-terminated surface structure; U(TET) and U(OCT) are U-values applied for the tetrahedral and octahedral Co atoms, respectively. The portion of Hartree-Fock exchange energy in HSE06 is marked in percentage.

Table 6.2 summarizes the H-bonding energies predicted using various U-values. As the U-values applied to the octahedral Co atoms are decreased, the H-binding energy decreases; the hydrogenation reaction of the surface becomes less favorable. The trend is attributed to the less localized $3d$ states enhancing the antibonding interaction of the newly reduced Co^{2+} ion and O. The fully hydrogenated $2\times 1\times 1$ surface structure has six hydrogenated O_{2c} ($\text{O}_{2c\text{-H}}$) and two hydrogenated O_{3c} ($\text{O}_{3c\text{-H}}$) atoms. It is worth mentioning that for every three HO_{2c} surrounding a void on the surface, a hydrogen bond is predicted to exist between two of them, providing a possible proton-shuttling route between two $\text{O}_{2c\text{-H}}$ atoms.

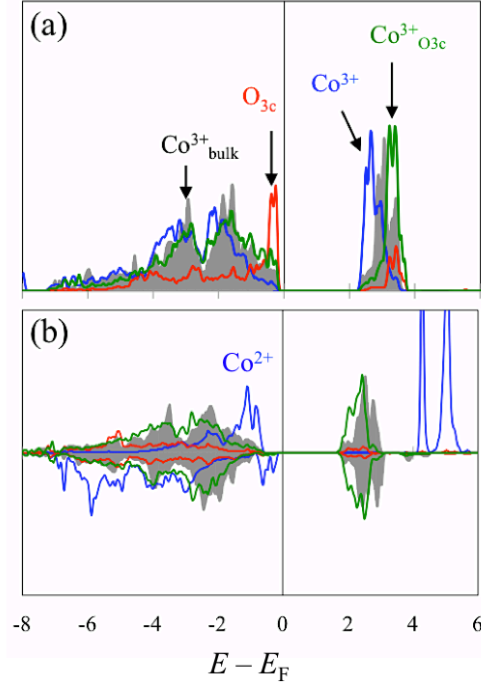


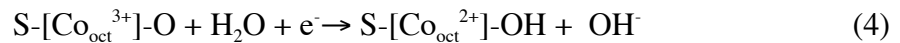
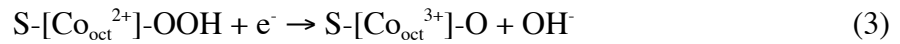
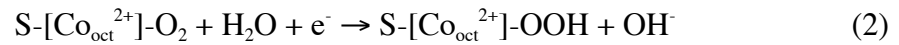
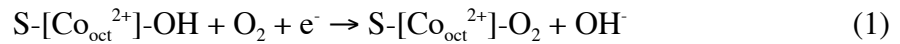
Figure 6.4 Electron density of states (DOS) of partially (a) and fully (b) H-terminated Co₃O₄ (111) surface structure. In (a), the DOS is projected onto Co³⁺ adjacent to 1O_{3c}/2HO_{2c} (green), 1HO_{3c}/2HO_{2c} (blue) and in the bulk (gray shade), and O_{3c} (red) atom. In (b), the blue denotes Co²⁺ ion adjacent to 1O_{3c}/2HO_{2c}.

Figure 6.4 shows the DOS of partially ($\text{H}_7[\text{Co}_{\text{tet}}^{2+}]_{\text{m}}[\text{Co}_{\text{oct}}^{3+}]_{2\text{m}-1}\text{O}_{4\text{m}}$) and fully ($\text{H}_8[\text{Co}_{\text{tet}}^{2+}]_{\text{m}}[\text{Co}_{\text{oct}}^{3+}]_{2\text{m}-2}[\text{Co}_{\text{oct}}^{2+}]\text{O}_{4\text{m}}$) H-terminated surface structures. In the partially H-terminated case [Fig. 6.4 (a)], the VB and CB mainly consist of O_{3c} 2p and well-coordinated Co³⁺ 3d states (Co³⁺ ion adjacent to a O_{3c-H} and two HO_{2c-H}), respectively. An energy gap of 2.1 eV is predicted, almost the same as the bulk, suggesting the H-terminated surface structure is well stabilized. Right below the Fermi level, the hybridization of O_{3c} 2p and Co³⁺_{O_{3c}} 3d states (Co³⁺ ion adjacent to a O_{3c} and two O_{2c-H}) is attributed to the stronger antibonding interaction induced by unstable 2p electrons. For

the same reason, the empty e_g states of $\text{Co}^{3+}_{\text{O3c}}$ are predicted to be higher than those of well-coordinated Co^{3+} . In the fully H-terminated surface structure [Fig. 6.4 (b)], the VB consists of Co^{2+} $3d$ states, implying that the hydrogenation reaction reduces a Co^{3+} ion to Co^{2+} ; this Co^{2+} ion is predicted to have high-spin states ($t_{2g}^5 e_g^2$). The prediction of nearly non-bonding $3d$ states is consistent with the elongated $\text{Co}^{2+} - \text{O}$ bond. Compared to the partially H-terminated case, the $\text{O}_{3\text{c-H}}$ $2p$ states are largely shifted downward as the $\text{H} - \text{O}$ bond stabilizes the $2p$ electrons. Meanwhile, the CB remains constituted of surface Co^{3+} $3d$ states, indicating that additional electrons could be injected to the surface.

6.3.3 Reaction Pathway

Next, a four-electron ORR reaction pathway for the Co_3O_4 (111) fully hydrogenated non-polar surface structure at the cathode in alkaline condition is proposed (overall process $\text{O}_2 + \text{H}_2\text{O} + 4e^- \rightarrow 4\text{OH}^-$).



For the simplicity, the chemical formula of $\text{H}_8[\text{Co}_{\text{tet}}^{2+}]_m[\text{Co}_{\text{oct}}^{3+}]_{2m-2}[\text{Co}_{\text{oct}}^{2+}]\text{O}_{4m}$ is written in $\text{S}[\text{Co}_{\text{oct}}^{2+}]\text{-OH}$, where S denotes the rest of the slab structure ($\text{H}_7[\text{Co}_{\text{tet}}^{2+}]_m[\text{Co}_{\text{oct}}^{3+}]_{2m-2}\text{O}_{4m-1}$), as the active site is identified as the octahedral Co atoms on the surface.

| U-Values | OH removal | O ₂ adsorption | $\Delta H(\text{eq1})$ (*OH \rightarrow *O ₂ ^{δ^-}) | $\Delta H(\text{eq2})$ (*O ₂ ^{δ^-} \rightarrow *OOH) | $\Delta H(\text{eq3})$ (OOH* \rightarrow *O) | $\Delta H(\text{eq3})$ (O* \rightarrow *OH) |
|-----------------|------------|---------------------------|---|---|---|--|
| Co(TET)/Co(OCT) | | | | | | |
| 5.9/5.9 | – 1.25 | – 0.22 | – 1.48 | – 0.76 | – 1.90 | – 1.60 |
| 4.4/6.7 | – 1.52 | 0.01 | – 1.52 | – 0.65 | – 1.67 | – 1.90 |
| 4.4/5.5 | – 1.11 | – 0.30 | – 1.42 | – 0.82 | – 2.03 | – 1.46 |
| 4.4/3.5 | – 0.52 | – 0.67 | – 1.18 | – 1.10 | – 2.07 | – 0.75 |

Table 6.3 Removal and adsorption energies of *OH and *O₂ on Co₃O₄ (111) H-terminated surface, respectively, and enthalpies of each reaction steps are calculated using various U values.

Table 6.3 summarizes the predicted enthalpies for each reaction calculated using different U values. The reaction scheme is intuitively similar to that suggested for the perovskite LaBO₃ structure in a previous study.¹⁴⁶ The total energy of the OH[–] anion is calculated as the difference in energies of a H₂O and half of H₂ molecule ($E(\text{OH}) = E(\text{H}_2\text{O}) - 1/2 E(\text{H}_2)$) as defined in ref 140.¹⁴⁷ Removing a *OH bounded to two Co atoms on a (111) Co₃O₄ surface structure creates an active site for the ORR. We first calculate the *OH removal energy as a Co³⁺ is reduced to Co²⁺. Next, the adsorption energy of an O₂ molecule (*O₂) is predicted. Next, the injection of a second electron and subsequent formation of *OOH through the interaction of *O₂ with a proton from a water molecule is studied. As the third electron is injected, we calculate the energy needed to break the *O–OH bond and form *O. Finally, the ORR cycle is closed by the hydrogenation reaction of *O creating a fully hydrogenated surface structure as discussed in Section 6.3.2.

6.3.4 Mechanisms for ORR

In this section, we discussed the mechanism of these reaction steps in detail. For each step, an additional electron is first injected to the surface structure. The Fermi shift for injecting an excess electron to the fully hydrogenated structure is predicted to be 0.47 eV. In all cases, the excess electron is predicted to reduce a surface Co^{3+} ion to Co^{2+} before the reaction takes place.

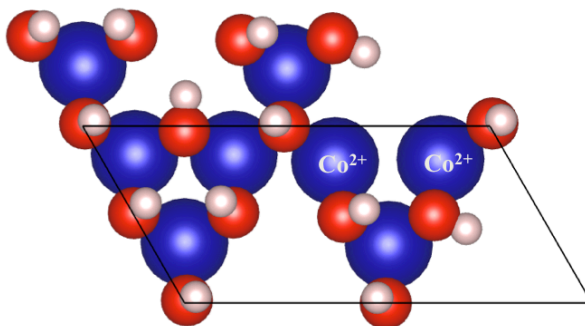


Figure 6.5 $\ast\text{OH}$ removal (0.13 ML) on Co_3O_4 (111) H-terminated surface structure

The H-terminated surface structure with an additional electron contains two Co^{2+} ions; they are separated to reduce the repulsive interaction. Using the explicit solvent model, an H-terminated O_{2c} (HO_{2c}) is predicted to be further hydrogenated to form a water molecule; this weakens the binding strength between HO_{2c} and the adjacent Co^{2+} ion greatly. Thus, the reaction is equivalent to the desorption of an OH^- ion from surface structure [Fig. 6.5]. The OH^- anion removal energy is calculated to be -1.02 eV, implying that removing an OH^- ion from a reduced surface structure is energetically favorable. The removal energy is predicted to decrease with decreasing U values applied to octahedral Co atoms [Table 6.3], which is attributed to the stronger Co^{2+} -O antibonding interaction

as discussed in Section 6.3.2. After the OH^- anion is removed from the surface, two neighboring 5-fold undercoordinated Co^{2+} ions are predicted to exist on the surface, implying that excess electrons tend to localize on undercoordinated Co atoms. This could be due to stabilization of the direct $\text{Co}^{2+} - \text{O}$ antibonding interaction by the slight distortion in the electron distribution.

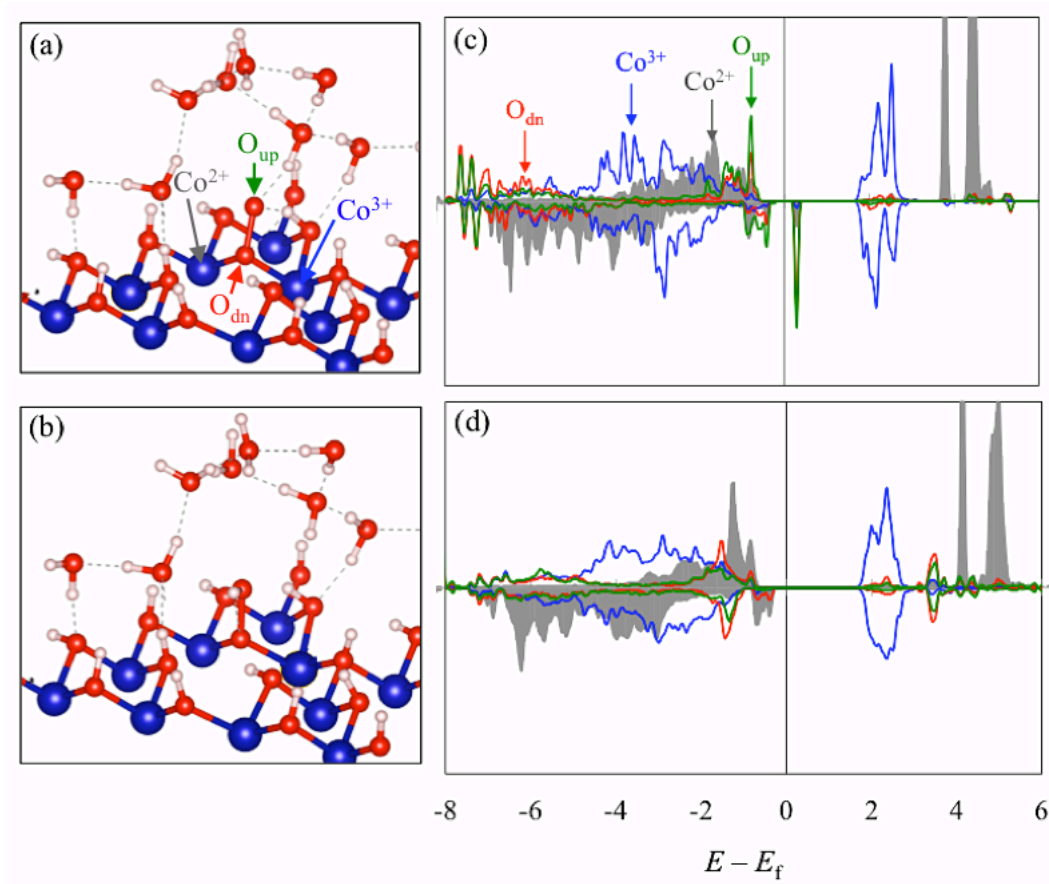


Figure 6.6 Structures and electron density of states (DOS) of Co_3O_4 (111) H-terminated surface with adsorbate (a) *O_2 and (b) *OOH , projected onto Co^{3+} (blue), Co^{2+} (grey shaded) adjacent to the adsorbate, O of the adsorbate adjacent to the surface (red) and exposed to the solution (green).

Next, the adsorption reaction of an O₂ molecule (*O₂) on two neighboring 5-fold coordinated Co²⁺ ions is predicted [Fig. 6.6 (a)]. We found that the charge state of *O₂ depends on (1) the type of model used to describe the water solutions and (2) the U-values. Using the implicit solvent model, the bond length of the adsorbed oxygen molecule is predicted to be ~ 1.3 Å, suggesting an incomplete electron transfer from a Co²⁺ ion to the superoxyl-like O₂ molecule (*O₂^{δ-}). On the other hand, when using the explicit solvent model, the bond length is predicted to be ~1.35 Å, implying the formation of a superoxyl (*O₂⁻) anion. Meanwhile, one of the two Co²⁺ ions adjacent to the *O₂⁻ anion is oxidized to Co³⁺. These predictions suggest that the water network is important in facilitating the charge transfer for O₂ adsorption.

| U-Values | $\Delta E(*O_2^{\delta-}/*O_2^-)$ | $\Delta H(\text{eq1})$ | $\Delta H(\text{eq2})$ |
|-----------------|-----------------------------------|-------------------------------------|--------------------------------------|
| Co(TET)/Co(OCT) | | (*OH→*O ₂ ⁻) | (*O ₂ ⁻ →*OOH) |
| 5.9 | 0.32 | - 1.17 | - 1.08 |
| 4.4/6.7 | 0.41 | - 1.11 | - 1.06 |
| 4.4/5.5 | 0.25 | - 1.18 | - 1.07 |
| 4.4/3.5 | - 0.16 | - 1.34 | - 0.95 |

Table 6.4 Difference of adsorption energies of partially (*O₂^{δ-}) and fully (*O₂⁻) charge transfer to the superoxyl anion on Co₃O₄ (111) H-terminated surface structure; the enthalpies of step 1 and 2 are calculated based on the fully charge transfer case.

The energy differences between the predicted *O₂^{δ-} and *O₂⁻ anions on surface using the implicit solvent model are summarized in Table 6.4. When smaller U-values are

applied to Co^{3+} ions, the formation of $^*\text{O}_2^-$ gradually becomes more stable due to the less localized valence electron on the Co^{2+} ion. It is worth mentioning that having a peroxy ($^*\text{O}_2^{2-}$) anion on the surface is predicted to be energetically less favorable than $^*\text{O}_2^-$ by about 0.4-0.6 eV.

For consistency, the adsorption energy predicted using the implicit solvent model is used to study the ORR reaction here. The adsorption energy of an O_2 molecule bound to two 5-fold coordinated Co^{2+} ions is calculated to be -0.23 eV, close to the O_2 adsorption on perovskite metal oxides (~ -0.2 eV) studied in previous works.¹⁴⁸ Table 6.3 summarizes the adsorption energies calculated using different U values for octahedral Co ions. The adsorption of O_2 becomes more favorable with decreasing U-values, which is expected as charge transfers more easily when it is less localized. By combining the $^*\text{OH}^-$ removal with $^*\text{O}_2^{\delta-}$ adsorption, the enthalpies of step 1 ($^*\text{OH}/^*\text{O}_2$ exchange) are summarized in Table 4., while the enthalpies calculated by assuming the formation of $^*\text{O}_2^-$ (full charge transfer) on surface are summarized in Table 6.5.

Figure 6.6 (b) shows the DOS of the structure with O_2 adsorbed on the surface projected onto O_2 , Co^{2+} and Co^{3+} ions adjacent to the O_2 molecule. The VB consists of $^*\text{O}_2^-$ 2p and Co^{2+} 3d states, while the CB is mainly $^*\text{O}_2^-$ 2p states; the formation of the superoxyl anion is confirmed. Meanwhile, the presence of filled Co^{3+} t_{2g} states in the valence bands implies an electron transfers from one of the two initial Co^{2+} ions (adjacent to O_2) to $^*\text{O}_2^-$.

Based on this adsorption configuration, the interaction of water molecules with the $^*\text{O}_2^-$ anion via a hydrogen bonding network is predicted using explicit solvent. In step

2, upon the addition of an electron the free energy change of creating a $^*\text{OOH}^-$ anion along with an OH^- anion in solution is calculated to be around -0.8 eV, similar to the number predicted for perovskite (from -0.40 to -0.73 eV) by Wang et al.¹⁴⁸ The atomic configuration of the surface structure with $^*\text{OOH}^-$ is illustrated in Figure 6.6 (c). The reaction is predicted to be more favorable as the U-value decreases as the enhanced charge transfer from Co^{2+} ion to $^*\text{O}_2$ facilitates the formation of OOH. Figure 6.6 (d) shows the DOS of the surface structure with $^*\text{OOH}$ adsorbed on the surface. The VB and CB consist of Co^{2+} and Co^{3+} 3d states, respectively. In comparison to the case of $^*\text{O}_2^-$ on the surface, the downshift of $^*\text{OOH}^-$ 2p states indicates stabilization due to the hydrogenation reaction. Meanwhile, the absence of O 2p states above Fermi level implies that the excess electron transfers from a Co^{2+} ion on surface to the $^*\text{OOH}^-$ anion.

In step 3, by removing an OH^- anion from $^*\text{OOH}^-$, an excess electron transfers to the newly created 2-fold undercoordinated O atom as both Co^{2+} ions in the subsurface layer are oxidized to Co^{3+} . This reaction enthalpy is calculated to be -1.28 eV. In addition, we found that moving a proton from a 3-fold coordinated O atom to the 2-fold undercoordinated O atom lowers the total energy by 0.58 eV. The presence of 3-fold undercoordinated O atom after step 3 is considered assuming the shuttling of a proton via the hydrogen-bonding network on the hydrophilic surface structure.

In addition to step 3, a possible two-electron pathway for ORR to form an H_2O_2 molecule is also examined here. As HO_{2c} on the surface forms a hydrogen bond with $^*\text{OOH}$ [Fig. 6.7], the creation of an H_2O_2 molecule through proton transport is considered. The enthalpy of $\text{S}[\text{Co}_{\text{oct}}^{2+}]\text{-OOH} + \text{H}_2\text{O} + e^- \rightarrow \text{S}[\text{Co}_{\text{oct}}^{2+}] + \text{H}_2\text{O}_2 + \text{OH}^-$ is

predicted to be -0.96 eV. The exothermic reaction could be related to the two-electron pathway for ORR in some cases of carbon-supported Co_3O_4 in the previous experimental work;¹⁴⁹ however, considering that the predicted enthalpy of step 3 is more favorable than the H_2O_2 formation by 0.32 eV, the four-electron pathway for ORR still holds while ignoring the charge-transfer barrier during reactions.

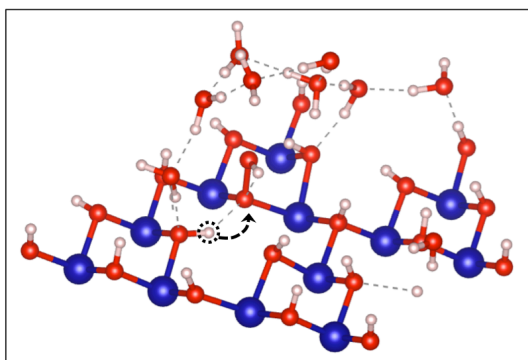


Figure 6.7 Illustration of in-plan H-bonding between HO_{2c} and OOH on Co_3O_4 (111) H-terminated surface structure.

Finally, as discussed in Section 6.3.2, injecting an electron to the partially H-terminated surface structure (with subsurface layer composed of only Co^{3+} ions) leads to the formation of a fully hydrogenated surface. The hydrogenation reaction creates an OH^- ion in solution, closing the ORR reaction cycle.

6.3.5 The Free Energy Diagram

The free energy diagram is calculated based on the computational hydrogen electrode model proposed by Nørskov et al.¹⁵⁰ The change in Gibbs free energy for each

reaction step involved in the proposed mechanism for ORR is calculated using the following equation:

$$\Delta G = \Delta E + \Delta ZPE - T\Delta S + e\Phi \quad (4.3.1)$$

where ΔE is the reaction energy, ΔZPE is the change in zero point energy, T is the reaction temperature, and ΔS is the change in entropy, and $e\Phi$ is the product of the elementary charge (e) transferred and the applied potential (Φ) versus reversible hydrogen electrode (RHE). The ΔZPE are calculated using VASP by considering operation within the harmonic approximation while ΔS is cited from the NIST database.^{151,152} The equilibrium potential (Φ_{eq}) is defined as the theoretical maximum cell voltage for the ORR, i.e. $[\Delta G(H_2O) - \Delta G(H_2) - 1/2 \Delta G(O_2)]/2e$. The ORR potential (Φ_{ORR}) corresponds to the highest potential at which all reaction steps are predicted to be exothermic, i.e. the free energy diagram is downhill along the pathway. The overpotential is then calculated by $\eta = \Phi_{eq} - \Phi_{ORR}$.

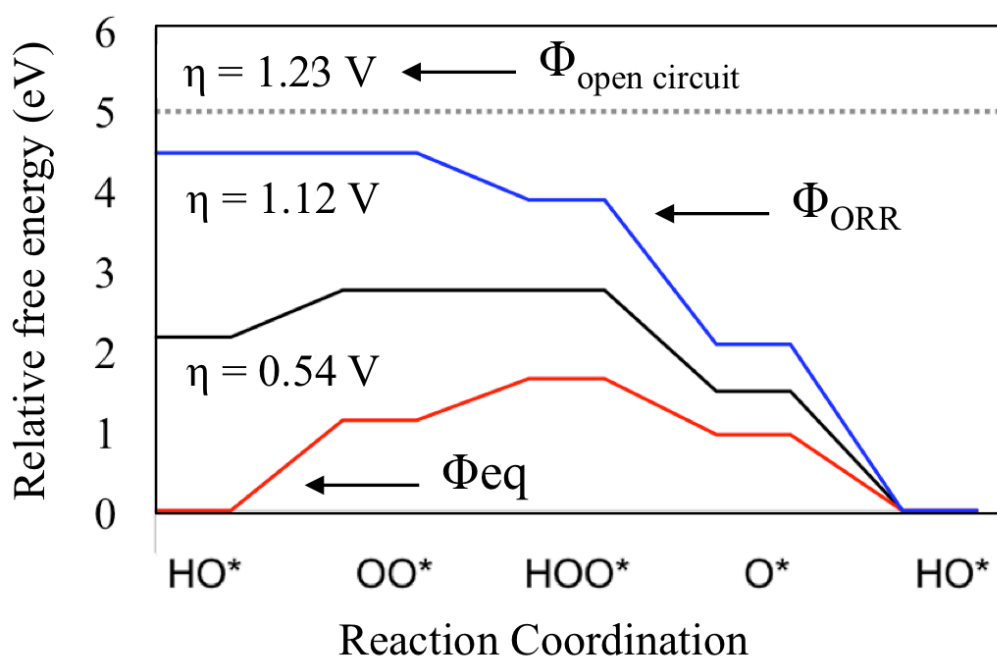


Figure 6.8 Free energy diagrams of the four-electron pathway for ORR on the Co_3O_4 (111) H-terminated surface structure. The red line represents the reaction at equilibrium (Φ_{eq}) potential corresponding to the zero electrode potential (0 V vs. RHE). The blue line represents the ORR potential (Φ_{ORR}) corresponding to the over potential (η) where all reaction steps along pathway are predicted downhill regarding to the free energies. The dashed line represents the theoretical open circuit potential.

Figure 6.8 shows the free energy pathway of the ORR on the Co_3O_4 (111) surface. The pathway is calculated based on the discussed reaction steps in this work using the implicit solvent model. At the equilibrium potential, Φ_{eq} , step 1 and 2 are predicted to be uphill while step 3 and 4 are downhill, indicating that the first two steps of the ORR process, i.e. $^*\text{OH}/^*\text{O}_2$ exchange and hydrogenation of $^*\text{O}_2$, are the rate-limiting steps; the result is similar to the case of perovskite oxide surfaces studied in ref 11 as well as in the case of the Pt (111) surface studied by Nørskov et al.¹⁵⁰ As the applied potential is increased to 0.54 V, step 1 becomes the only rate-limiting step, implying that the

*OH/*O₂ is the potential-determining step of the ORR. The overpotential for the ORR is predicted to be 1.12 V (Φ_{ORR}) when all reaction steps are predicted to be downhill along the pathway, suggesting that the proposed four-electron pathway is physical in terms of conducting an exothermic ORR in alkaline condition. It is worth mentioning that the enthalpies of step 1 and step 2 become comparable when $U=4.4$ eV is applied to the octahedral Co atoms [Table 6.4]. Meanwhile, complete charge transfer to *O₂⁻ is also predicted. The results suggest that the determination of potential-limiting step is related to the tendency of charge to localize on the surface. Following that, the enthalpy of step 1 and 2 calculated by considering the fully charge transferred case (*O₂⁻) are summarized in Table 6.5. In this case, the enthalpies of the two steps are actually similar when moderately lowering the U -values (5.5 eV) for octahedral Co atoms. Considering the possible overestimation of U values for the Co₃O₄ structure discussed in Section 6.3.1, the *OH/*O₂ exchange and hydrogenation of *O₂ could be similar in regards to determining the overpotential of the ORR.

6.4 SUMMARY

Using DFT-GGA calculations, a four-electron pathway for the Co₃O₄ (111) surface structure is investigated. Starting with the bulk structure, we found the U values (Co²⁺: 4.4, Co³⁺: 6.7) adopted by previous theoretical studies might be overestimated based on the prediction of high-spin octahedral Co³⁺ ions in the matrices. Based on that, different U values were examined; the low-spin states are predicted by applying U values smaller than 4.4 eV for Co³⁺ ions. Considering that applying 4.4/6.7 eV for Co²⁺/Co³⁺ ions

still well captures the bulk properties of the Co_3O_4 structure (composed of low-spin Co^{3+} ions), the set of U values are used in this work. Meanwhile, for the comprehensiveness of the studies, we reported results calculated using different U values.

Considering the ORR is performed in aqueous conditions, the H-terminated surface structure is employed. For a fully H-terminated surface structure, the ratio of Co^{3+} and Co^{2+} ions in the subsurface layer is 5:1. Based on the surface structure, reaction steps related to the charge injection are discussed and the related enthalpies are calculated. Using the implicit solvent model, we first predicted the exothermic reaction of creating an OH^- removal on the surface by injecting an electron to the slab structure; two adjacent undercoordinated Co^{2+} ions are formed. The adsorption of an O_2 molecule ($^*\text{O}_2$) bound to the two Co^{2+} ions is then predicted. To simulate a full charge transfer from a Co^{2+} ion to $^*\text{O}_2$, forming superoxyl, the explicit solvent model is required. This suggests that the prediction of charge transfer is sensitive to the H-bond network. Next, the second injected electron induces proton transfer from a H_2O molecule to the $^*\text{O}_2$, creating $^*\text{OOH}$ on the surface. The DOS analysis illustrates the downward shift of $^*\text{O}_2$ $2p$ states, indicating that the protonation stabilizes the adsorption configuration. For the injection of the third electron, removing an OH^- anion from $^*\text{OOH}$ is calculated to be exothermic. Moreover, the surface structure is further stabilized as a proton transfers from a 3-fold coordinated O_{3c} to the newly formed 2-fold undercoordinated O_{2c} atoms. Finally, along with the injection of the fourth electron, the undercoordinated 3-fold oxygen is protonated; hence, the surface structure returns to the fully H-terminated surface. It is worth mentioning that we also examined the possible two-electron pathway involving the oxidation of

OOH to an H_2O_2 molecule. Our calculation shows the reaction step is energetically less favorable than the desorption of OH^- (step 3), implying the four-electron pathway is preferred. Nonetheless, the formation of H_2O_2 is actually predicted to be exothermic, suggesting the possibility for ORR occurring through the two-electron pathway; this finding could be related to the experimental observation that a certain carbon support is needed for Co_3O_4 to catalyze ORR via four-electron pathway. Finally, the free energy diagram of the above intermediate steps for ORR is constructed. The diagram illustrates that the $^\text{OH}/^*\text{O}_2$ exchange reaction is the potential limiting step.

Chapter 7 : Investigation of Metal-Oxide Cathode Materials for Lithium Ion Batteries: Phosphate Deficient LiFePO_4 and FePO_4

7.1 INTRODUCTION

Lithium iron phosphate LiFePO_4 (LFP) has recently emerged as an attractive cathode material for next-generation lithium ion batteries (LIBs) because of its remarkable thermal and chemical stability, nontoxicity, low cost, and high intercalation voltage (≈ 3.5 V) as well as theoretical capacity (≈ 170 mAh/g).^{153,154} However, the practical use of LFP is hampered by its intrinsically poor electrical and ionic conductivities.^{155,156} Considerable efforts have been made to overcome these drawbacks, including heterogeneous doping and defect engineering. For instance, aliovalent doping with Nb, Mg, Zr, Ti has been demonstrated to enhance the LFP electrical conductivity by eight orders of magnitude up to about 10^{-2} S/cm¹⁵⁷ (which is comparable to that of the most commonly used LiCoO_2 and LiMn_2O_4).¹⁵⁸ In addition, proper control of naturally occurring defects (such as Li vacancies/interstitials) and Li-Fe ion exchanging antisite defects has been also suggested to have positive impacts on Li mobility enhancement.^{159,160,161} While the underlying mechanisms still remain a controversial topic, the above findings seed the idea of enhancing the electronic and ionic conduction simultaneously in LFP via structural modifications at the atomic level. Very recently, a viable synthesis method was proposed to control the polyanion deficiency in a lithiated metal phosphate matrix, but the atomic details have not been explored. In this work, we assess the structure, stability and mechanical properties of phosphate (PO_4) -deficient

LFP and FP based on density functional theory (DFT) calculations.

7.2 METHODOLOGY

All atomic structures and energies reported herein were calculated using spin-polarized DFT within the generalized gradient approximation (GGA-PBE)^{15,16} as implemented in the Vienna Ab initio Simulation Package (VASP)^{32,33}. The projected augmented wave (PAW) method^{162,163} with a plane-wave basis set was employed to describe the interaction between ion core and valence electrons. To treat the strong on-site $3d$ electron-electron interactions on Fe an additional Hubbard-U term was added (with an effective value of $U_{\text{eff}} = 4.3$ eV)⁸³. Valence configurations employed are as follows: $3d^6 4s^2$ for Fe, $3s^2 3p^2$ for P and $2s^2 2p^4$ for O. An energy cutoff of 450 eV was applied for the plane-wave expansion of the electronic eigenfunctions. For geometry optimization and energy calculations, all atoms were fully relaxed within periodic supercell considered, using the conjugate gradient method until residual forces on constituent atoms became smaller than 1×10^{-2} eV/Å. The pristine LiFePO_4 (FePO_4) was modeled using a 28(24) -atom unit cell while the PO_4 -deficient structure was created by removing a PO_4 unit from an expanded $(1 \times 2 \times 3)$, 168(144)-atom LiFePO_4 (FePO_4) supercell. For Brillouin zone sampling, $(3 \times 4 \times 5)$ and $(3 \times 3 \times 1)$ k-point mesh in the scheme of Monkhorst-Pack¹⁶⁴ was used for the pristine and PO_4 -deficient FePO_4 , respectively.

7.3 RESULTS AND DISCUSSION

7.3.1 Pristine Bulk Structure

Figure 7.1 shows the optimized structure of orthorhombic olivine LiFePO_4 (LFP) and FePO_4 (FP) (space group Pnma) using GGA+U functional. In LFP matrix, Li^+ and Fe^{2+} ions occupy M1 and M2 octahedral sites, respectively, which form layers spanned on (100) plane and are ordered alternately with planes formed by $(\text{PO}_4)^{3-}$ tetrahedra in [100] direction, where each PO_4 unit is connected to 5 FeO_6 units. Delithiated FePO_4 has the same structure to LiFePO_4 with only difference from empty Li octahedral sites. The calculated lattice constants: $a = 10.45 \text{ \AA}$, $b = 6.08 \text{ \AA}$, $c = 4.76 \text{ \AA}$ for LFP and $a = 9.97 \text{ \AA}$, $b = 5.91 \text{ \AA}$, $c = 4.88 \text{ \AA}$ for FP are in good agreement with the experimental values of 10.34 \AA , $b = 6.06 \text{ \AA}$, $c = 4.7 \text{ \AA}$ and $a = 9.76 \text{ \AA}$, $b = 5.75 \text{ \AA}$, $c = 4.76 \text{ \AA}$, respectively.¹⁶⁵ The slight overestimation of lattice constant is mainly attributed to the well-known tendency of GGA to underestimate the bond strength.

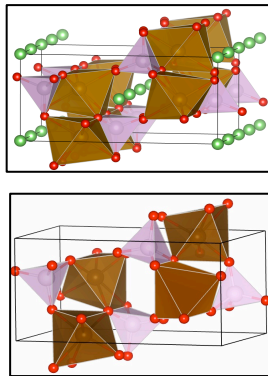


Figure 7.1 The atomic configuration of LiFePO_4 and FePO_4 with brown octahedra and pink tetrahedra represent FeO_6 and PO_4 units, respectively; Green and red balls represent Li and O atoms, respectively.

Figure 7.2 shows the electron density of states (DOS) projected onto Fe, P, and O atoms of pristine LFP and FP. The Fermi level is used as a reference energy, which is set to zero. In FP, the top of valance band (VB) is mainly occupied by filled O 2p states ($-4 \sim 0$ eV) with limited hybridization with half-filled Fe 3d states, while the later states are mostly shown in energy range of $-8 \sim -6$ eV; The bottom of conduction band (CB) is occupied by empty minority-spin Fe 3d- t_{2g} states, rendering a gap of 1.75 eV very close to experimental value (1.7 eV).¹⁶⁶

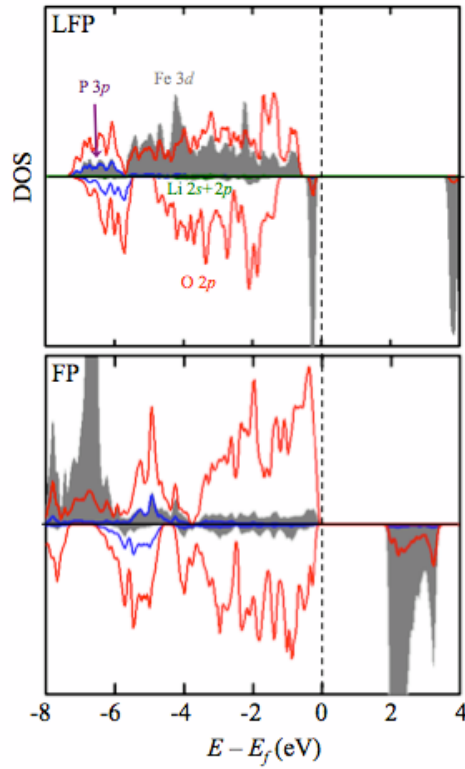


Figure 7.2 The electron density of states (DOS) projected onto Li, Fe, P and O atoms in (a) LiFePO_4 and (b) FePO_4 with Fermi level indicated by dash line.

A strong ionic character of $\text{Fe}^{3+}-\text{O}^{2-}$ bonds predicted in FP suggests the half-filled Fe $3d$ bands are relatively more stable than O $2p$ bands, preventing the two bands from hybridization. In the energy range of $-6 \text{ eV} \sim -4 \text{ eV}$, P $3p$ and O $2p$ states are predicted largely overlapped, suggesting the strong covalent P – O binding interaction. As such, PO_4 units can play an important role in stabilizing LFP/FP structures. In LFP, Fe^{3+} ions are reduced into Fe^{2+} with electrons donated by Li atoms during the lithiation reaction. The partially filled minority-spin Fe $3d$ - t_{2g} states split and are predicted to be the VB and CB, opening up a gap predicted to be 3.8 eV in an agreement with experimental result ($3.8 - 4.0 \text{ eV}$).^{166,167} As depicted in the DOS, the VB is highly localized and barely hybridized with O $2p$ orbitals. The same result has also been reported in the earlier study, in which Zaghbi et al. explained that Madelung energy raise redox energy of $\text{Fe}^{2+/3+}$ above O^{2-} to stabilize the Fe^{2+} and O^{2-} ions of the LFP structure.¹⁶⁸ Moreover, splitting from the t_{2g} states, the overlap of the VB and O $2p$ orbitals would also naturally be less significant. Compared with the FP, LFP has a more significant overlap of Fe $3d$ and O $2p$ states in the energy range of $-5.5 \sim -0.5 \text{ eV}$. The rise of the Fe $3d$ bands could result from the interaction between the VB and the spin-majority Fe $3d$ states. At the mean time, our calculations show that the Coulomb interaction between Li^+ and O^{2-} can bring down the energy of O $2p$ bands, which may further increase the overlap.

7.3.2 PO₄-deficient FePO₄ Structure

We examined how the deficiency of phosphate (PO₄) polyanions alters the electronic structure and geometry of FePO₄. As depicted in Fig. 7.3 (a) (inset), a PO₄-deficient structure was created by removing a neutral PO₄ unit ($V_{PO_4}^0$) from a FePO₄ supercell with 24 PO₄ units. While neighboring atoms are noticeably displaced, four of the five Fe atoms adjacent to $V_{PO_4}^0$ become fivefold coordinated and the rest is fourfold coordinated. The removal of a neutral PO₄ unit leaves three unpaired electrons which tend to localize on adjacent Fe atoms.

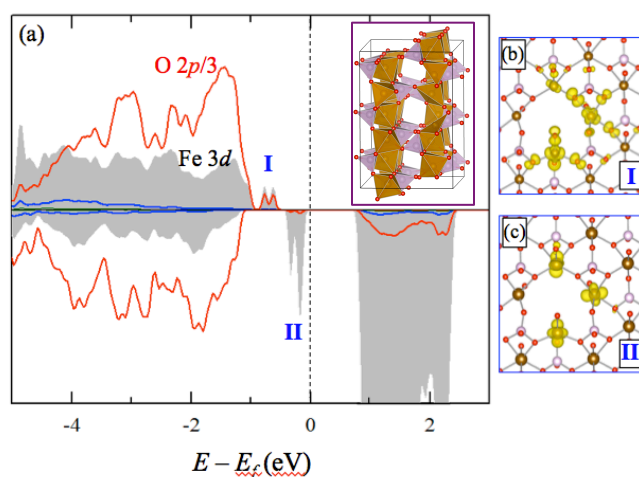
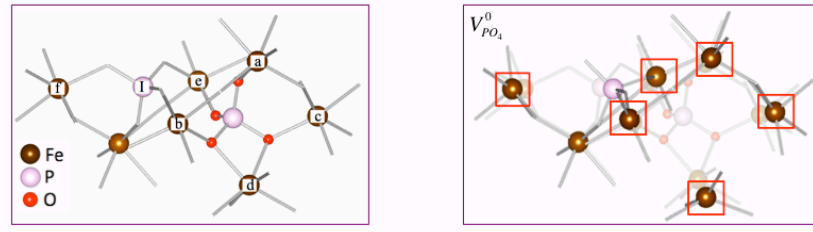


Figure 7.3 (a) The DOS of PO₄-deficient FePO₄ [note the intensity of O 2p state is rescaled by 1/3]. (b) and (c) The band-decomposed charge densities corresponding to defect states I and II are plotted with an isosurface value of 0.005 electron/Å³.

As presented in Fig. 7.3 (a), the projected DOS of the PO₄-deficient structure exhibits two distinct defect states within the band gap. One defect level (indicated as I) lies just above the VB, and the other (II) is in the middle of the gap. The defect state I

shows overlap between spin-up Fe 3*d* and O 2*p* orbitals while spreading over neighboring Fe and O atoms (as demonstrated by the band decomposed charge density plot in Fig. 7.3 (b); this suggests that the defect level is associated with the lattice distortions around $V_{PO_4}^0$. On the other hand, as shown in Fig. 7.3 (c), the excess electrons associated with defect state II seem to be highly localized on three neighboring Fe atoms; this is not surprising considering that Fe 3*d* states dominate the bottom of the CB in FePO₄, and thus they readily accept excess electrons.



| $V_{PO_4}^q$ | Fe_a | Fe_b | Fe_c | Fe_d | Fe_e | $Fe_f - P_f$ |
|--------------|-----------|-----------|-----------|-----------|-----------|--------------|
| Pristine | 3+ / 3.21 | 3+ / 3.22 | 3+ / 3.22 | 3+ / 2.82 | 3+ / 3.26 | 3+ / 3.22 |
| 0 | 2+ / 3.25 | 3+ / 3.46 | 2+ / 3.34 | 2+ / 3.33 | 3+ / 3.62 | 3+ / 4.08 |
| +1 | 2+ / 3.32 | 3+ / 3.49 | 3+ / 3.49 | 2+ / 3.45 | 3+ / 3.60 | 3+ / 3.46 |
| -1 | 2+ / 3.25 | 3+ / 3.49 | 2+ / 3.34 | 2+ / 3.33 | 3+ / 3.60 | 2+ / 3.95 |
| -2 | 2+ / 3.32 | 2+ / 3.36 | 2+ / 3.35 | 2+ / 3.38 | 2+ / 3.61 | 3+ / 3.31 |

Table 7.1 Valence states of the indicated Fe (left of slash) and distances (Å) from the Fe to PO₄ vacancy center (right of slash) of in optimized structures of pristine and PO₄-deficient FePO₄ under various charge states.

To better understand the defect-induced changes on the bonding environment, we examined the structures for $V_{PO_4}^q$ of different charge states (*q*). For *q* = 1−, 0, 1+ and 2+,

the variations in Fe valence state and distances from Fe to the vacancy center ($\text{Fe}-V_{\text{PO}_4}$) are summarized in Table 7.1, together with values from the pristine case for comparison. In neutral state, due to the aforementioned charge localization, the neighboring three Fe atoms (a, c and d) are reduced to Fe^{2+} . The local lattice surrounding $V_{\text{PO}_4}^0$ exhibits an outward expansion, and the adjacent P_1 atom is displaced slightly in [010] direction towards $V_{\text{PO}_4}^0$; consequently, the $\text{P}_1\text{-Fe}$ distance increases from 3.22 Å (in the pristine case) to 4.08 Å. It is worth noting that the $V_{\text{PO}_4}^0$ -induced lattice distortion appears to be asymmetrical with respect to the (010) plane spanned by Fe (a, d and e) as the $V_{\text{PO}_4}^0 - \text{Fe}_b$ and $V_{\text{PO}_4}^0 - \text{Fe}_c$ distances are different (3.34 and 3.46 Å, respectively). The slight deviation from symmetry is likely attributed to the unequal charge redistribution among the five Fe ions adjacent to $V_{\text{PO}_4}^0$, resulting in their differences in charge state and bond environment. For $V_{\text{PO}_4}^+$, with the additional hole, one of the three Fe^{2+} ions in $V_{\text{PO}_4}^0$ is oxidized to Fe_c^{3+} . The lattice distortion becomes symmetrical as two Fe ions (b and d) locating on the positive sides of the (010) plane have the same charge state (3+); in addition, we also found the displacement of the adjacent P atom to be much smaller if the lattice distortion was symmetrical. For $V_{\text{PO}_4}^-$, the additional electron tends to localize on Fe, and the lattice distortion is asymmetrical. For $V_{\text{PO}_4}^{2-}$, with the additional two electrons, all five Fe^{3+} ions surrounding the PO_4 vacancy are reduced to Fe^{2+} , thus the symmetric configuration is restored, and the P-Fe (I) distance of 3.31 Å is very close to the pristine case (3.22 Å).

7.3.3 Relative Stability of Defected FePO₄ in Various Charged States

Figure 7.4 shows the relative formation energy of $V_{PO_4}^+$, $V_{PO_4}^-$ and $V_{PO_4}^{2-}$ with respect to $V_{PO_4}^0$, which is calculated by

$$E^f(V_{PO_4}^q) = E_{tot}(V_{PO_4}^q) - E_{tot}(V_{PO_4}^0) + q(E_v + \varepsilon_F) \quad (7.3.1)$$

where E_{tot} is the total energy of the supercell, q is the charge state, E_v is valence band maximum (VBM), and ε_F is the Fermi level. In the periodic approach, a homogeneous background charge is included to maintain the overall charge neutrality of a charged supercell. To account for the electrostatic interaction with the background charge, a monopole correction was made to the total energy of the charged system.¹⁶⁹ For a point-like charge in the 144-atom FePO₄ supercell, the monopole correction is estimated to be smaller than 0.1 eV, which is reasonable given the considerably large dielectric constant of 17.5¹⁷⁰. Our calculation predicts the relative formation energies of $V_{PO_4}^+$, $V_{PO_4}^-$ and $V_{PO_4}^{2-}$ to be -0.77, 0.76 and 1.83 eV at the VBM, respectively. Given the calculated FePO₄ bandgap around 1.75 eV, the first donor (+/ 0) and acceptor (0/ -), and the second acceptor levels (-/ 2-) are predicted to be 0.7, 0.87, and 1.08 eV, respectively. At the midgap ($\varepsilon_F \approx 0.88$ eV), $V_{PO_4}^-$ has the lowest formation energy around -0.15 eV, suggesting that $V_{PO_4}^0$ may easily accommodate an additional electron under the intrinsic condition;

considering their small formation energy difference, $V_{PO_4}^0$ and $V_{PO_4}^-$ may coexist in the matrix.

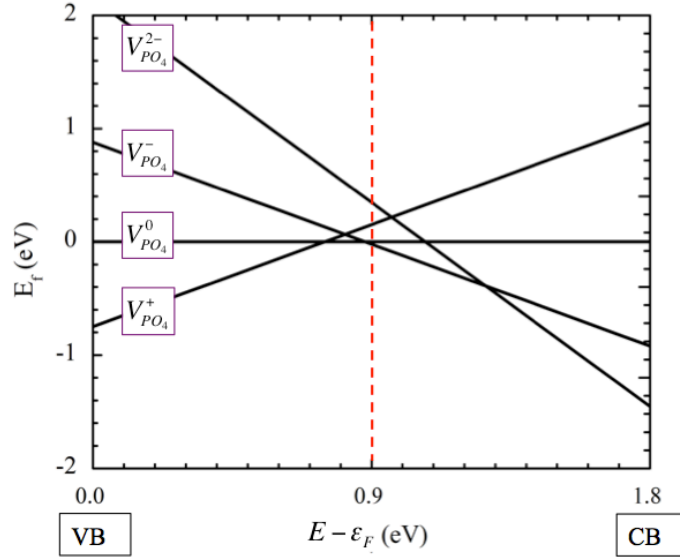
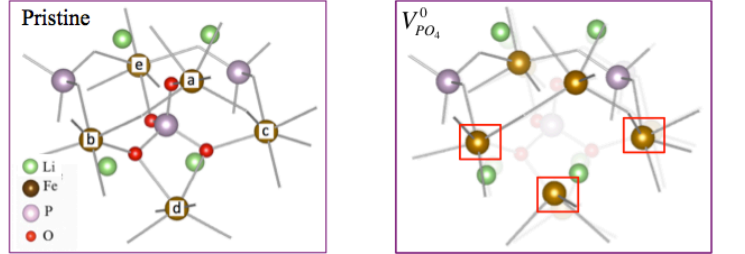


Figure 7.4 Variation in the relative formation energy of PO₄-deficient FePO₄ in different charge states with respect to as a function of the Fermi level relative to the valence band maximum (E_v) for the computed FePO₄ bandgap around 1.75 eV.

7.3.4 PO₄-deficient LiFePO₄ Structure

The PO₄-deficient LFP structure considered in this work was created by removing a PO₄ unit from a periodic 168-atom supercell containing 24 PO₄ units, corresponding to 4 at.% PO₄-vacancy. The creation of a neutral PO₄-vacancy (V_{PO_4}) leaves three unpaired electrons, which are predicted to localize on three of the five adjacent Fe ions as confirmed by the DOS and band-decomposed charge density analysis.



| | $V_{PO_4}^q$ | Fe_a^q | Fe_b^q | Fe_c^q | Fe_d^q | Fe_e^q |
|----------|--------------|-----------|-----------|-----------|-----------|-----------|
| Pristine | | 2+ / 3.29 | 2+ / 3.32 | 2+ / 3.32 | 2+ / 2.87 | 2+ / 3.31 |
| 0 | | 2+ / 3.35 | 1+ / 3.11 | 1+ / 3.17 | 1+ / 2.28 | 2+ / 3.49 |
| +1 | | 2+ / 3.37 | 1+ / 3.09 | 2+ / 3.45 | 1+ / 2.49 | 2+ / 3.47 |
| +2 | | 2+ / 3.42 | 2+ / 3.44 | 2+ / 3.44 | 1+ / 2.78 | 2+ / 3.49 |
| +3 | | 2+ / 3.45 | 2+ / 3.52 | 2+ / 3.52 | 2+ / 3.21 | 2+ / 3.53 |

Table 7.2 Valence states of the indicated Fe (left of slash) and distances (Å) from the Fe to PO_4 vacancy center (right of slash) of in optimized structures of pristine and PO_4 -deficient $LiFePO_4$ under various charge states.

Table 7.2 summarizes the variations in Fe valence state and distances from Fe to the vacancy center ($Fe-V_{PO_4}^q$) with $q = 0, 1+, 2+$ and $3+$, together with values from the pristine case for comparison. While all Fe ions are 2+ in pristine LFP, three of the Fe ions adjacent to $V_{PO_4}^0$ are oxidized to 1+, which in turn reduces the (i) Coulomb repulsion between Fe ions, and the (ii) Coulomb attraction between Fe ions and neighboring $(PO_4)^{3-}$ polyanions. Consequently, the $Fe-V_{PO_4}$ distances are shortened in comparison to the pristine case, leading to inward displacements of Fe^+ towards $V_{PO_4}^0$. Following this rational, the local structure is affected by the intricate interplay between aforementioned

Coulomb interactions. The adjacent Fe ions then exhibit inward or outward displacements depending on the excess electron distribution pertains to $V_{PO_4}^q$ of specific charges.

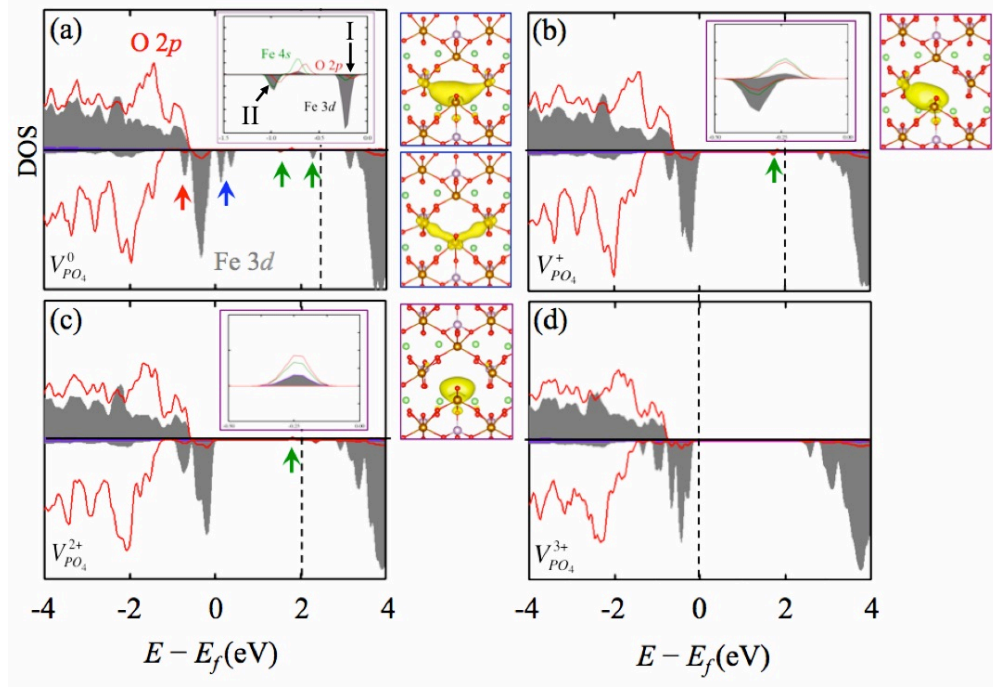


Figure 7.5 The DOS of PO_4 -deficient $LiFePO_4$ in charge state (a) neutral, (b) 1+, (c) 2+ and (d) 3+, respectively. The insets are enlarged DOS detail of localized states indicated by green arrow. The band-decomposed charge densities corresponding to those localized states are plotted with an isosurface value of $0.01 \text{ electron}/\text{\AA}^3$.

Figure 7.5 shows the DOS projected onto Fe, P and O atoms in PO_4 -deficient LFP of different charge states, together with the band-decomposed charge density plots shown in the insets (on the right). For $V_{PO_4}^0$ [Fig. 7.5 (a)], two distinct defect states are found within the band gap; one defect level (indicated as I) lies right below the conduction band (CB), and the other (indicated as II) is around the middle of the gap. The defect state I is mainly composed of Fe_b and Fe_c 3d while state II shows some overlap between Fe_d 3d

and 4s, and O 2p (as also demonstrated by the band-decomposed charge density plots). This suggests the excess electrons are highly localized, such that the three Fe ions (b, c and d) are reduced to Fe⁺ as mentioned before, and the small degree of charge spreading to neighboring O atoms is likely due to the lattice distortion around $V_{PO_4}^0$. Furthermore, we see that at the top of the valence band (VB), Fe 3d states are split into three distinct peaks. The blue arrow indicates the two peaks from Fe⁺ 3d, which are destabilized by the increasing repulsive force from Fe⁺–O²⁻ antibonding states due to additional valence electrons from $V_{PO_4}^0$, and thus the upshift in energy. On the other hand, the two peaks from two undercoordinated Fe²⁺ ions (indicated by the red arrow) become relatively more stable (downshift in energy) due to the polyanion removal reduces the overlap between Fe²⁺ 3d and O²⁻ 2p states. As $V_{PO_4}^q$ becomes more positively charged [Fig. 7.5 (b-d)], the number of defect states within the gap decreases, and with each undercoordinated Fe⁺ oxidized to Fe²⁺, the Fe 3d at the top of VB tends to be further stabilized and shifts down in energy.

7.3.5 Relative Stability of PO₄-defected LiFePO₄ in Various Charged States

To understand the stability of LFP matrix with electrons left by PO₄-vacancy, we calculated the relative formation energy of $V_{PO_4}^q$ with $q = 0$ to 4+ by Eq. 1, as shown in Fig. 7.6. In the periodic approach, a homogeneous background charge is included to maintain the overall charge neutrality of a charged supercell. For a point-like charge in

the 168-atom LFP supercell, the monopole correction is estimated to be smaller than 0.1 eV, which is the same value to aforementioned 144-atom FP and reasonable given the considerably large dielectric constant of 19.8¹⁷.

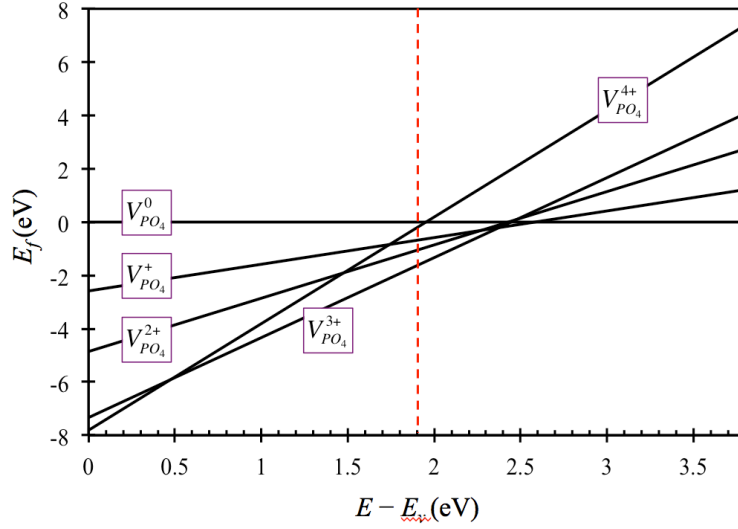


Figure 7.6 Variation in the relative formation energy of PO_4 -deficient $LiFePO_4$ in different charge states with respect to as a function of the Fermi level relative to the valence band maximum (E_v) for the computed $LiFePO_4$ bandgap around 3.8 eV.

Our calculation predicts the relative formation energies of $V_{PO_4}^{4+}$, $V_{PO_4}^{3+}$, $V_{PO_4}^{2+}$ and $V_{PO_4}^+$ to be -7.9, -7.3, -4.8 and -2.6 eV at the VBM, respectively. Given the calculated $LiFePO_4$ bandgap around 3.8 eV, the first (+/ 0), second (2+/ +) and third (3+/ 2+) donor levels are predicted to be 2.55, 2.35 and 0.5 eV, respectively. At the middle gap ($\epsilon_F \approx 1.9$ eV), $V_{PO_4}^{3+}$ has the lowest formation energy around -2.1 eV, suggesting that the PO_4 -deficient LFP matrix can easily lose three electrons.

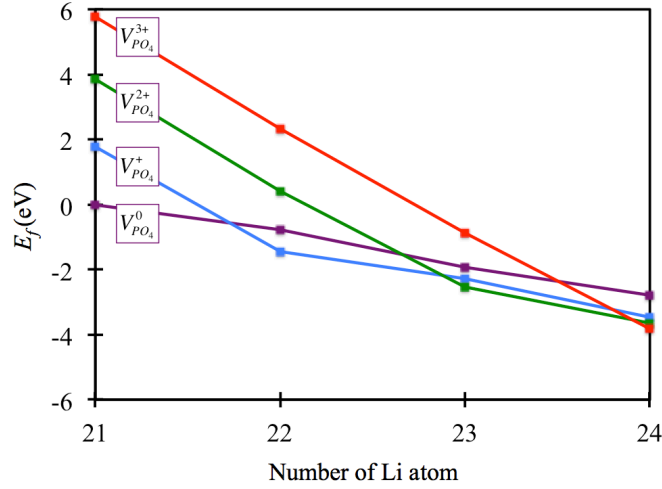


Figure 7.7 The relative formation energy of PO_4 -deficient $LiFePO_4$ with $q = 0$ to $4+$ as a function of Li content (x) in the $Li_xFe_N(PO_4)_{N-1}$ supercell ($N = 24$) with respect to the $x = N-3$ neutral case ($q = 0$).

Previously, we predicted $V_{PO_4}^0$ to be the most favorable charge state in FP.¹⁷¹

Interestingly, in the case of LFP, $V_{PO_4}^{3+}$ appears to be the most favorable, indicating the relative stability of $V_{PO_4}^q$ varies depending on the Li content. That is, while the stability of $V_{PO_4}^q$ is presumably related to the Fe^{2+}/Fe^+ oxidation-reduction (redox) reaction governed by changes in stoichiometry ($Li_NFe_N(PO_4)_N \rightarrow Li_NFe_N(PO_4)_{N-1}$), variations in Li content would influence the Fe oxidation and thereby affect the stability. Figure 7.7 shows the relative formation energy $E_f(x)$ of $V_{PO_4}^q$ ($q = 0$ to $4+$) as a function of Li content (x) in the $Li_xFe_N(PO_4)_{N-1}$ supercell ($N = 24$) with respect to the $x = N-3$ neutral case ($q = 0$). Here, we re-define the formation energy as

$$E_f(x) = [E_{tot}(V_x^0) + E^f(V_x^q)] - [E_{tot}(V_{N-3}^0) + (x - N + 3)E_{tot}(Li)] \quad (7.3.2)$$

where $E_{tot}(V_x^q)$ is the total energy of PO_4 -deficient supercell with q and x denoting the charge state and Li content, respectively, $E^f(V_x^q)$ is the formation energy defined earlier in Eq. 7.3.1 where x equals to N , and $E_{tot}(\text{Li})$ is the per-atom energy of body-centered-cubic (*bcc*) Li metal.

In the case of $x \leq N-3$, the system would always be most stable under neutral charge state since the formation of $V_{\text{PO}_4}^0$ only results in $\text{Fe}^{3+} \rightarrow \text{Fe}^{2+}$ reductions. As x increases from $N-2$ to N , $E_f(x)$ of neutral states are predicted to be negative and continue to decrease in value with respect to the $x = N-3$ case, suggesting the PO_4 -deficient supercell remains stable approaching the fully lithiated composition ($x = N = 24$). Moreover, we find that the PO_4 -deficient matrix of varying Li contents can be further stabilized via $\text{Fe}^+ \rightarrow \text{Fe}^{2+}$ oxidation, such that for $x = N-2$ and $N-1$, $q = 2+$ and $1+$ are the most stable charge states, respectively. For the fully lithiated case ($x = N$), $q = 3+$ is predicted to be most energetically favorable as aforementioned. These results suggest that PO_4 -polyanion deficient matrices would be stable in all Li composition range up till the fully lithiated phase ($x = N = 24$), and the stability would be further enhanced if the system were positively charged. In either case, the lithiation capacity of LFP is not compromised via the creation of the PO_4 polyanion vacancies.

7.3.6 Mechanical Properties

Finally, we looked at how the PO₄ deficiency affects the mechanical properties. Here we only considered the bulk modulus (B) which can be estimated by fitting the Murnaghan equation of state¹⁷² to the corresponding energy versus volume curve. Uniform tensile and compressive strains were imposed on the pristine, neutral ($V_{PO_4}^0$) PO₄-deficient FP and triply positive charged ($V_{PO_4}^{3+}$) PO₄-deficient LFP structures to achieve $\pm 0.66 - 1$ % volume changes.

$$E(V) = E_0 + \left(\frac{BV}{B'} \right) \left[\frac{(V_0/V)^{B'}}{B'-1} + 1 \right] - \frac{V_0 B}{B'-1} \quad (7.3.3)$$

where E and E_0 refer to the total energies of pristine and PO₄-deficient FP/LFP at volume V and V_0 (equilibrium), respectively, and B' is the pressure derivative of the bulk modulus; here, we increased the cut-off energy to 550-600 eV and force tolerance to 0.01 eV/Å to refine energy variations with applied strain. While the predicted B values of 68.1 (96.1) GPa for pristine FP (LFP) is in close agreement with previous theoretical results of 73.6 (94.7) GPa,¹⁷³ our calculations show a 20% (8.8%) reduction in B of 53.2 (87.6) GPa with only 4.2 at.% PO₄-vacancy in the matrix. These results suggest that both lithiated and delithiated FePO₄ can be significantly softened by the presence of PO₄ deficiency. We anticipate the softer/more flexible matrixes can in turn enhance the strain accommodation capability during cycling and thereby improve the cathode. Based on the aforementioned results of fundamental properties of PO₄-deficient LFP/FP, we will

examine the influence on lithiation process from the formation of PO_4 -vacancy, and search for potential improvements on this cathode material.

7.4 SUMMARY

Spin-polarized DFT+U calculations were performed to investigate the structures and properties of PO_4 -deficient FePO_4 and LiFePO_4 at various charge states ($V_{\text{PO}_4}^q$). Our calculation shows the PO_4 -deficient FePO_4 structure has a limited distortion under the presence of V_{PO_4} . The excess electrons from V_{PO_4} was predicted to be localized on Fe which have broken bonds near the vacancy and stabilize the structure. The additional electrons and holes added in the matrix were also predicted to have similar tendency. The formation energy of $V_{\text{PO}_4}^q$ with different charged states (q) were then calculated. The results show the first donor (+/ 0) and acceptor (0/ -), and the second acceptor levels (-/ 2-) are predicted to be ranged from 0.7 to 1.08 eV, which suggests $V_{\text{PO}_4}^q$ can be stabilized with q equals to +1, 0, -1 in the matrix.

In the PO_4 -deficient LiFePO_4 , three electrons left by one PO_4 removal ($V_{\text{PO}_4}^0$) are predicted localized on three Fe^+ ions adjacent to the vacancy. The reduction of Fe^{2+} ions to Fe^+ lowers the attractive Coulomb force between the Fe^+ ions and surrounding $(\text{PO}_4)^{3-}$ polyanions, leading to inward displacement of Fe ions to the vacancy center. The DOS analysis illustrates a series of non-bonding states below the CB, which are related to the presence of $V_{\text{PO}_4}^0$. First of all, localized Fe^+ 3d states consist of the unpaired electrons

from creating $V_{PO_4}^0$ are predicted in the gap. Below that, certain valence states of Fe^+ are found shift to higher energies as being destabilized by the unpaired electrons. Meanwhile, valence states of two Fe^{2+} ions adjacent to the vacancy shift to lower energies, which are attributed to the stabilization of Fe – O antibonding states due to the decrease of overlap between $Fe^{2+} 3d$ and $O^{2-} 2p$ states. According to the relative formation energies for various charge states, $V_{PO_4}^{3+}$ is predicted to be the most energetically favorable. For $q = 3+$, three aforementioned Fe^+ ions in $V_{PO_4}^0$ case are oxidized to Fe^{2+} . Thus, no high-energy localized state is predicted in the gap. It is worth mentioning that the reduction reaction of $Fe^+ \rightarrow Fe^{2+}$ increases the attractive (repulsive) force to the surrounding $(PO_4)^{3-}$ polyanions (Li^+ cations) near the vacancy, resulting in an outward relaxation.

Our calculations show that, for $Li_xFe_N(PO_4)_{N-1}$, the most stable charge state is predicted to be $q = 0, 1+, 2+, \text{ and } 3+$ with $x = N-3, N-2, N-1$ and N , respectively. Therefore, the capacity of PO_4 -deficient $LiFePO_4$ as a cathode is not influenced by the excess charges in the matrix as the most energetically favorable charge states change during the lithiation process. Finally, we calculated the bulk modulus (B) of both $FePO_4$ and $LiFePO_4$ structures with and without the presence of V_{PO_4} vacancy. Our calculations show a 20% (8.8%) reduction in the bulk modulus of $FePO_4$ and $LiFePO_4$, respectively, with only 4.2 at.% PO_4 -vacnacy in the matrix. These results suggest that both lithiated and delithiated $FePO_4$ can be significantly softened by the presence of PO_4 deficiency. We anticipate the softened matrices could enhance the strain accommodation capability during cycling and improve the cathode performance. These fundamental findings

suggest the performance of the LFP cathode for Li-ion batteries can be engineered through creation of PO_4 polyanion vacancies, which may increase the electrical conductivity as well as Li^+ ion diffusivity.

References

- ¹ IPCC. *Climate Change 2014: Synthesis Report. Contribution of Working Groups I, II and III to the Fifth Assessment Report of the Intergovernmental Panel on Climate Change*; Geneva, Switzerland (2014)
- ² D.M. D'Alessandro, B. Smit, and J.R. Long, *Angew. Chem. Int. Ed. Engl.*, **49**, 6058 (2010)
- ³ U.S. Energy Information Agency. *International Energy Outlook 2013*; Washington, DC (2013)
- ⁴ C.N.R. Rao, *Annu. Rev. Phys. Chem.*, **40**, 291 (1989)
- ⁵ M.Z. Born, *Physik*, **37**, 863 (1926)
- ⁶ M. Born, and R. Oppenheimer, *Annalen der Physik*, **389**, 457 (1927)
- ⁷ M. Springborg, *Methods of Electronic Structure Calculations: From molecules to solids* [Wiley, New York, New York] (2000)
- ⁸ J. Slater, and H.C. Verma, *Physical Review.*, **34**, 1293 (1929)
- ⁹ P. Hohenberg, and W. Kohn, *Phys. Rev.*, **136**, B864 (1964)
- ¹⁰ R.M. Martin, *Electronic Structure: Basic Theory and Practical Methods* [Cambridge University Press] (2004).
- ¹¹ W. Kohn, and L.J. Sham, *Phys. Rev.*, **140**, A1133 (1965)
- ¹² J.P. Perdew, and K. Burke, *Int. J. Quantum Chem.*, **57**, 309 (1996)
- ¹³ J.P. Perdew, and Y. Wang, *Phys. Rev. B.*, **33**, 8800 (1986)
- ¹⁴ J.P. Perdew, *Electronic Structure of Solids '91* (edited by P. Ziesche, and H. Eschrig, Akademie Verlag, 1991, 11).
- ¹⁵ J.P. Perdew, K. Burke, and M. Ernzerhof, *Phys. Rev. Lett.*, **77**, 3865 (1996)
- ¹⁶ J.P. Perdew, K. Burke, and M. Ernzerhof, *Phys. Rev. Lett.*, **78**, 1396 (1997)
- ¹⁷ A. Krashenninnikov, *Introduction to electronic structure simulations – Lecture 8* [University of Helsinki and Helsinki University of Technology] (2006)
- ¹⁸ D.R. Hamann, M. Schlueter, and C. Chiang, *Phys. Rev. Lett.*, **43**, 1494 (1979)
- ¹⁹ D. Vanderbilt, *Phys. Rev. B*, **41**, 7892 (1990)
- ²⁰ K.P. Kuhl, T. Hatsukade, E.R. Cave, D.N. Abram, J. Kibsgaard, and T.F. Jaramillo, *J. Am. Chem. Soc.*, **136**, 14107–14113 (2014)
- ²¹ X. Chang, T. Wang, and J. Gong, *Energy Environ. Sci.*, **9**, 2177 (2016)
- ²² International Journal of Hydrogen Energy Volume 11, Issue 5, 1986, Pages 341-347
- ²³ M. Jitaru, D.A. Lowry, M. Toma, B.C. Toma, L. Oniciu, *J. Appl. Electrochem.*, **27**, 875 (1997)
- ²⁴ R.P.S Chaplin, A.A. Wragg, *J. Appl. Electrochem.*, **33**, 1107 (2003)
- ²⁵ Y. Chen, M.W. Kanan, *J. Am. Chem. Soc.*, **134**, 1986 (2012)
- ²⁶ Z.M. Detweiler, J.L. White, S.L. Bernasek, A.B. Bocarsly, *Langmuir*, **30**, 7593 (2014)
- ²⁷ Y. Hori, K. Kikuchi, S. Suzuki, *Chem. Lett.*, 1695 (1985)
- ²⁸ S. Ma, P. J. Kenis, *Curr. Opin. Chem. Eng.*, **2**, 191 (2013)
- ²⁹ C.W. Li, and M.W. Kanan, *J. Am. Chem. Soc.*, **134**, 7231 (2012)

- ³⁰ U. Kang, S.K. Choi, D.J. Ham, S.M. Ji, W. Choi, D.S. Han, A. Abdel-Wahab and, H. Park, *Energy Environ. Sci.*, **8**, 2638 (2015)
- ³¹ U. Kang, and H. Park, *J. Mater. Chem. A*, **5**, 2123 (2017)
- ³² G. Kresse, and J. Furthmüller, *Comput. Mat. Sci.*, **6**, 15 (1996)
- ³³ G. Kresse, and J. Furthmüller, *Phys. Rev. B*, **54**, 11169 (1996)
- ³⁴ P.E. Blochl, *Phys. Rev. B*, **50**, 17953 (1994)
- ³⁵ G. Kresse, and D. Joubert, *Phys. Rev. B*, **59**, 1758 (1999)
- ³⁶ C.E. Ekuma, V.I. Anisimov, J. Moreno, and M. Jarrell, *Eur. Phys. J. B*, **87**, 23 (2014)
- ³⁷ J. Heyd, G. E. Scuseria, and M. Ernzerhof, *J. Chem. Phys.*, **118**, 8207 (2003).
- ³⁸ H.J. Monkhorst, and J.D. Pack, *Phys. Rev. B*, **13**, 5188 (1976)
- ³⁹ K. Mathew, R. Sundararaman, K. Letchworth-Weaver, T. A. Arias, and R. G. Hennig, *J. Chem. Phys.*, **140**, 084106 (2014)
- ⁴⁰ A.P. Moura, L.S. Cavalcante, J.C. Sczancoski, D.G. Stroppa, E.C. Paris, A.J. Ramirez, J.A. Varela, E. Longo, *Adv. Powder Techno.*, **21**, 197 (2010)
- ⁴¹ A.K. Mishra, A. Roldan, and N.H. Leeuw, *J. Phys. Chem. C*, **120**, 2198 (2015)
- ⁴² A. Filippetti, *Phys. Rev. Lett.*, **95**, 086405 (2005)
- ⁴³ A.K. Mishra, A. Roldan, and N.H. Leeuw, *J. Phys. Chem. C*, **120**, 2198 (2015)
- ⁴⁴ Y. Maimaiti, M. Nolan, and S.D. Elliott, *Phys. Chem. Chem. Phys.*, **16**, 3036 (2014)
- ⁴⁵ A.E. Rakhshani, *Solid State Electron.*, **29**, 7 (1986)
- ⁴⁶ S.C. Ray, *Sol. Energy Mater. Sol. Cells*, **68**, 307 (2001)
- ⁴⁷ K.L. Hardee, and A.J. Bard, *J. Electrochem. Soc.*, **124**, 215-224 (1977)
- ⁴⁸ J. Ghijsen, L.H. Tjeng, J. van Elp, H. Eskes, J. Westerink, G.A. Sawatzky, and M.T. Czyzyk, *Phys. Rev. B*, **38**, 11322 (1988)
- ⁴⁹ H.T. Hsueh, S.J. Chang, F.Y. Hung, W.Y. Weng, C.L. Hsu, T.J. Hsueh, S.S. Lin and B.T. Dai, *J. Electrochem. Soc.*, **158**, J106 (2011)
- ⁵⁰ X. Jiang, T. Herricks, and Y. Xia, *Nano Lett.*, **2**, 1333 (2002)
- ⁵¹ J. Hu, D. Li, J.G. Lu, and R.Wu, *J. Phys. Chem. C*, **114**, 17120 (2010)
- ⁵² A.K. Mishra, A. Roldan, and N.H. Leeuw, *J. Phys. Chem. C*, **120**, 2198 (2015)
- ⁵³ Y. Maimaiti, M. Nolan, S.D. Elliott, *Phys. Chem. Chem. Phys.*, **16**, 3036 (2014)
- ⁵⁴ J. Zhang, R. Zhang, B. Wang, and L. Ling, *Appl. Surf. Sci.*, **364**, 758 (2016)
- ⁵⁵ S. Warren, W.R. Flavell, A.G. Thomas, J. Hollingworth, P.M. Dunwoody, S. Downes, and C. Chen, *Surf. Sci.*, **436**, 1, (1999)
- ⁵⁶ Z. Chang, T. Wang, and J. Gong, *Energy Environ. Sci.*, **9**, 2177 (2016)
- ⁵⁷ E.L. Uzunova, N. Seriani, and H. Mikosch, *Phys. Chem. Chem. Phys.*, **17**, 11088 (2015)
- ⁵⁸ A.A. Peterson, F. Abild-Pedersen, F. Studt, J. Rossmeisl, and J.K. Nørskov, *Energy Environ. Sci.*, **3**, 1311 (2010)
- ⁵⁹ T. Cheng, H. Xiao, and W.A. Goddard III, *J. Am. Chem. Soc.*, **138**, 13802 (2016)
- ⁶⁰ K.P. Kuhl, E.R. Cave, D.N. Abram, and T.F. Jaramillo, *Energy Environ. Sci.*, **5**, 7050 (2012)
- ⁶¹ G. Kovács, G. Schubert, F. Joó, I. Pápai, *Catal. Today*, **115**, 53 (2006)

- ⁶² U. Kang, S.K. Choi, D.J. Ham, S.M. Ji, W. Choi, D. S. Han, A. Abdel-Wahabe, and H. Park, *Energy Environ. Sci.*, **8**, 2638-2643 (2015)
- ⁶³ R. Kortlever, J. Shen, K.J.P. Schouten, F. Calle-Vallejo, and M.T.M. Koper, *J. Phys. Chem. Lett.*, **6**, 4073 (2015)
- ⁶⁴ Y. Lan, S. Ma, J. Lu, and P.J.A. Kenis, *Int. J. Electrochem. Sci.*, **9**, 7300 (2014)
- ⁶⁵ A.A. Peterson, and J.K. Nørskov, *J. Phys. Chem. Lett.*, **3**, 251 (2012)
- ⁶⁶ M. Gattrell, N. Gupta, and A. Co, *J. Electroanal. Chem.*, **594**, 1 (2006)
- ⁶⁷ S. Fierro, T. Nagel, H. Baltruschat, and C. Comninellis, *Electrochem. Commun.*, **9**, 1969 (2007)
- ⁶⁸ K. Macounova, M. Makarova, and P. Krtil, *Electrochem. Commun.*, **11**, 1865 (2009)
- ⁶⁹ M. Wohlfahrt-Mehrens, and J. Heitbaum, *J. Electroanal. Chem. Interf. Electrochem.*, **237**, 251 (1987).
- ⁷⁰ T. Reier, M. Oezaslan, and P. Strasser, *ACS Catal.*, **2**, 1765 (2012)
- ⁷¹ R.B. Gordon, M. Bertram, and T.E. Graedel, *Proc. Natl Acad. Sci.*, **103**, 1209 (2006)
- ⁷² V. Augustyn, and A. Manthiram, *Chem Plus Chem.*, **80**, 422 (2015)
- ⁷³ S.W. Lee, C. Carlton, M. Risch, Y. Surendranath, S. Chen, S. Furutsuki, A. Yamada, D.G. Nocera, and Y. Shao-Horn, *J. Am. Chem. Soc.*, **134**, 16959 (2012)
- ⁷⁴ T. Maiyalagan, K.A. Jarvis, S. Therese, P.J. Ferreira, and A. Manthiram, *Nat. Commun.*, **5**, 3949 (2014)
- ⁷⁵ Y. Liang, Y. Li, H. Wang, J. Zhou, J. Wang, T. Regier, and H. Dai, *Nat. Mater.*, **10**, 780 (2011)
- ⁷⁶ Z. Lu, H. Wang, D. Kong, K. Yan, P.-C. Hsu, G. Zheng, H. Yao, Z. Liang, X. Sun, and Y. Cui, *Nat. Commun.*, **5**, 4345 (2014)
- ⁷⁷ L. Wang, F. Zhou, Y.S. Meng, and G. Ceder, *Phys. Rev. B*, **76**, 1 (2007)
- ⁷⁸ N. Colligan, V. Augustyn, and A. Manthiram, *J. Phys. Chem. C.*, **119**, pp 2335–2340 (2015)
- ⁷⁹ S. Venkatraman, and A. Manthiram, *J. Solid State Chem.*, **177**, 4244 (2004)
- ⁸⁰ T.W. Kim, E.-J. Oh, A.-Y. Jee, S.T. Lim, D.H. Park, M. Lee, S.-H. Hyun, J.-H. Choy, and S.-J. Hwang, *Chem. Eur. J.*, **15**, 10752 (2009)
- ⁸¹ R. Benedek, M.M. Thackeray, and A. van de Walle, *Chem. Mater.*, **20**, 5485 (2008)
- ⁸² R.J. Gummow, D.C. Liles, and M.M. Thackeray, *Mat. Res. Bull.*, **28**, 235 (1993)
- ⁸³ F. Zhou, M. Cococcioni, C.A. Marianetti, D. Morgan, and G. Ceder, *Phys. Rev. B.*, **70**, 235121 (2004)
- ⁸⁴ J. Heyd, G.E. Scuseria, and M. Ernzerhof, *J. Chem. Phys.* **118**, 8207 (2003).
- ⁸⁵ S. van Smaalen, R. Dinnebier, M. Sofin, and M. Jansen, *Acta Crystallogr. B*, **63**, 17 (2007).
- ⁸⁶ D.F. Xue, S. Zuo, H. Ratajczak, *Physica B*, **352**, 99 (2004)
- ⁸⁷ R.Q. Albuquerque, G.B. Rocha, O.L. Malta, P. Porcher, *Chem. Phys. Lett.*, **331**, 519 (2000)
- ⁸⁸ M. Antaya, K. Cearns, J. S. Preston, J. N. Reimers, and J. R. Dahn, *J. Appl. Phys.*, **76**, 2799 (1994)
- ⁸⁹ J.M. Rosolen, *J. Electroanal. Chem.*, **501**, 253 (2001)

- ⁹⁰ J. van Elp, J. L. Wieland, H. Eskes, P. Kuiper, G.A. Sawatzky, F.M.F. de Groot, and T.S. Turner, *Phys. Rev. B*, **44**, 6090, (1991)
- ⁹¹ S. Laubach, S. Laubach, P.C. Schmidt, D. Ensling, S. Schmid, and W. Jaegermann, *Phys. Chem. Chem. Phys.*, **11**, 3278 (2009)
- ⁹² A. Van der Ven, and G. Ceder, *Phys. Rev. B*, **59**, 742 (1999)
- ⁹³ J.R. Dahn, E.W. Fuller, M. Obrovac, and U. von Sacken, *Solid State Ionics*, **69**, 265 (1994)
- ⁹⁴ R. Hausbrand, D. Becker, and W. Jaegermann, *Prog. Solid State Ch.*, **42**, 175 (2014)
- ⁹⁵ M. Motzko, M.A. Carrillo Solano, W. Jaegermann, and R. Hausbrand, *J. Phys. Chem. C*, **119**, 23407 (2015)
- ⁹⁶ T. Ikeda, *J. Chem. Phys.*, **126**, 034501 (2007)
- ⁹⁷ J.-H. Shim, K.-S. Lee, A. Missyul, J. Lee, B. Linn, E.C. Lee, and S. Lee, *Chem. Mater.*, **27**, 3273 (2015)
- ⁹⁸ B.J. Morgan, and G.W. Watson, *J. Phys. Chem. C*, **113**, 7322 (2009)
- ⁹⁹ H. Li, Y. Guo, and J. Robertson, *J. Phys. Chem. C*, **119**, 18160 (2015)
- ¹⁰⁰ B. Bharti, S. Kumar, H.-No. Lee, and R. Kumar, *Sci. Rep.*, **6**, 32355 (2016)
- ¹⁰¹ X. Pan, M.-Q. Yang, X. Fu, N. Zhang, and Y.-J. Xu, *Nanoscale*, **5**, 3601 (2013)
- ¹⁰² S. Levasseur, M. Ménétrier, Y. Shao-Horn, L. Gautier, A. Audemer, G. Demazeau, A. Largeteau, and C. Delmas, *Chem. Mater.*, **15**, 348 (2003)
- ¹⁰³ L. Dahéron, H. Martinez, R. Dedryvère, I. Baraille, M. Ménétrier, C. Denage, C. Delmas, and D. Gonbeau, *J. Phys. Chem. C*, **113**, 5843 (2009)
- ¹⁰⁴ S. Wendt, R. Schaub, J. Matthiesen, E.K. Vestergaard, E. Wahlström, M.D. Rasmussen, P. Thstrup, L.M. Molina, E. Lægsgaard, I. Stensgaard, B. Hammer, and F. Besenbacher, *Surf. Sci.*, **598**, 226 (2005)
- ¹⁰⁵ Z. Zhou, Y. Zhang, Z. Wang, W. Wei, W. Tang, J. Shi, and R. Xiong, *Appl. Surf. Sci.*, **254**, 6972 (2008)
- ¹⁰⁶ D.R. Lide Jr., and R.L. Kuczkowski, *J. Chem. Phys.*, **46**, 4768 (1967)
- ¹⁰⁷ S. Fierro, T. Nagel, H. Baltruschat, and C. Comninellis, *Electrochem. Commun.*, **9**, 1969 (2007)
- ¹⁰⁸ K. Macounova, M. Makarova, and P. Krtil, *Electrochem. Commun.*, **11**, 1865 (2009)
- ¹⁰⁹ M. Wohlfahrt-Mehrens, and J. Heitbaum, *J. Electroanal. Chem. Interf. Electrochem.*, **237**, 251 (1987)
- ¹¹⁰ T. Reier, M. Oezaslan, and P. Strasser, *ACS Catal.*, **2**, 1765 (2012)
- ¹¹¹ J. Suntivich, K.J. May, H.A. Gasteiger, J.B. Goodenough, and Y. Shao-Horn, *Science*, **334**, 1383 (2011)
- ¹¹² M. García-Mota, A. Vojvodic, H. Metiu, I.C. Man, H.-Y. Su, J. Rossmeisl, and J.K. Nørskov, *Chem. Cat. Chem.*, **3**, 1607 (2011)
- ¹¹³ M.H. Seo, H.W. Park, D.U. Lee, M.G. Park, and Z. Chen, *ACS Catal.*, **5**, 4337 (2015)
- ¹¹⁴ H. Kim, J. Park, I. Park, K. Jin, S.E. Jerng, S.H. Kim, K.T. Nam, and K. Kang, *Nat. Commun.*, **6**, 8253 (2015)
- ¹¹⁵ M.S. Burke, L.J. Enman, A.S. Batchellor, S. Zou, and S.W. Boettcher, *Chem. Mater.*, **27**, 7549 (2015)

- ¹¹⁶ F. Dionigi, and P. Strasser, *Adv. Energy Mater.*, **6**, 1600621 (2016)
- ¹¹⁷ K. Mathew, R. Sundararaman, K. Letchworth-Weaver, T. A. Arias, and R. G. Hennig, *J. Chem. Phys.*, **140**, 084106 (2014)
- ¹¹⁸ J. Bonion, C. Costentin, M. Robert, J.-M. Saveant, and C. Tard, *Accounts Chem. Res.*, **45**, 372 (2012)
- ¹¹⁹ M.E.G. Lyons, and R.L. Doyle, *Int. J. Electrochem. Sci.*, **6**, 5710 (2011)
- ¹²⁰ T. Takashima, K. Ishikawa, and H. Irie, *J. Phys. Chem. C*, **120**, 24827 (2016)
- ¹²¹ G. Zhang, X. Li, Y. Li, and D. Chen, *Mol. Phys.*, **111**, 3276 (2013)
- ¹²² S. Rizzato, J. Bergès, S.A. Mason, A. Albinati, and J. Kozelka, *Angew. Chem. Int. Ed. Engl.*, **49**, 7440 (2010)
- ¹²³ F. Bartha, O. Kapuy, C. Kozmutza, and C. Van Alsenoy, *J. Mol. Struct-Theochem*, **666**, 117 (2003)
- ¹²⁴ A. Grimaud, O. Diaz-Morales, B. Han, W.T. Hong, Y.-L. Lee, L. Giordano, K.A. Stoerzinger, M.T.M. Koper, and Y. Shao-Horn, *Nat. Chem.*, **9**, 457 (2017)
- ¹²⁵ B. Lim, M. Jiang, P.H.C. Camargo, E.C. Cho, J. Tao, X. Lu, Y. Zhu, Y. Xia, *Science*, **324**, 1302 (2009)
- ¹²⁶ V.R. Stamenkovic, B. Fowler, B.S. Mun, G. Wang, P.N. Ross, C.A. Lucas, and N.M. Markovi, *Science*, **315**, 493 (2007)
- ¹²⁷ H. Li, G. Sun, N. Li, S. Sun, D. Su, and Q. Xin, *J. Phys. Chem. C*, **111**, 5605 (2007)
- ¹²⁸ X. Tong, X. Xia, C. Guo, Y. Zhang, J. Tu, H. Jin Fan, and X.-Y. Guo, *J. Mater. Chem. A*, **3**, 18372 (2015)
- ¹²⁹ K. Gong, F. Du, Z. Xia, M. Durstock, L. Dai, *Science*, **323**, 760 (2009)
- ¹³⁰ W. Song, Z. Ren, S.-Y. Chen, Y. Meng, S. Biswas, P. Nandi, H.A. Elsen, P.-X. Gao, and S.L. Suib, *ACS Appl. Mater. Interfaces*, **8**, 20802 (2016)
- ¹³¹ X. Ge, Y. Liu, F.W. Goh, T.S. Hor, Y. Zong, P. Xiao, Z. Zhang, S.H. Lim, B. Li, X. Wang, and Z. Liu, *ACS Appl. Mater. Interfaces*, **6**, 12684 (2014)
- ¹³² A. Serov, N.I. Andersen, A.J. Roy, I. Matanovic, K. Artyushkova, and P. Atanassov, *J. Electrochem. Soc.*, **162**, F449 (2015)
- ¹³³ J. Xu, P. Gao, and T. S. Zhao, *Energy Environ. Sci.*, **5**, 5333 (2012)
- ¹³⁴ J. Xiao, Q. Kuang, S. Yang, F. Xiao, S. Wang, and L. Guo, *Scientific Reports*, **3**, 2300 (2013)
- ¹³⁵ J. Chen, and A. Selloni, *Phys. Rev. B*, **85**, 085306 (2012)
- ¹³⁶ J. Heyd, G. E. Scuseria, and M. Ernzerhof, *J. Chem. Phys.*, **118**, 8207 (2003)
- ¹³⁷ K. Mathew, R. Sundararaman, K. Letchworth-Weaver, T. A. Arias, and R. G. Hennig, *J. Chem. Phys.*, **140**, 084106 (2014)
- ¹³⁸ W.L. Smith, and A.D. Hobson, *Acta Cryst. B*, **29**, 362 (1973)
- ¹³⁹ C.D. Spencer, and D. Schroeer, *Phys. Rev. B*, **9**, 3658 (1974)
- ¹⁴⁰ B. Varghese, B. Mukherjee, K.R.G. Karthik, K.B. Jinesh, S.G. Mhaisalkar, E.S. Tok, and C.H. Sow, *J. Appl. Phys.*, **111**, 104306 (2012)
- ¹⁴¹ D. Barreca, C. Massignan, S. Daolio, M. Fabrizio, C. Piccirillo, L. Armelao, and E. Tondello, *Chem. Mater.*, **13**, 588 (2001)

- ¹⁴² V.R. Shinde, S.B. Mahadik, T.P. Gujar, C.D. Lokhande, *Appl. Surf. Sci.*, **252**, 7487 (2006)
- ¹⁴³ L. Qiao, H.Y. Xiao, H.M. Meyer, J.N. Sun, C.M. Rouleau, A.A. Puretzky, D.B. Geohegan, I.N. Ivanov, M. Yoon, W. J. Weberb, and M.D. Biegalski, *J. Mater. Chem. C*, **1**, 4628 (2013)
- ¹⁴⁴ J.P. Beaufils, and Y. Barbaux, *J. Appl. Cryst.*, **15**, 301 (1982)
- ¹⁴⁵ W. Meyer, K. Biedermann, M. Gubo, L. Hammer, and K. Heinz, *J. Phys. Condens. Matter*, **20**, 265011 (2008)
- ¹⁴⁶ J. Suntivich, H.A. Gasteiger, N. Yabuuchi, H. Nakanishi, J.B. Goodenough, and Y. Shao-Horn, *Nat. Chem.*, **3**, 546 (2011)
- ¹⁴⁷ I.C. Man, H.-Y. Su, F. Calle-Vallejo, H.A. Hansen, J.I Martinez, N.G. Inoglu, J. Kitchin, T.F. Jaramillo, J.K. Nørskov, and J. Rossmeisl, *Chem. Cat. Chem.*, **3**, 1159 (2011)
- ¹⁴⁸ Y. Wang, and H.-P. Cheng, *J. Phys. Chem. C*, **117**, 2106 (2013)
- ¹⁴⁹ S. Liu, L. Li, H.S. Ahn, and A. Manthiram, *J. Mater. Chem. A*, **3**, 11615 (2015)
- ¹⁵⁰ J.K Nørskov, J. Rossmeisl, A. Logadottir, L. Lindqvist, J.R. Kitchin, T. Bligaard, and H. Jónsson, *J. Phys. Chem. B*, **108**, 17886 (2004)
- ¹⁵¹ J.D. Cox, D.D. Wagman, and V.A. Medvedev, CODATA Key Values for Thermodynamics, Hemisphere Publishing Corp., New York, 1984
- ¹⁵² M.W. Chase Jr., NIST-JANAF Thermochemical Tables, Fourth Edition, *J. Phys. Chem. Ref. Data*, Monograph 9, 1998
- ¹⁵³ M. Takahashi, S. Tobishima, K. Takei, and Y. Sakurai, *J. Power. Sources*, **97-98**, 508 (2001)
- ¹⁵⁴ Y. Wang, P. He, and H. Zhou, *Energy Environ. Sci.*, **4**, 805 (2011)
- ¹⁵⁵ L.-X. Yuan, Z.-H. Wang, W.-X. Zhang, X.-L. Hu, J.-T. Chen, Y.-H. Huang, and J. B. Goodenough, *Energy Environ. Sci.*, **4**, 269 (2011)
- ¹⁵⁶ J. Li, W. Yao, S. Martin, and D. Vaknin, *Solid State Ionics*, **179**, 2016 (2008)
- ¹⁵⁷ S. Chung, J. Bloking, and Y. Chiang, *Nat. Mater.*, **1**, 123 (2002)
- ¹⁵⁸ M. Park, X. Zhang, M. Chung, G. B. Less, and A. M. Sastry, *J. Power Sources*, **195**, 7904 (2010)
- ¹⁵⁹ M. S. Islam, D. J. Driscoll, C. A. J. Fisher, and P. R. Slater, *Chem. Mater.*, **17**, 5085 (2005)
- ¹⁶⁰ G. K. P. Dathar, D. Sheppard, K. J. Stevenson, and G. Henkelman, *Chem. Mater.*, **23**, 4032 (2011)
- ¹⁶¹ K. Hoang, and M. Johannes, *Chem. Mater.*, **23**, 3003 (2011)
- ¹⁶² P. E. Blochl, *Phys. Rev. B*, **50**, 17953 (1994)
- ¹⁶³ G. Kresse, and D. Joubert, *Phys. Rev. B*, **59**, 1758 (1999)
- ¹⁶⁴ H. J. Monkhorst, and J. D. Pack, *Phys. Rev. B*, **13**, 5188 (1976)
- ¹⁶⁵ G. Rousse, J. Rodriguez-Carvajal, S. Patoux, and C. Masquelier, *Chem. Mater.*, **15**, 4082 (2003)
- ¹⁶⁶ J. Gou, *Proc SPIE*, **6650**, 66500F (2007)
- ¹⁶⁷ I.P. Shapiro, *Optika i Spektroskopiya*, **4**, 256 (1958)

- ¹⁶⁸ K. Zaghib, A. Mauger, J. B. Goodenough, F. Gendron, and C. M. Julien, *Chem. Mater.*, **19**, 3740 (2007)
- ¹⁶⁹ G. Makov, and M. C. Payne, *Phys. Rev. B*, **51**, 4014 (1995)
- ¹⁷⁰ C. Kuss, G. Liang, and S. B. Schougaard, *J. Mater. Chem.*, **22**, 24889 (2012)
- ¹⁷¹ Y.-H. Tsai, C.-Y. Chou, K. E. Kweon, S.-U. Park, K.-H. Song, C.-K. Back, and G. S. Hwang, *Electrochem. Lett.* **2**, A111-A113 (2013)
- ¹⁷² F. D. Murbaghan, *Proc. Natl. Acad. Sci.* **30**, 244 (1994)
- ¹⁷³ T. Maxish; G. Ceder; *Phys. Rev. B*, **73**, 174112 (2006)